Site U1562[1]

A. Briais, R.E. Parnell-Turner, L.J. LeVay, Y. Cui, A. Di Chiara, J.P. Dodd, T. Dunkley Jones, D. Dwyer, D.E. Eason, S.A. Friedman, S.R. Hemming, K. Hochmuth, H. Ibrahim, C. Jasper, B.T. Karatsolis, S. Lee, D.E. LeBlanc, M.R. Lindsay, D.D. McNamara, S.E. Modestou, B. Murton, S. OConnell, G.T. Pasquet, P.N. Pearson, S.P. Qian, Y. Rosenthal, S. Satolli, M. Sinnesael, T. Suzuki, T. Thulasi Doss, N.J. White, T. Wu, A. Yang Yang, V. dos Santos Rocha, C. Pearman, and C.Y. Tian[2]

Contents

Keywords

Core descriptions

Supplementary material

References (RIS)

1. Background and objectives

Site U1562 is located on Björn drift, on the eastern flank of the Reykjanes Ridge in the North Atlantic Ocean. It is located ~12 km east of Site U1554 (Figures **F1**, **F2**) on a basement high at the eastern edge of the main drift deposit. Site U1562 is located on crustal V-shaped ridge (VSR) 3, which is associated with a high in the free-air gravity anomaly, whereas Site U1554 is located on V-shaped trough (VST) 2b. Site U1562 sits on ocean crust with an age of 13.86 Ma estimated from magnetic anomalies.

Site U1562 is located on Seismic Line JC50-1 (Common Midpoint [CMP] 39920) near the intersection with Seismic Line JC50-C2 (CMP 685) (Figures **F2**, **F3**); both lines were obtained in 2010 during RRS *James Cook* Cruise JC50 (Parnell-Turner et al., 2017). Sediment thickness at Site U1562 was expected to be ~465 m (3.237 s two-way traveltime [TWT]) based on seismic imagery. The sediment section at the site is marked by the pinching out of the Björn drift sedimentary deposit, a thicker section of which was cored at Site U1554. Several disruptions in the sediment succession on the seismic profile suggest the presence of unconformities and possible changes in
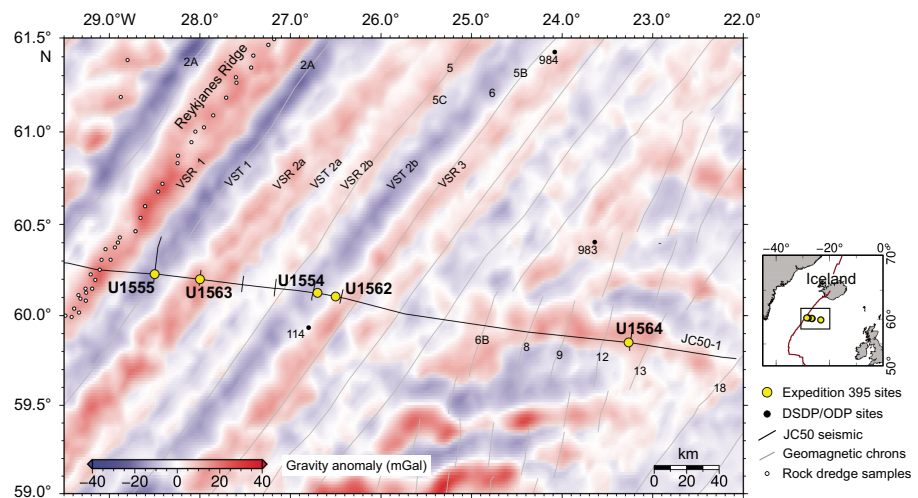
Figure F1. Satellite free-air gravity anomaly map, Expedition 395. Inset: North Atlantic region. Solid line = mid-Atlantic ridge, box = location of main panel.

the conditions of sediment deposition and evolution. One target for Site U1562 was to obtain a continuous sedimentary record of Björn drift, which will offer millennial-scale climate records. Another target was to core the basaltic crust at a VSR to provide constraints on mantle melting conditions and hydrothermal alteration of the crust, especially in comparison with basalt from Site U1554 located on a VST. Cores and data from this site will address all three of the primary science objectives: (1) crustal accretion and mantle behavior; (2) ocean circulation, gateways, and sedimentation; and (3) time-dependent hydrothermal alteration of oceanic crust.

The operational objectives for this site were to core the sedimentary section using the advanced piston corer (APC)/extended core barrel (XCB) system to the sediment/basement interface, use the rotary core barrel (RCB) system to core ~130 m into the basement, and use downhole wireline tools to log the borehole.

Figure F2. Seismic Profile JC50-1 near Sites U1554 and U1562. Modified from Parnell-Turner et al. (2017).

Figure F3. Bathymetric map, Site U1562. Data from the 2010 JC50 site survey cruise. Numbered dots = CMPs.

2. Operations

Site U1562 (60°06.3006′N, 26°30.1044′W) consists of three holes, 395C-U1562A, 395C-U1562B, and 395-U1562C, that extend to 300.4–561.5 m drilling depth below seafloor (DSF) (Table T1).
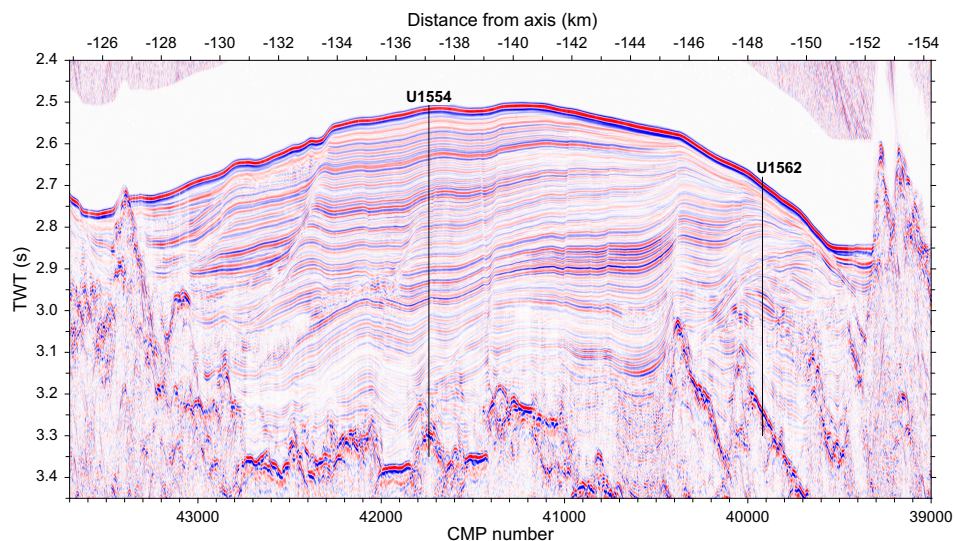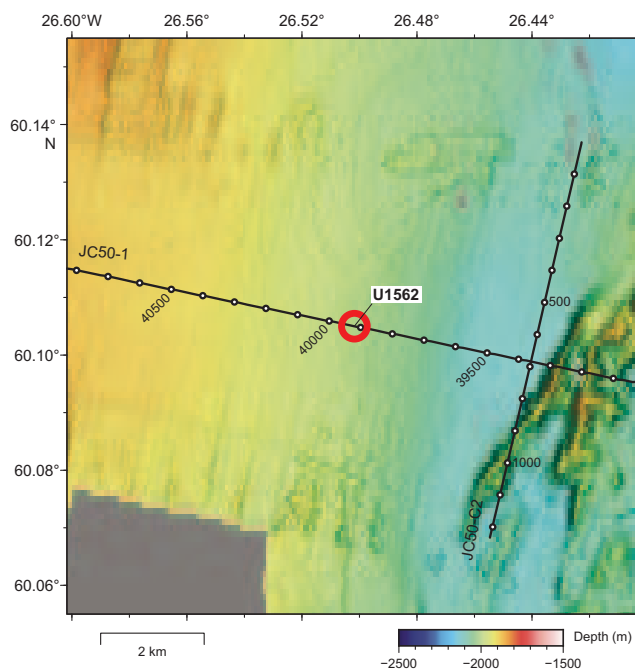
A total of 144 cores were recovered at Site U1562. These cores collected 792.57 m of sediment and basalt over a cored interval of 876.6 m (90% recovery). The APC system was used to collect 36 cores over a 330.0 m interval with 343.87 m of core recovered (104% recovery). The half-length APC (HLAPC) was deployed for 69 cores and recovered 337.83 m of sediment from a 324.3 m interval (104% recovery). The XCB system was deployed over a 68.6 m interval. The eight XCB cores recovered 37.79 m of sediment and basalt (55% recovery). The RCB system was deployed over a 153.4 m interval with 73.08 m of core recovered (48% recovery). A total of 31 cores were collected with the RCB system. Downhole wireline logging operations using four logging tools took place in Hole U1562B.

The total time spent at Site U1562 was 12.3 days.

Table T1. Core summary, Site U1562. H = APC, F = HLAPC, X = XCB, R = RCB. DSF = drilling depth below seafloor, CSF = core depth below seafloor. (Continued on next two pages.) **Download table in CSV format.**

Hole U1562A
Expedition 395C
Latitude: 60°6.3030′N
Longitude: 26°30.1245′W
Water depth (mbsl): 2003.4
Time on hole (days): 3.27
Seafloor depth DRF (m): 2014.5
Rig floor to sea level (m): 11.1
Penetration DSF (m): 429.8
Cored interval (m): 429.8
Recovered length (m): 411.04
Recovery (%): 96
Total cores (*N*): 65

Hole U1562B
Expedition 395C
Latitude: 60°6.2993′N
Longitude: 26°30.1026′W
Water depth (mbsl): 2003.4
Time on hole (days): 7.18
Seafloor depth DRF (m): 2014.5
Rig floor to sea level (m): 11.1
Penetration DSF (m): 561.5
Cored interval (m): 153.4
Recovered length (m): 73.08
Recovery (%): 48
Total cores (*N*): 31

Hole U1562C
Expedition 395
Latitude: 60°6.3015′N
Longitude: 26°30.0754′W
Water depth (mbsl): 2002.7
Time on hole (days): 1.86
Seafloor depth DRF (m): 2014.2
Rig floor to sea level (m): 11.5
Penetration DSF (m): 300.4
Cored interval (m): 293.4
Recovered length (m): 308.45
Recovery (%): 105
Total cores (*N*): 48

Core	Date	Core on deck time UTC (h)	Top of cored interval depth DSF (m)	Bottom of cored interval depth DSF (m)	Interval advanced (m)	Top of cored interval depth CSF (m)	Bottom of cored interval depth CSF (m)	Length of core recovered (m)	Recovery (%)	Sections (N)	Temperature measurement	Oriented	Lithology
395C-U1562A-													
1H	10 Jul 2021	2135	0.0	2.0	2.0	0.0	2.04	2.08	104	3		Y	Sediment
2H	10 Jul 2021	2305	2.0	11.5	9.5	2.0	11.09	9.09	96	7		Y	Sediment
3H	11 Jul 2021	0055	11.5	21.0	9.5	11.5	21.37	9.87	104	8		Y	Sediment
4H	11 Jul 2021	0155	21.0	30.5	9.5	21.0	31.11	10.11	106	8	APCT-3	Y	Sediment
5H	11 Jul 2021	0235	30.5	40.0	9.5	30.5	40.46	9.96	105	8		Y	Sediment
6H	11 Jul 2021	0320	40.0	49.5	9.5	40.0	49.76	9.76	103	8		Y	Sediment
7H	11 Jul 2021	0415	49.5	59.0	9.5	49.5	59.52	10.02	105	8	APCT-3	Y	Sediment
8H	11 Jul 2021	0500	59.0	68.5	9.5	59.0	68.91	9.91	104	8		Y	Sediment
9H	11 Jul 2021	0545	68.5	78.0	9.5	68.5	78.49	9.99	105	8		Y	Sediment
10H	11 Jul 2021	0650	78.0	87.5	9.5	78.0	88.10	10.1	106	8	APCT-3	Y	Sediment
11H	11 Jul 2021	0735	87.5	97.0	9.5	87.5	97.38	9.88	104	8		Y	Sediment
12H	11 Jul 2021	0820	97.0	106.5	9.5	97.0	106.86	9.86	104	8		Y	Sediment
13H	11 Jul 2021	0925	106.5	116.0	9.5	106.5	116.59	10.09	106	8	APCT-3	Y	Sediment
14H	11 Jul 2021	1010	116.0	125.5	9.5	116.0	125.63	9.63	101	8		Y	Sediment
15H	11 Jul 2021	1120	125.5	135.0	9.5	125.5	135.47	9.97	105	8		Y	Sediment
16H	11 Jul 2021	1215	135.0	144.5	9.5	135.0	144.63	9.63	101	8		Y	Sediment
17H	11 Jul 2021	1300	144.5	154.0	9.5	144.5	154.51	10.01	105	8		Y	Sediment
18H	11 Jul 2021	1400	154.0	163.5	9.5	154.0	163.46	9.46	100	8		Y	Sediment
19H	11 Jul 2021	1445	163.5	173.0	9.5	163.5	173.52	10.02	105	8		Y	Sediment
20H	11 Jul 2021	1530	173.0	182.5	9.5	173.0	183.02	10.02	105	8		Y	Sediment
21H	11 Jul 2021	1655	182.5	192.0	9.5	182.5	192.49	9.99	105	8		Y	Sediment
22F	11 Jul 2021	2010	192.0	196.7	4.7	192.0	196.92	4.92	105	5			Sediment
23F	11 Jul 2021	2045	196.7	201.4	4.7	196.7	201.56	4.86	103	5			Sediment
24F	11 Jul 2021	2125	201.4	206.1	4.7	201.4	206.26	4.86	103	5			Sediment
25F	11 Jul 2021	2155	206.1	210.8	4.7	206.1	211.03	4.93	105	5			Sediment
26F	11 Jul 2021	2240	210.8	215.5	4.7	210.8	215.73	4.93	105	5			Sediment
27F	11 Jul 2021	2320	215.5	220.2	4.7	215.5	220.40	4.90	104	5			Sediment
28F	11 Jul 2021	2350	220.2	224.9	4.7	220.2	224.93	4.73	101	5			Sediment
29F	12 Jul 2021	0030	224.9	229.6	4.7	224.9	229.86	4.96	106	5			Sediment

Table T1 (continued). (Continued on next page.)

Core	Date	Core on deck time UTC (h)	Top of cored interval depth DSF (m)	Bottom of cored interval depth DSF (m)	Interval advanced (m)	Top of cored interval depth CSF (m)	Bottom of cored interval depth CSF (m)	Length of core recovered (m)	Recovery (%)	Sections (N)	Temperature measurement	Oriented	Lithology
30F	12 Jul 2021	0110	229.6	234.3	4.7	229.6	234.51	4.91	104	5			Sediment
31F	12 Jul 2021	0200	234.3	239.0	4.7	234.3	238.21	3.91	83	4			Sediment
32F	12 Jul 2021	0240	239.0	243.7	4.7	239.0	243.89	4.89	104	5			Sediment
33F	12 Jul 2021	0320	243.7	248.4	4.7	243.7	248.55	4.85	103	5			Sediment
34F	12 Jul 2021	0400	248.4	253.1	4.7	248.4	253.31	4.91	104	5			Sediment
35F	12 Jul 2021	0435	253.1	257.8	4.7	253.1	257.92	4.82	103	5			Sediment
36F	12 Jul 2021	0515	257.8	262.5	4.7	257.8	262.75	4.95	105	5			Sediment
37F	12 Jul 2021	0555	262.5	267.2	4.7	262.5	266.98	4.48	95	4			Sediment
38F	12 Jul 2021	0640	267.2	271.9	4.7	267.2	271.74	4.54	97	4			Sediment
39F	12 Jul 2021	0720	271.9	276.6	4.7	271.9	276.36	4.46	95	4			Sediment
40F	12 Jul 2021	0755	276.6	281.3	4.7	276.6	281.20	4.60	98	4			Sediment
41F	12 Jul 2021	0835	281.3	286.0	4.7	281.3	286.31	5.01	107	5			Sediment
42F	12 Jul 2021	0910	286.0	290.7	4.7	286.0	290.97	4.97	106	5			Sediment
43F	12 Jul 2021	0945	290.7	295.4	4.7	290.7	295.61	4.91	104	5			Sediment
44F	12 Jul 2021	1030	295.4	300.1	4.7	295.4	300.28	4.88	104	5			Sediment
45F	12 Jul 2021	1110	300.1	304.8	4.7	300.1	304.81	4.71	100	4			Sediment
46F	12 Jul 2021	1200	304.8	309.5	4.7	304.8	309.77	4.97	106	5			Sediment
47F	12 Jul 2021	1235	309.5	314.2	4.7	309.5	314.43	4.93	105	5			Sediment
48F	12 Jul 2021	1315	314.2	318.9	4.7	314.2	318.96	4.76	101	4			Sediment
49F	12 Jul 2021	1355	318.9	323.6	4.7	318.9	323.90	5.00	106	5			Sediment
50F	12 Jul 2021	1430	323.6	328.3	4.7	323.6	328.54	4.94	105	5			Sediment
51F	12 Jul 2021	1500	328.3	333.0	4.7	328.3	332.89	4.59	98	4			Sediment
52F	12 Jul 2021	1545	333.0	337.7	4.7	333.0	337.89	4.89	104	5			Sediment
53F	12 Jul 2021	1620	337.7	342.4	4.7	337.7	342.64	4.94	105	5			Sediment
54F	12 Jul 2021	1655	342.4	347.1	4.7	342.4	347.42	5.02	107	5			Sediment
55F	12 Jul 2021	1735	347.1	351.8	4.7	347.1	352.06	4.96	106	5			Sediment
56F	12 Jul 2021	1815	351.8	356.5	4.7	351.8	356.75	4.95	105	5			Sediment
57F	12 Jul 2021	2040	356.5	361.2	4.7	356.5	361.46	4.96	106	5			Sediment
58X	12 Jul 2021	2220	361.2	370.9	9.7	361.2	366.27	5.07	52	5			Sediment
59X	12 Jul 2021	2330	370.9	380.6	9.7	370.9	378.98	8.08	83	7			Sediment
60X	13 Jul 2021	0155	380.6	390.3	9.7	380.6	383.11	2.51	26	3			Sediment
61X	13 Jul 2021	0405	390.3	400.0	9.7	390.3	395.09	4.79	49	4			Sediment
62X	13 Jul 2021	0555	400.0	409.7	9.7	400.0	404.52	4.52	47	4			Sediment
63X	13 Jul 2021	0805	409.7	419.4	9.7	409.7	413.32	3.62	37	4			Sediment
64X	13 Jul 2021	1025	419.4	429.1	9.7	419.4	427.82	8.52	88	7			Sediment
65X	13 Jul 2021	1250	429.1	429.8	0.7	429.1	429.81	0.68	97	1			Basalt
395C-U1562B-													
11						***** Drilled from 0 to 408.1 DSF (m)*****							
2R	14 Jul 2021	1510	408.1	417.6	9.5	408.1	412.23	4.13	43	4			Sediment
3R	14 Jul 2021	1603	417.6	427.1	9.5	417.6	422.25	4.65	49	4			Sediment
4R	14 Jul 2021	1805	427.1	432.1	5.0	427.1	431.52	4.38	88	4			Sediment/basalt interface
5R	14 Jul 2021	2150	432.1	436.8	4.7	432.1	435.70	3.44	73	3			Basalt
6R	15 Jul 2021	0115	436.8	441.8	5.0	436.8	441.67	3.93	79	4			Basalt
7R	15 Jul 2021	0450	441.8	446.5	4.7	441.8	443.35	1.37	29	2			Basalt
8R	15 Jul 2021	0815	446.5	451.5	5.0	446.5	449.63	2.74	55	3			Basalt
9R	15 Jul 2021	1215	451.5	455.5	4.0	451.5	454.66	2.55	64	3			Basalt
10R	15 Jul 2021	1725	455.5	460.5	5.0	455.5	458.58	2.71	54	3			Basalt
11R	15 Jul 2021	2125	460.5	465.2	4.7	460.5	463.09	2.21	47	2			Basalt
12R	15 Jul 2021	2355	465.2	470.2	5.0	465.2	467.31	1.66	33	2			Basalt
13R	16 Jul 2021	0335	470.2	474.2	4.0	470.2	473.46	2.46	62	3			Basalt
14R	16 Jul 2021	0535	474.2	479.2	5.0	474.2	476.39	1.96	39	3			Basalt and sediment
15R	16 Jul 2021	0850	479.2	483.9	4.7	479.2	482.65	2.80	60	3			Basalt
16R	16 Jul 2021	1220	483.9	488.9	5.0	483.9	485.68	1.31	26	2			Basalt
17R	16 Jul 2021	1620	488.9	493.6	4.7	488.9	493.89	3.72	79	4			Basalt
18R	16 Jul 2021	1955	493.6	498.6	5.0	493.6	495.90	1.68	34	2			Basalt
19R	16 Jul 2021	2250	498.6	500.7	2.1	498.6	499.82	0.95	45	1			Basalt
20R	17 Jul 2021	2145	500.7	503.3	2.6	500.7	503.15	1.96	75	2			Basalt
21R	18 Jul 2021	0100	503.3	508.3	5.0	503.3	506.45	2.12	42	3			Basalt
22R	18 Jul 2021	0530	508.3	513.0	4.7	508.3	509.51	0.82	17	1			Basalt
23R	18 Jul 2021	0850	513.0	518.0	5.0	513.0	516.66	2.71	54	3			Basalt
24R	18 Jul 2021	1210	518.0	522.7	4.7	518.0	519.95	1.71	36	2			Basalt
25R	18 Jul 2021	1710	522.7	527.7	5.0	522.7	526.76	3.50	70	3			Basalt
26R	18 Jul 2021	1910	527.7	532.4	4.7	527.7	528.84	0.87	19	1			Basalt
27R	18 Jul 2021	2110	532.4	537.4	5.0	532.4	535.07	2.17	43	2			Basalt
28R	18 Jul 2021	2325	537.4	542.1	4.7	537.4	539.54	1.63	35	2			Basalt
29R	19 Jul 2021	0210	542.1	547.1	5.0	542.1	543.60	1.31	26	1			Basalt

Table T1 (continued).

Core	Date	Core on deck time UTC (h)	Top of cored interval depth DSF (m)	Bottom of cored interval depth DSF (m)	Interval advanced (m)	Top of cored interval depth CSF (m)	Bottom of cored interval depth CSF (m)	Length of core recovered (m)	Recovery (%)	Sections (N)	Temperature measurement	Oriented	Lithology
30R	19 Jul 2021	0515	547.1	551.8	4.7	547.1	548.90	1.37	29	2			Basalt
31R	19 Jul 2021	0805	551.8	556.8	5.0	551.8	554.06	1.91	38	2			Basalt
32R	19 Jul 2021	1105	556.8	561.5	4.7	556.8	559.60	2.35	50	2			Basalt
395-U1562C-													
1H	1 Jul 2023	1515	0.0	5.3	5.3	0.0	5.370	5.37	101	5		Y	Sediment
2H	1 Jul 2023	1605	5.3	14.8	9.5	5.3	15.08	9.78	103	8		Y	Sediment
3H	1 Jul 2023	1650	14.8	24.3	9.5	14.8	24.67	9.87	104	8		Y	Sediment
4H	1 Jul 2023	1730	24.3	33.8	9.5	24.3	34.37	10.07	106	8		Y	Sediment
51					*****Drilled from 33.8 to 34.8 DSF (m)*****								
6H	1 Jul 2023	1900	34.8	44.3	9.5	34.8	44.86	10.06	106	8		Y	Sediment
7H	1 Jul 2023	1945	44.3	53.8	9.5	44.3	54.25	9.95	105	8		Y	Sediment
8H	1 Jul 2023	2030	53.8	63.3	9.5	53.8	63.83	10.03	106	8		Y	Sediment
9H	1 Jul 2023	2110	63.3	72.8	9.5	63.3	73.18	9.88	104	8		Y	Sediment
10H	1 Jul 2023	2150	72.8	82.3	9.5	72.8	82.70	9.90	104	8		Y	Sediment
11H	1 Jul 2023	2235	82.3	91.8	9.5	82.3	92.40	10.10	106	8		Y	Sediment
12H	1 Jul 2023	2320	91.8	101.3	9.5	91.8	101.80	10.00	105	8		Y	Sediment
13H	2 Jul 2023	0010	101.3	110.8	9.5	101.3	111.28	9.98	105	8		Y	Sediment
14H	2 Jul 2023	0100	110.8	120.3	9.5	110.8	120.76	9.96	105	8		Y	Sediment
15H	2 Jul 2023	0145	120.3	129.8	9.5	120.3	129.84	9.54	100	8		Y	Sediment
16H	2 Jul 2023	0320	129.8	139.3	9.5	129.8	139.73	9.93	105	8		Y	Sediment
17F	2 Jul 2023	0420	139.3	144.0	4.7	139.3	144.22	4.92	105	5			Sediment
18F	2 Jul 2023	0500	144.0	148.7	4.7	144.0	148.50	4.50	96	4			Sediment
191					*****Drilled from 148.7 to 150.2 DSF (m)*****								
20F	2 Jul 2023	0530	150.2	154.9	4.7	150.2	155.20	5.00	106	5			Sediment
21F	2 Jul 2023	0615	154.9	159.6	4.7	154.9	159.93	5.03	107	5			Sediment
22F	2 Jul 2023	0700	159.6	164.3	4.7	159.6	164.56	4.96	106	5			Sediment
23F	2 Jul 2023	0735	164.3	169.0	4.7	164.3	169.19	4.89	104	5			Sediment
241					*****Drilled from 169.0 to 170.5 DSF (m)*****								
25F	2 Jul 2023	0820	170.5	175.2	4.7	170.5	175.46	4.96	106	5			Sediment
26F	2 Jul 2023	0905	175.2	179.9	4.7	175.2	180.13	4.93	105	5			Sediment
27F	2 Jul 2023	0945	179.9	184.6	4.7	179.9	184.93	5.03	107	5			Sediment
28F	2 Jul 2023	1025	184.6	189.3	4.7	184.6	189.62	5.02	107	5			Sediment
29F	2 Jul 2023	1100	189.3	194.0	4.7	189.3	194.18	4.88	104	5			Sediment
30F	2 Jul 2023	1140	194.0	198.7	4.7	194.0	198.98	4.98	106	5			Sediment
31F	2 Jul 2023	1215	198.7	203.4	4.7	198.7	203.75	5.05	107	5			Sediment
32F	2 Jul 2023	1250	203.4	208.1	4.7	203.4	208.28	4.88	104	5			Sediment
33F	2 Jul 2023	1330	208.1	212.8	4.7	208.1	213.14	5.03	107	5			Sediment
34F	2 Jul 2023	1405	212.8	217.5	4.7	212.8	217.81	5.01	107	5			Sediment
35F	2 Jul 2023	1440	217.5	222.2	4.7	217.5	222.26	4.76	101	5			Sediment
36F	2 Jul 2023	1540	222.2	226.9	4.7	222.2	227.09	4.89	104	5			Sediment
37F	2 Jul 2023	1615	226.9	231.6	4.7	226.9	231.91	5.01	107	5			Sediment
381					*****Drilled from 231.6 to 232.6 DSF (m)*****								
39F	2 Jul 2023	1655	232.6	237.3	4.7	232.6	237.57	4.97	106	5			Sediment
40F	2 Jul 2023	1725	237.3	242.0	4.7	237.3	242.27	4.97	106	5			Sediment
41F	2 Jul 2023	1800	242.0	246.7	4.7	242.0	247.03	5.03	107	5			Sediment
42F	2 Jul 2023	1840	246.7	251.4	4.7	246.7	251.76	5.06	108	5			Sediment
431					*****Drilled from 251.4 to 253.4 DSF (m)*****								
44F	2 Jul 2023	1915	253.4	258.1	4.7	253.4	258.46	5.06	108	5			Sediment
45F	2 Jul 2023	1955	258.1	262.8	4.7	258.1	263.13	5.03	107	5			Sediment
46F	2 Jul 2023	2055	262.8	267.5	4.7	262.8	267.90	5.10	109	5			Sediment
47F	2 Jul 2023	2135	267.5	272.2	4.7	267.5	272.53	5.03	107	5			Sediment
48F	2 Jul 2023	2210	272.2	276.9	4.7	272.2	277.16	4.96	106	5			Sediment
49F	2 Jul 2023	2245	276.9	281.6	4.7	276.9	281.94	5.04	107	5			Sediment
50F	2 Jul 2023	2325	281.6	286.3	4.7	281.6	286.56	4.96	106	5			Sediment
51F	3 Jul 2023	0010	286.3	291.0	4.7	286.3	291.36	5.06	108	5			Sediment
52F	3 Jul 2023	0055	291.0	295.7	4.7	291.0	295.99	4.99	106	5			Sediment
53F	3 Jul 2023	0150	295.7	300.4	4.7	295.7	300.73	5.03	107	5			Sediment
		Site U1562 totals:		876.5				792.57	90	825			

2.1. Expedition 395C

2.1.1. Hole U1562A

The vessel began the 6.1 nmi transit from Hole U1554F to Site U1562 in dynamic positioning (DP) mode on 10 July 2021. The crew continued to pull up the drill pipe following the completion of operations in Hole U1554F during the transit. The end of the pipe cleared the rotary table at 1130 h UTC. At 1306 h on 10 July, the vessel arrived at Site U1562, and the APC/XCB bottom-hole assembly (BHA) was made up. The drill pipe was run to 1996 meters below sea level (mbsl) to take the first APC core.

Hole U1562A (60°06.3030′N, 26°30.1245′W), located 21 m west of the site coordinates, was spudded at 2115 h, and Core 1H recovered the mudline and 2.08 m of core, establishing a seafloor depth of 2003.4 mbsl. Cores 2H–21H were advanced from 2.0 to 192.0 m DSF using the APC system. Core 21H experienced significant overpull and was drilled over with the drill string to release the core barrel. HLAPC core barrels were made up, and coring continued with Cores 22F–57F (192.0–361.2 m DSF) with 4.7 m advances. HLAPC refusal was met with Core 57F, which also required the drill string to drill over the core barrel to release it from the sediment. The XCB core barrels were made up, and coring continued with Cores 58X–64X (361.2–429.1 m DSF). After coring Core 64X, the XCB cutting shoe was severely damaged and slightly melted and the base of the core catcher contained basalt. Another core barrel was deployed, and Core 65X was advanced to ensure that the bit had reached basement. The bit advanced 0.7 m over 1 h, and Core 65X recovered 0.68 m of basalt, confirming a basement depth of 429.1 m DSF. The final depth of Hole U1562A was 429.8 m DSF. The drill string was pulled from the hole, with the bit reaching the seafloor at 1535 h on 13 July. Hole U1562A ended when the bit reached the rotary table at 1935 h.

All APC cores were oriented, and formation temperature measurements using the advanced piston corer temperature (APCT-3) tool were collected for Cores 395C-U1562A-4H, 7H, 10H, and 13H. Samples for interstitial water (IW), microbiology, micropaleontology, and gas analyses were routinely collected on the catwalk.

A total of 411.04 m of core was recovered over a 429.8 m interval (96% recovery). The average recovery for piston cores was 104% with the APC system and 103% with the HLAPC system. The XCB system had an average recovery of 55%.

2.1.2. Hole U1562B

Following the end of Hole U1562A, an RCB BHA with a C-4 RCB bit was made up and the drill string was lowered to the seafloor. The ship was offset 21 m east-southeast of Hole U1562A, near the site coordinates, and Hole U1562B (60°6.2993′N, 26°30.1026′W; 2003.4 mbsl) was spudded at 0320 h on 14 July 2021 and advanced without coring to 408.1 m DSF. The center bit was recovered, and an RCB core barrel was deployed. Cores 2R–13R were advanced from 408.1 to 474.2 m DSF, recovering 48.65 m of sediment and basalt (55% recovery). The sediment/basement interface was recovered in Core 4R at 429.0 m DSF. Coring rates drastically sped up from ~2 to over 7 m/h while drilling Core 14R. The driller noted that there was a ~3 m interval that drilled extremely quickly. It was soon revealed that Core 14R recovered 0.6 m of carbonate ooze bracketed by basalt. Coring continued with Cores 15R–19R advancing from 479.2 to 500.7 m DSF (47% recovery). While coring Core 19R, the penetration rate dropped to 1 m/h and there was erratic torque on the bit. It was suspected that the drill bit was damaged, and the rig floor crew began pulling the pipe out of the hole. A free-fall funnel was deployed at 0220 h on 17 July to allow for the reentry of Hole U1562B. The bit cleared the seafloor at 0312 h and the rotary table at 0708 h. The bit was indeed damaged; a new C-7 RCB coring bit was made up to the BHA, and the crew assembled the drill string. The subsea camera was deployed at 1130 h to observe the reentry of Hole U1562B, which occurred at 1450 h. The subsea camera was retrieved, and the drill string advanced to 500.7 m DSF. After cleaning the hole with a high-viscosity mud sweep, Cores 20R–28R advanced from 500.7 to 561.5 m DSF. Coring operations concluded in Hole U1562B after coring 132.5 m into the basement section. The final depth of Hole U1562B was 561.5 m DSF.

A total of 73.08 m of core was recovered over a 153.4 m cored interval in Hole U1562B (48% recovery). In all, 31 RCB cores were collected from this hole. The average rate of penetration while coring the basalt was 2.1 m/h.

Following coring, the rotary shifting tool (RST) was run to release the bit into the bottom of the hole. The drill string was pulled up, and the end of the pipe was set at 89 m DSF. The triple combination (triple combo) tool string was made up and deployed at 1755 h on 19 July. After completing two successful passes of the entire hole, the tools were retrieved and reached the rig floor at 2310 h. After the triple combo tool string was laid out, the Formation MicroScanner (FMS)-sonic tool string was made up and deployed at 0100 h on 20 July. Following two passes that extended to the base of the hole, the FMS-sonic tool string was pulled from the hole and reached the rig floor at 0645 h. The next logging run used the Versatile Seismic Imager (VSI). The protected species observation protocols began at 0730 h, and the International Ocean Discovery Program (IODP) technical staff ramped up the air guns starting at 0834 h. The VSI was lowered to the base of the hole, and a total of four depth stations (420.5, 426, 459.9, and 556.6 m wireline log depth below seafloor [WSF]) were completed, two in the basement section, one at the sediment/basement interface, and one in the lowermost sediment. The VSI could not be successfully run throughout the sedimentary section because of the wide diameter (>16 inches) of the borehole. Following the VSI run, the air guns were put away, and the tool reached the rig floor at 1320 h. The final logging run, using the Ultrasonic Borehole Imager (UBI), began at 1445 h. The UBI made two passes of the basement section, acquiring 360° borehole images. The UBI was recovered at the rig floor at 2130 h. The drill string was pulled out of the hole to ~1489 mbsl, and the ship began the transit in DP mode to Hole U1554F at 2355 h on 20 July, ending operations at Site U1562.

2.2. Expedition 395

2.2.1. Hole U1562C

The vessel returned to Site U1562 on 1 July 2023. With the drill bit ~54 m above the seafloor, the vessel transited in DP mode from Site U1554 to Site U1562. Following a 6.1 nmi transit, the vessel was over the site coordinates at 1210 h, marking the start of Hole U1562C (60°06.3015′N, 26°30.0754′W), which was spudded at 1500 h. The mudline Core 1H recovered 5.37 m, establishing a seafloor depth of 2002.7 mbsl. Cores 1H–16H advanced the hole to 139.3 m DSF, and all APC cores were oriented using the Icefield MI-5 core orientation tool. One drilled interval of 1 m (395-U1562C-51) was used to offset coring gaps observed by the stratigraphic correlators.

Core 395-U1562C-16H had 100,000 lb of overpull and required a drill-over to free the core barrel. Refusal of the APC system was reached, and the HLAPC system was deployed for the remainder of the hole. Cores 17F–53F advanced the hole to 300.4 m DSF. Four short drilled intervals (1.5–2 m in length) were used to offset coring gaps between Holes U1562A and U1562C for stratigraphic correlation. After reaching the target depth of 300 m DSF, the drill pipe was pulled from the hole with the bit clearing the seafloor at 0405 h on 3 July. A total of 48 cores were collected in Hole U1562C, recovering 308.45 m of sediment over a 293.4 m cored interval (105% recovery). The BHA was broken down, and the rig was secured for transit. At 0900 h, the ship was switched from DP to cruise mode, ending operations at Site U1562.

3. Lithostratigraphy

The sediments at Site U1562 are primarily composed of silty clay with variable amounts of carbonate (Lithostratigraphic Units I–III), underlain by nannofossil ooze transitioning to chalk near the sediment/basement interface (Unit IV). Unit divisions were made based on (1) visual core description, (2) natural gamma radiation (NGR) measurements, (3) smear slide examination, (4) bulk calcium carbonate ($CaCO_3$) measurements, and (5) L* reflectance (Figures **F4**, **F5**; Table **T2**). To assist understanding the sedimentologic patterns at this site, NGR and reflectance data were smoothed using an eighth-order lowpass Butterworth filter with a cutoff of 0.125 times the Nyquist frequency (Figure **F5**; this was applied to data that had undergone cleaning; see **Physical properties** in the Expedition 395 methods chapter [Parnell-Turner et al., 2025a]). This bidirectional linear digital filter avoids phase shift, maintaining correct peak positions (Butterworth,
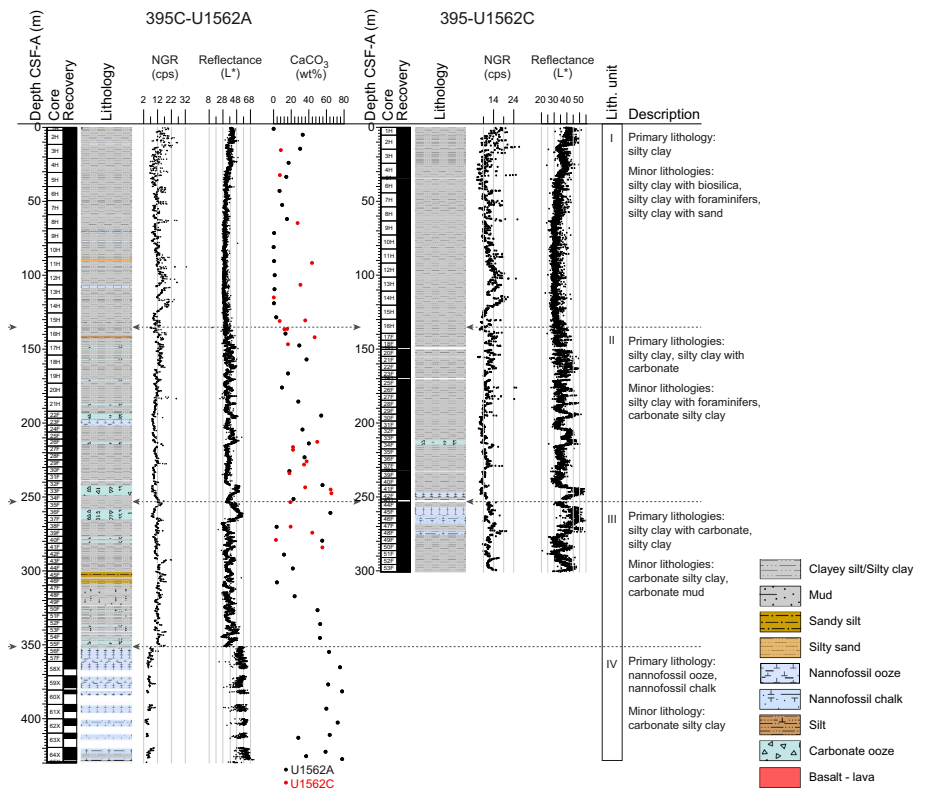
Figure F4. Lithostratigraphic summary, Site U1562. cps = counts per second. For lithology legend, see Figure F9 in the Expedition 395 methods chapter (Parnell-Turner et al., 2025a).
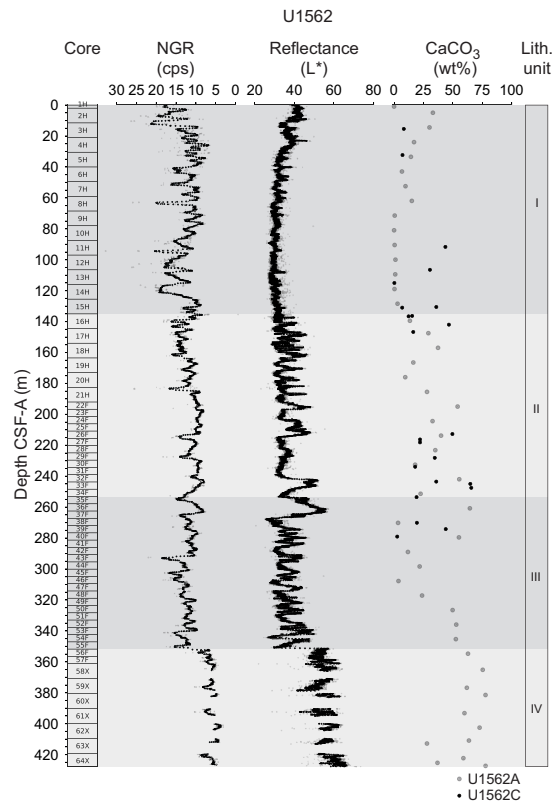

Figure F5. Parameters used for lithologic unit definitions, Site U1562. NGR and reflectance (L*): data from Hole U1562A are shown. cps = counts per second, black/gray dots = data with/without Butterworth filter applied.

1930; Lyons, 2011). Immediately below the transition between Units I and II, there are several sharp boundaries noted in the core sections. Unit III is defined by extensive evidence for soft-sediment deformation, possibly due to a series of slumps. There is a sharp contact between Units III and IV. Weight percent $CaCO_3$ is highly variable, but average values increase downhole (note that $CaCO_3$ measurements were spaced approximately one to three per 10 m and thus may not fully represent $CaCO_3$ variability with depth). Small clasts of volcaniclastic material (pumice and scoria) are found throughout the sequence at Site U1562. All clasts larger than 2 cm are listed in Table **T3**.

3.1. Lithostratigraphic Unit I

Intervals: 395C-U1562A-1H, 0 cm, to 16H-1, 0 cm; 395-U1562C-1H-1, 0 cm, to 16H-4, 0 cm
Depths: Hole U1562A = 0–135.0 m core depth below seafloor, Method A (CSF-A); Hole
     U1562C = 0–135.23 m CSF-A
Thickness: Hole U1562A = 135.0 m; Hole U1562C = 135.23 m
Age: Holocene to early Pliocene
Lithology: silty clay

Unit I is primarily silty clay, most commonly grayish brown, gray, and light brownish gray in Hole U1562A (Figure **F6**). During Expedition 395, when cores were described soon after recovery, col-

Table T2. Lithostratigraphic summary, Site U1562. EOH = end of hole. **Download table in CSV format.**

Lith. unit	Interval	Depth CSF-A (m)	Age	Main lithologies	Minor lithologies
I	395C-U1562A-1H, 0 cm, to 16H-1, 0 cm	0–135.0	Holocene to early Pliocene	Silty clay	Silty clay with biosilica, silty clay with foraminifers, silty clay with sand
I	395-U1562C-1H-1, 0 cm, to 16H-4, 0 cm	0–135.23	Holocene to early Pliocene	Silty clay	Silty clay with biosilica, silty clay with foraminifers, silty clay with sand
II	395C-U1562A-16H-1, 0 cm, to 35F-1, 0 cm	135.0–253.1	early Pliocene to late Miocene	Silty clay, silty clay with carbonate	Silty clay with foraminifers, carbonate silty clay
II	395-U1562C-16H-4, 0 cm, to 42F-CC, 22 cm	135.23–251.49	early Pliocene to late Miocene	Silty clay, silty clay with carbonate	Silty clay with foraminifers, carbonate silty clay
III	395C-U1562A-35F-1, 0 cm, to 55F-4, 14 cm	253.1–351.36	late Miocene	Silty clay with carbonate, silty clay	Carbonate silty clay, carbonate mud
III	395-U1562C-44F-1, 0 cm, to EOH	253.4–300.68	late Miocene	Silty clay with carbonate, silty clay	Carbonate silty clay, carbonate mud
IV	395C-U1562A-55F-4, 14 cm, to 64X-CC, 33 cm	351.36–427.73	late Miocene	Nannofossil ooze, nannofossil chalk	Carbonate silty clay
IV	395C-U1562B-2R-1, 3 cm, to 4R-1, 147 cm	408.13–428.57	late Miocene	Nannofossil ooze, nannofossil chalk	Carbonate silty clay

Table T3. Clasts (>2 cm), Site U1562. **Download table in CSV format.**

Core, section, interval (cm)	Description
395C-U1562A-	
2H-1, 16–16	2 cm subrounded basalt
2H-1, 129–129	3 cm angular conglomerate
2H-3, 13–13	2 cm subrounded metasediment
2H-3, 14–14	2 cm angular metasediment
2H-4, 43–43	5 cm subrounded granite
2H-5, 49–49	2 cm angular conglomerate
14H-1, 86–86	Fractured, well-rounded soft-sediment clast
58X-1, 24–32	6 cm rounded basalt
58X-1, 24–32	3 cm rounded micrite
58X-1, 30–32	2 cm subangular microgranular dark reddish clast
59X-1, 0–4	4 cm amphibolite gneiss clasts
59X-1, 0–5	5 cm amphibolite gneiss clasts
60X-1, 0–5	4 cm metamorphic, possible gneiss clasts
61X-1, 0–5	5 cm angular gneiss
395-U1562C-	
3H-2, 8–54	3 cm granite clast at 15 cm
4H-3, 5–8	3 cm drop stone
14H-3, 117–119	2 cm basalt
30F-1, 1–5	5 cm metavolcanic clast
36F-1, 7–10	2 cm clast

ors for these same sediments in Hole U1562C were predominantly very dark gray, olive gray, and brown. The discrepancy in color is likely due to oxidation of the sediments prior to core description for Expedition 395C (core description occurred ~10 months after core recovery). Unit I exhibits relatively high frequency and amplitude variation in NGR values. In contrast, reflectance (L*) values exhibit little variability throughout this unit. The exception is the upper 30 m of sediment in which reflectance values are slightly more variable (L*, a*, and b*), coinciding with an interval in which foraminifers and biogenic silica are slightly more abundant and colors are slightly brighter (yellowish brown, pale brown, and gray; Cores 395C-U1562A-1H through 4H and 395-U1562C-1H through 4H). Nannofossils and foraminifers are present throughout the unit, although in highly variable amounts, consistent with variable $CaCO_3$ percent, which ranges from below ~1 to 83 wt% (average = 16 wt%). Biosilica is present throughout in varying but minor amounts. With respect to relative abundance within the biosiliceous component, sponge spicules are present in trace to abundant amounts, radiolarians are present in trace amounts, diatoms are present in trace to common amounts, and silicoflagellates are present in trace amounts. The terrigenous components are primarily quartz and feldspar. Glass, oxides, and uncommonly glauconite and inorganic calcite are also observed (Figure **F6A–F6C**). A thin glassy layer is observed in Section 395-U1562C-7H-5, 47 cm. Several sharp boundaries and graded beds with a fining-upward texture are present in Core 3H. Laminations are observed at the base of Section 12H-4 (128–148 cm), although these are clearer in X-Ray Linescan Logger (XSCAN) images than macroscopic observation (Figure **F7**). The cores of this unit show little drilling disturbance except for some soupy intervals in the topmost section of cores. Bioturbation is primarily sparse to moderate.

3.2. Lithostratigraphic Unit II

Intervals: 395C-U1562A-16H-1, 0 cm, to 35F-1, 0 cm; 395-U1562C-16H-4, 0 cm, to 42F-CC, 22 cm
Depths: Hole U1562A = 135.0–253.1 m CSF-A; Hole U1562C = 135.23–251.49 m CSF-A
Thickness: Hole U1562A = 118.1 m; Hole U1562C = 116.26 m
Age: early Pliocene to late Miocene
Lithology: silty clay, silty clay with carbonate
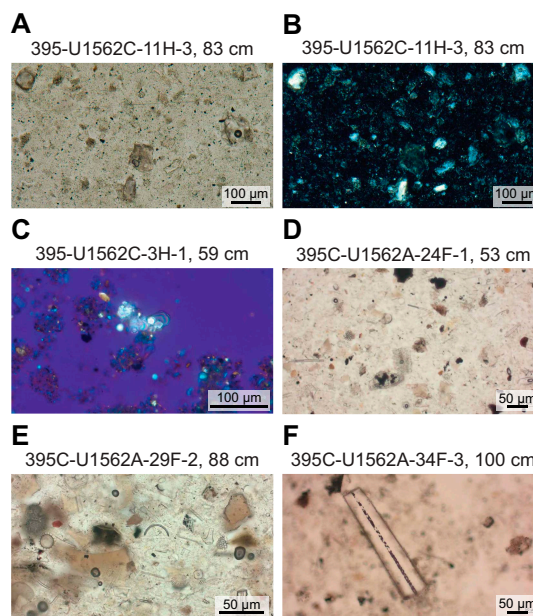
Figure F6. Unit I and II silty clay, calcite minerals, and sponge spicules, Site U1562. A, B. Silty clay with abundant terrigenous grains (e.g., quartz and feldspar) and traces of biosilica in Unit I in (A) plane-polarized light (PPL) and (B) cross-polarized light (XPL). C. Cluster of inorganic calcite minerals with gypsum plate in Unit I (XPL). D. Silty clay with opaque grains, glass, biosilica, and pyrite infilling of microfossils (radiolarian near bottom center) in Unit II (PPL). E. Silty clay with biosilica and abundant glass in Unit II (PPL). Some grains (lower left) have no vesicles, and others (upper right) have dark vesicles. F. Pyrite infilling of sponge spicule in Unit II (PPL).

Unit II is mainly light brownish gray, dark grayish brown, and grayish brown silty clay and silty clay with carbonate. As for Unit I, during Expedition 395 and for the same sequence of sediments from Hole U1562C, the colors described were more commonly dark or olive gray than brown. Although cycles in NGR values display lower amplitude and frequency in comparison to Unit I, reflectance (L*) values display higher amplitude variations (Figures **F4**, **F5**). $CaCO_3$ measurements are again variable with depth in this unit, ranging 7–55 wt% (average = 28 wt%). Beds of carbonate silty clay and silty clay with foraminifers (light gray, dark gray, or greenish gray) are found at intermittent depths, including in Cores 395C-U1562A-22F, 32F, and 33F and 395-U1562C-17H, 18H, 19H, 33F, 34F, and 42F. Disseminated pyrite is commonly observed in smear slides in this unit, often infilling siliceous and carbonate microfossils (Figure **F6D–F6F**). Although present throughout Site U1562, glass is more abundant in smear slides in Unit II than in Unit I (Figure **F6A, F6D, F6E**).

Several sharp contacts are observed near the interface between Units I and II. These contacts occur at several depths in Cores 395C-U1562A-16H through 18H and 395-U1562C-16H through 21F (Figure **F8A–F8H**). The most prominent contact in Hole U1562C, located in Section 16H-4A, 102 cm, has a thin (<0.5 cm), bright orange layer that displays abundant iron oxides in smear slide (Figure **F8F**). Other layers display thin (~1–3 cm) intervals of dark green, very fine grained material (Figure **F8E, F8G**). Occasional evidence of soft-sediment deformation is present in Sections 18F-2, 18F-3, 20F-2, 20F-3, 26F-1, 26F-2, 28F-2, and 40F-3 (Figure **F8I, F8J**). Sediment layers with abundant glass are also observed macroscopically (e.g., intervals 395C-U1562A-17H-4, 14–16 cm; 20H-7, 40–45 cm; 21H-1, 95–101 cm; and 395-U1562C-34F-3, 30–35 cm). Diffuse, dark gray blebs or layers that may contain glass are present but were more difficult to assess macroscopically because they do not present as distinct layers; time constraints prohibited shipboard smear slide analysis for all of these features (e.g., intervals 395C-U1562A-18H-6, 14–15 cm, and 21H-4, 42–44 cm). Small pumice and scoria clasts (<2 cm) were observed in Sections 30F-1, 107 cm, and 30F-2, 2, 43, and 102 cm. Bioturbation is generally slight to moderate in this unit. Some drilling disturbance is present, ranging from slight to severe deformation, although this is generally confined to short intervals at or near the tops of core sections.

3.3. Lithostratigraphic Unit III

> Intervals: 395C-U1562A-35F-1, 0 cm, to 55F-4, 14 cm; 395-U1562C-44F-1, 0 cm, to end of hole
> Depths: Hole U1562A = 253.1–351.36 m CSF-A; Hole U1562C = 253.4–300.68 m CSF-A
> Thickness: Hole U1562A = 98.26 m; Hole U1562C = 47.28 m
> Age: late Miocene
> Lithology: silty clay with carbonate, carbonate silty clay

Unit III is predominately silty clay and silty clay with carbonate, with intervals of carbonate silty clay and carbonate mud. This unit is defined by the abundance of features consistent with soft-
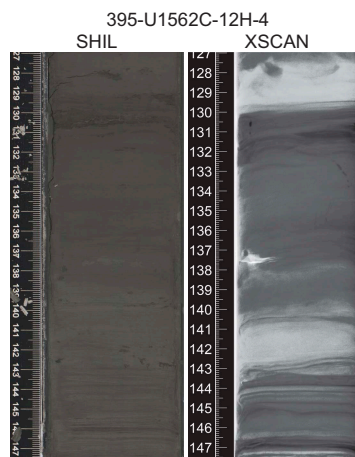

Figure F7. Comparison of laminations at the base of 395-U1562C-12H-4. SHIL = Section Half Imaging Logger.

sediment deformation throughout. Because the sediments are clay rich and homogeneous in appearance and lack well-defined bedding features such as laminae or cross-bedding, the deformation is primarily recognized by color contrasts between soft clasts of silty clay. The features observed include several distinctive layers of centimeter-scale lumps of silty clay resembling brecciated mud clasts, with or without matrix. Where matrix is present, it is of a similar texture to the clasts. The variable coloration of the sediment clasts, with interlocking, irregular blobs in matrix resembles the Camouflage Central-Europe pattern in some cores (e.g., 395C-U1562A-35F, 43F, 49F, 50F, 53F, and 54F) (Figure **F9A–F9C**). Other expressions of soft-sediment deformation and disorganization, such as convoluted layers, high-angle contacts (often with curvature) between differently colored layers, flow structures, dragging structures, folding, arching, and squeezing are present in the cores listed previously as well as in Cores 37F, 46F, 52F and 395-U1562C-44F, 45F, 49F, 50F, 51F, 52F, and 53F (Figure **F9D–F9F**). The extensive deformation observed across Unit III, combined with thinner intervals of apparently undisturbed sediment, gives the impression of a thick series of slumps separated by short intervals of quiescence.

$CaCO_3$ measurements are again highly variable in Unit III, ranging 3–65 wt% (average = 35 wt%), likely reflecting the incorporation of several layers of sediment with different initial depositional conditions into the slumps. Similar to Unit II, Unit III continues to present disseminated pyrite and glass in smear slides. A glass-rich layer is present at the base of a deformed layer in interval 395C-U1562A-37F-2, 66–68 cm. Small scoria clasts are present in Cores 37F, 53F, and 54F. Bioturbation ranges from absent to abundant. Drilling disturbance is minor in this unit; where present, it consists of slightly to moderately soupy or fragmented intervals, generally occurring in the uppermost few centimeters of cores.
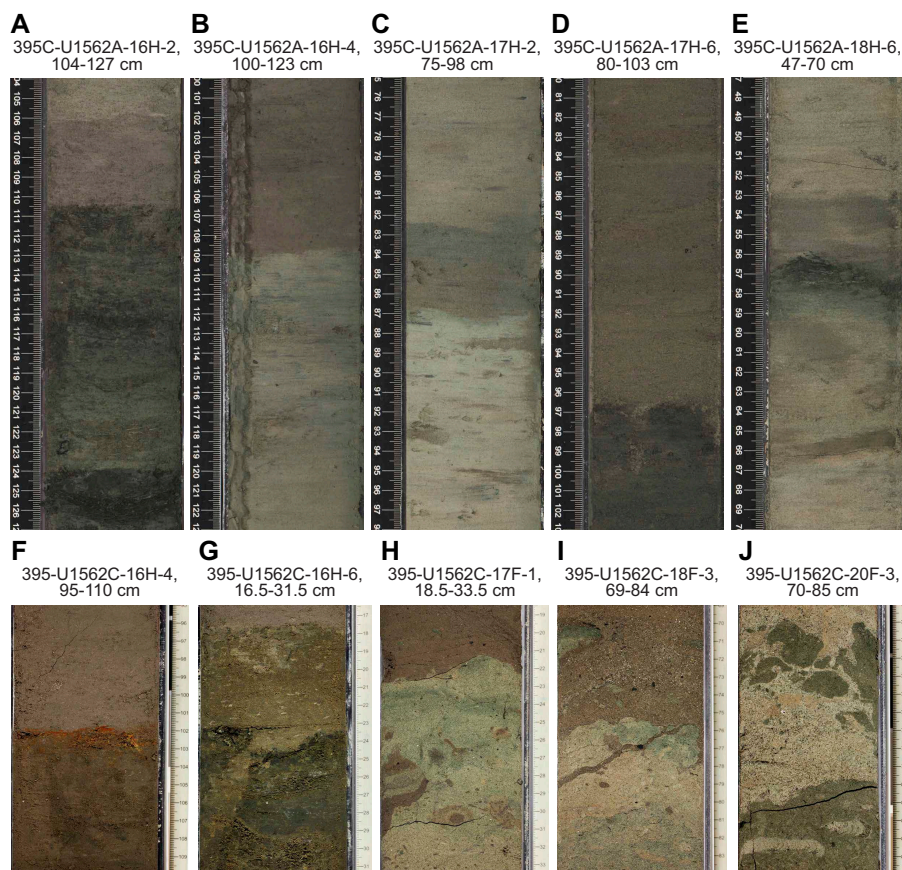
Figure F8. Sharp boundaries observed at the top of Unit II, Holes U1562A and U1562C. Close up images of most contacts were not made during Expedition 395C. However, all of the contacts shown in this image can be traced between Holes U1562A and U1562C.

3.4. Lithostratigraphic Unit IV

Intervals: 395C-U1562A-55F-4, 14 cm, to 64X-CC, 33 cm; 395C-U1562B-2R-1, 3 cm, to 4R-1, 147 cm

Depths: Hole U1562A = 351.36–427.73 m CSF-A; Hole U1562B = 408.13–428.57 m CSF-A

Thickness: Hole U1562A = 76.37 m; Hole U1562B = 20.44 m

Age: late Miocene

Lithology: nannofossil ooze, nannofossil chalk

Unit IV is predominantly characterized by light gray nannofossil ooze, transitioning to nannofossil chalk toward the base of the unit. This unit begins in Section 395C-U1562A-55F-4, 14 cm, at a sharp contact between the overlying deformed silty clays and the underlying nannofossil ooze (Figure **F10A**). Subordinate beds (<3 m thick) of carbonate silty clay are also present near the upper and lower sections of this unit. The base of this unit is in Section 395C-U1562B-4R-1, at approximately 147 cm (428.57 m CSF-A), because Core 4R includes the interface between chalk and basalt basement between Sections 4R-1 and 4R-2. Bulk $CaCO_3$ ranges 59–78 wt% (average = 64 wt%); however, one exception is an interval of carbonate clayey silt (Sections 395C-U1562A-64X-3 through 64X-5), which has approximately 37 wt% $CaCO_3$. Unit IV is moderately to abundantly bioturbated, with greenish mottling associated with burrows (Figure **F10B**). Green banding is present in many intervals. Bands do not exhibit a different composition in smear slides from the surrounding sediments and appear to crosscut most burrows, implying they are the result of changes in sediment oxidation postdeposition (Figure **F10C**). Drilling disturbance in this unit presents as slight to severe fragmentation, with the severity and abundance of disturbance increas-
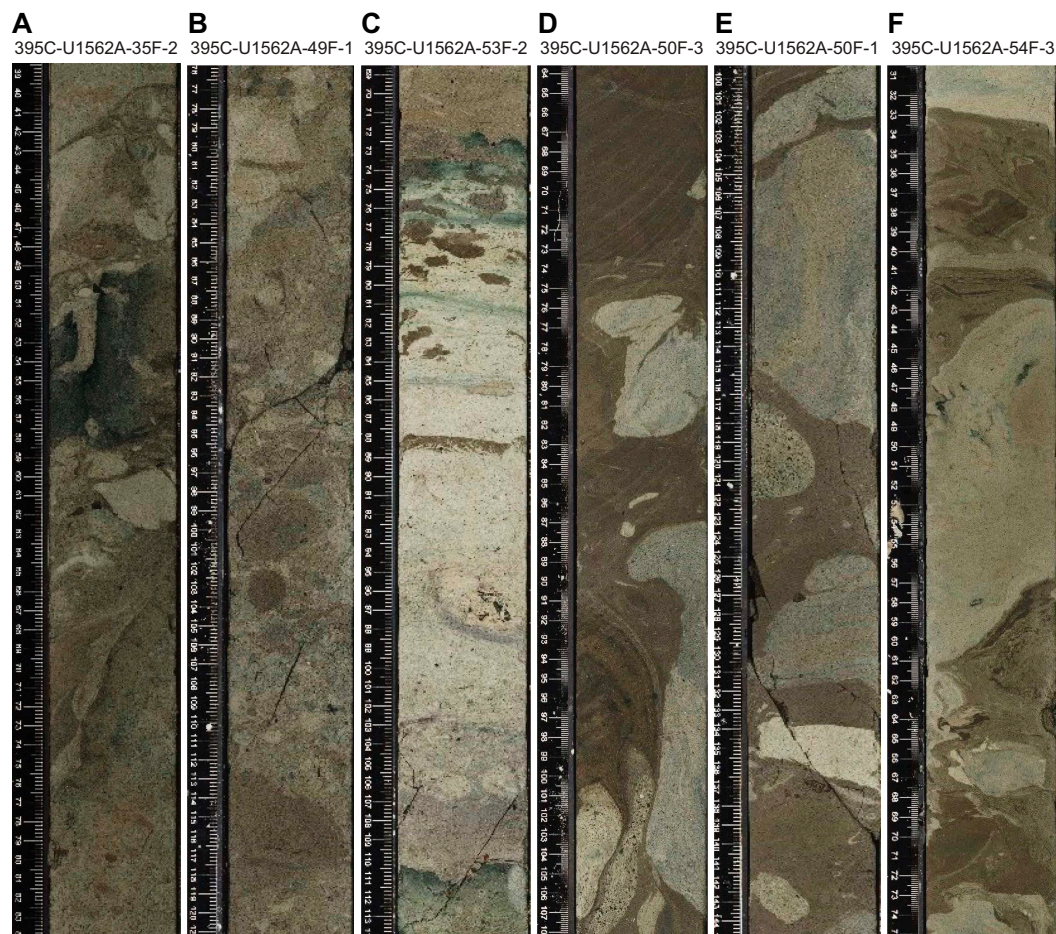
Figure F9. Evidence for possible soft-sediment deformation in Unit III, Site U1562. A–C. Brecciated mud clast-like features closely resembling the Camouflage Central-Europe pattern. D–F. Other disorganization features such as folding, squeezing (base of D), and sharp, high-angle contacts between contrasting colored sediment packages.

ing downcore. Core recovery is also reduced for Unit IV in comparison to the upper units, which likely relates to degree of lithification (Figure **F4**).

Three clasts are present in Section 395C-U1562A-58X-1A, 28 cm (Figure **F10D**): a 6 cm sub-rounded basalt clast, a rounded 3 cm micrite clast, and a 2 cm subangular microgranular dark reddish clast. All three clasts are likely the result of fall-in from shallower depths in the hole, based on their position near the top of the core and the observed drilling disturbance at this depth, and hence are unlikely to be in place. A glassy layer with a diffuse upper boundary was identified near the base of the sedimentary column in Unit IV in interval 61X-2, 62–64 cm (Figure **F10E**).

In the underlying basalt basement units, a 65 cm thick layer of highly fragmented nannofossil chalk was recovered (interval 395C-U1562B-14R, 0–65 cm). This layer is pale brown, abundantly bioturbated and contains occasional greenish yellow and black glass throughout.

3.5. XRD results

A subset of squeeze cake residue samples (*n* = 10) were analyzed using X-ray diffraction (XRD). Results are consistent with smear slide and macroscopic observations (Figure **F11**; Table **T4**). The amount of calcite implied by the diffraction patterns is variable but consistent with $CaCO_3$ weight percent measurements. Minerals identified at this site are consistent with the terrigenous and authigenic minerals observed in smear slide and include quartz, assorted feldspar and pyroxene, pyrite, and calcite. XRD samples were not specifically prepared for clay mineral analysis, and peaks with a 2θ of <15° should be treated with caution; however, most samples display peaks in this region, consistent with the presence of clay minerals. Future analysis of the clay mineralogy in these samples could be useful for determining shifts in deposition processes and sediment sources.
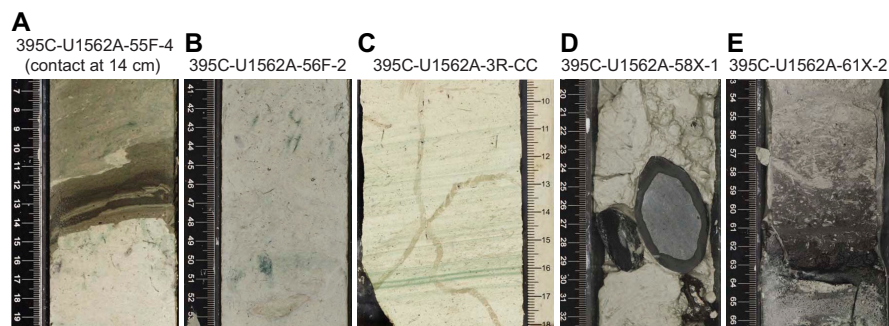
Figure F10. Sedimentary features from Unit IV, Hole U1562A. A. Unit III/IV contact. B. Green mottling observed in Unit IV, often associated with burrows. C. Green banding appearing to crosscut burrows (e.g., between 11 and 16 cm). D. Basalt, micrite, and granular red clasts found grouped near the top of 58X. E. Glass layer at ~63 cm >2 cm thick.
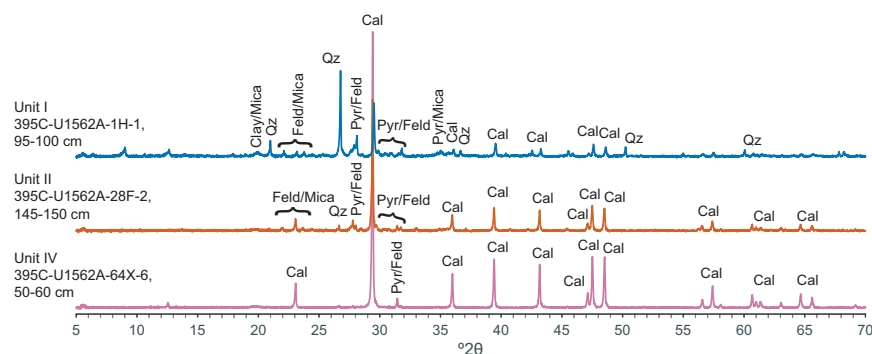
Figure F11. Powder XRD results, Hole U1562A. Sample composition is variable. Patterns are indicative of the range of terrigenous and carbonate mineral assemblages. Mineral assemblage from the base of the sediment sequence is mainly calcite. Cal = calcite, Pyr = pyroxene, Feld = feldspar, Qz = quartz.

Table T4. XRD results, Site U1562. **Download table in CSV format.**

Core, section, interval (cm)	Sample ID	Major minerals
395C-U1562A-		
1H-1, 95–100	CAKE10970411	Quartz, calcite, feldspar, mica, pyroxene
6H-2, 145–150	CAKE10972721	Quartz, calcite, feldspar, pyroxene
13H-2, 145–150	CAKE10975891	Calcite, quartz, pyroxene, feldspar
17H-2, 145–150	CAKE10977711	Calcite, feldspar
21H-2, 145–150	CAKE10979541	Calcite, pyroxene, feldspar
28H-2, 145–150	CAKE10981741	Calcite, feldspar
36F-2, 145–150	CAKE10983671	Calcite, quartz, feldspar, pyrite
44F-2, 146–151	CAKE10985661	Calcite, feldspar
52F-2, 145–150	CAKE10987691	Calcite, feldspar
64X-6, 50–60	CAKE10992051	Calcite
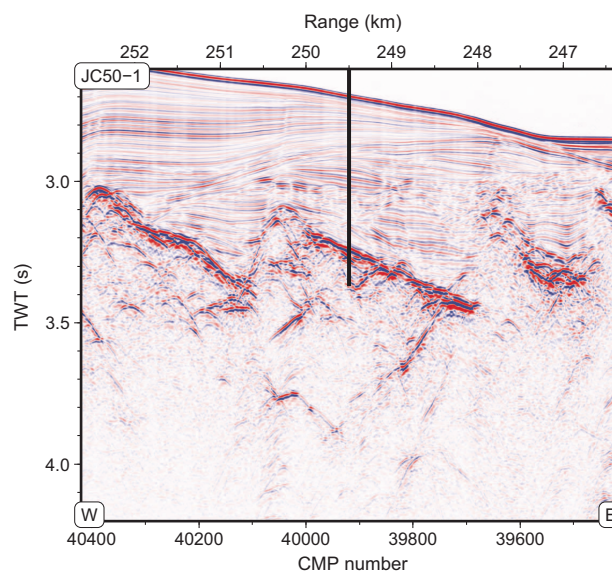
Figure F12. Site U1562 location on Seismic Line JC50-1.

4. Igneous petrology

Site U1562 is located on the western edge of VSR 3, where the estimated basement age is 13.9 Ma. This site is located near a series of normal faults that dip toward the northwest (Figure **F12**). Basalt coring in Hole 395C-U1562B reached ~560 m CSF-A (~130 m into basement) with 48% recovery (Figure **F13**). The sediment/basement contact was not recovered, but a quasi-interface with a small amount of glassy basaltic pillow fragments and breccia (<1 m) was sampled at the base of Hole 395C-U1562A.

4.1. Lithostratigraphy

Igneous rock cores from Site U1562 are mostly pillow basalts (>54%), with several thick sheet flow intervals recovered at 446–458 and 517–527 m CSF-A. Overall, the recovered basalts are sparsely to moderately olivine phyric, with some intervals also containing small plagioclase phenocrysts. Cores from this site also contain abundant peperite and intercalated sediment (Figure **F13**).

Hole U1562A reached the sediment/basement interface at ~427.7 m CSF-A, where white calcareous ooze lies on top of glassy basalt fragments in Section 64X-CC. The underlying core recovered a weathered vesicular sheet flow of sparsely olivine phyric basalt.

Hole U1562B encountered the sediment–basement transition at 428.6 m CSF-A and reached a maximum depth of 559.5 m CSF-A within basement. Recovered material is primarily composed of sparsely to moderately olivine phyric basalt with significant amounts of intercalated carbonate and peperite fragments. Material from this hole is mostly pillow basalt, which makes up more than half the total recovery. It is typically hypocrystalline with chilled margins and mottled devitrification. Thin glass rinds are common, with some larger glass rinds and shards up to 3 cm thick. The pillows are mostly sparsely vesicular, with a few intervals ranging up to ~10% vesicularity. Vesicles commonly occur in bands near the edges of flows or pillow lobes. Peperite and intercalated carbonates are also common, with multiple regions of sediment-rich recovery. Peperites and lava breccias make up ~12% of the total volume of volcanic recovery. The peperites exhibit a variety of features indicative of sediment-lava interaction (e.g., Skilling et al., 2002), including abundant basalt clasts with quenched glassy rims, fluidal margins, sediment intrusion into cracks and vesicles, and baked carbonate matrixes. There are several sheet flows (as thick as 10 m) that are generally nonvesicular aside from large sparse vesicles concentrated at flow boundaries. These flows are
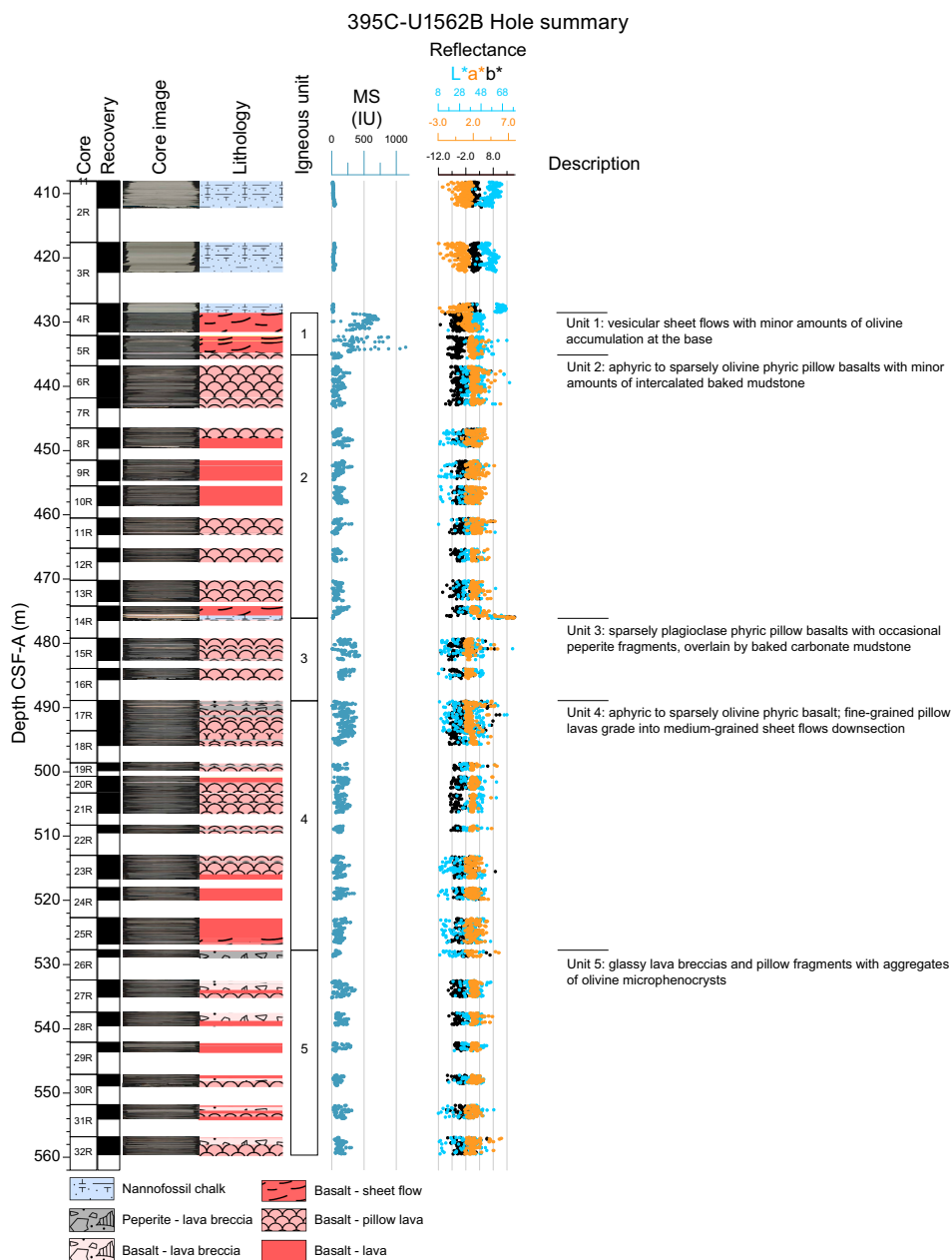
Figure F13. Lithostratigraphic summary, Hole U1562B. See Physical properties for detailed reflectance data.

sparsely to moderately olivine phyric with medium-grained interiors that grade to fine-grained chilled margins at flow boundaries. As at other Expedition 395 sites, these sheet flows also exhibit higher magnetic susceptibility (MS) and higher L* color reflectance than pillow lava intervals (Figure **F13**; see **Physical properties**). Most basalts show slight to moderate alteration with carbonate veins throughout (see **Alteration petrology and structural geology**). Sections 395C-U1562B-8R-2 and 10R-1 have strongly altered vesicular flow tops.

4.2. Core descriptions

Descriptions are based on a combination of detailed macroscopic observations of core sections, microscopic thin section observations, and physical properties measurements (e.g., MS, color reflectance, and wireline logs). Significant characteristics are summarized in the visual core descriptions (VCDs).

Igneous lithologies at Site U1562 are divided into three principal morphologic categories: pillow lavas, sheet flows, and peperites (Figures **F14**, **F15**). Pillow lavas consist of aphyric to sparsely olivine-phyric basalt fragments characterized by chilled curved margins, concentric vesicle bands, and thin glass rinds. Sheet flows recovered at this site are 2–10 m thick with coarser groundmass interiors. Approximately ~25% of the recovered lava is not assigned a flow morphology because of ambiguity distinguishing thin sheet flows from large pillows and lobate flows. Vesicles are sparsely to moderately abundant, often filled, and commonly occur in aligned bands. Veins and fractures frequently contain clay, celadonite, and Fe-oxide, with variable extents of background alteration (see **Alteration petrology and structural geology**).

Peperitic layers are characterized by glass shards and lava fragments in a carbonate matrix and show evidence for lava-sediment interaction (e.g., baked sediment, basalt fragments with quenched rims, and fluidal margins). These units often contain abundant fresh glass shards and fragments. Thick glass rinds (>1 cm) are relatively abundant in this core. In addition to peperitic intervals, some horizons contain lava breccias that lack clear evidence for lava-sediment interaction. Occasionally, there are thin layers of intercalated calcareous mudstone, which is sometimes
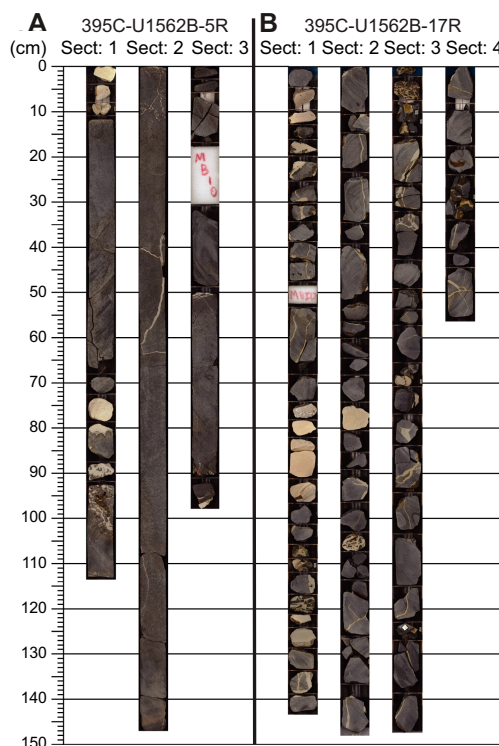

Figure F14. Common lithologies, Hole U1562B. A. Sheet flows with intercalated sediment. B. Pillow lavas with intercalated sediment and peperite fragments.

brecciated. A 65 cm thick layer of mudstone was recovered in Section 395C-U1562B-14R-2 at ~475 m CSF-A.

We used the presence of sediment-rich horizons (i.e., significant intercalated sediment or peperite) and mineralogical changes (e.g., olivine-phyric to plagioclase-phyric basalt) to divide the basement succession into igneous lithologic units (Table **T5**). Because of incomplete recovery and a general lack of well-defined contacts, our unit boundary locations are approximate and preliminary. We note that the cores with the lowest recovery are associated with pillow fragments, peperites, and/or intercalated sediment. This pattern is consistent with preliminary observations from the downhole logging data (see **Downhole measurements**), which show broad correlations between recovery rate, rock density, and lava morphology.

4.2.1. Hole U1562A

Less than 1 m of basement was recovered at the base of Hole U1562A, consisting of glassy basalt fragments overlying a weathered and vesicular sheet flow.
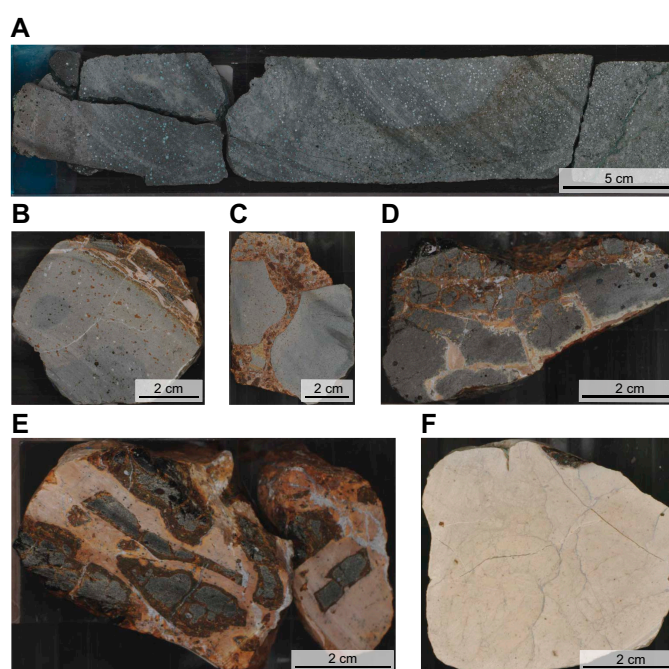
Figure F15. Typical lithologies, Hole U1562B. A. Vesicular sheet flow top (4R-2A, 0–31 cm). B. Small pillow lava fragment with 1 cm thick glass rind (19R-1A, 36–43 cm). C. Fracture between two pillow fragments filled with altered peperitic material (32R-1A, 43–52 cm). D. Pillow fragment with network of peperitic and carbonate veins, mostly empty vesicles, and thick glass rind (24R-2A, 35–39 cm). E. Peperite with glass rinds around basalt clasts (24R-1A, 79–83 cm). F. Baked carbonate mudstone with a network of thin veins (17R-2A, 75–81 cm).

Table T5. Igneous lithologic units, Hole 395C-U1562B. **Download table in CSV format.**

Unit	Interval	Depth CSF-A (m)	Description
	395C-U1562B-		
L1	4R-2, 0 cm, to 5R-2, 148 cm	428.57–434.72	Vesicular sheet flows with minor amounts of olivine accumulation in the base
L2	5R-3, 0 cm, to 14R-1, 134 cm	434.72–475.54	Aphyric to sparsely olivine phyric pillow basalts with minor amounts of intercalated baked mudstone
L3	14R-3, 0 cm, to 16R-2, 34 cm	476.2–485.68	Sparsely plagioclase phyric pillow basalts with occasional peperite fragments overlain by baked carbonate mudstone
L4	17R-1, 0 cm, to 26R-1, 7 cm	485.9–527.77	Aphyric to sparsely olivine phyric basalt; fine-grained pillow lavas grade into medium-grained sheet flows downsection
L5	26R-1, 7 cm, to 32R-2, 140 cm	527.77–559.6	Glassy lava breccias and pillow fragments with aggregates of olivine microphenocrysts

4.2.2. Hole U1562B

This hole can be divided into five igneous lithologic units (Figure F13; Table T5). The top is marked by a ~6 m thick altered vesicular sheet flow with minor amounts of olivine accumulation at its base (Unit 1). This sheet flow is underlain by a series of aphyric to sparsely olivine phyric pillow lavas with a thin sheet flow at the base and minor amounts of intercalated baked mudstone (Unit 2). Unit 2 overlies over half a meter of variably baked mudstone with manganese spots at ~475 m CSF-A. This sediment horizon forms the boundary between Units 2 and 3. Unit 3 consists of ~12 m of pillow basalts with sparse plagioclase and olivine phenocrysts intermixed with occasional peperite fragments. This basalt interval is underlain by another sediment-rich peperite horizon, beneath which Unit 4 includes almost 40 m of aphyric to sparsely olivine phyric basalt dominated by fine-grained pillows, which grade into a medium-grained sheet flow near the base of the unit. Another notable peperite interval (>1 m thick) forms the boundary between Units 4 and 5. Unit 5 consists of glassy lava breccias and pillow fragments that contain olivine microphenocryst conglomerates. This lowermost unit had low recovery to the base of the hole.

4.3. Thin sections

Thin sections were sampled from Hole U1562B with an average spacing of ~7 m (see **Core descriptions**), resulting in 18 thin sections, mostly from pillow lavas. They are, on average, sparsely to moderately olivine phyric (<10%) with relatively little alteration (Figure F16). Olivine phenocrysts range from small microphenocrysts to large, euhedral olivines up to ~4 mm across. Skeletal and swallowtail olivines are common in the groundmass, indicating rapid cooling. Plagioclase is the most abundant groundmass mineral, usually forming acicular or skeletal crystals without significant zoning. Thin sections from Igneous Lithologic Unit 3 contain twinned plagioclase phenocrysts up to ~2 mm long. The groundmass usually exhibits intergranular and intersertal textures containing clinopyroxene-bearing mesostasis, opaque oxides, and altered glass. Thin sections sampled from sheet flows are variable but tend to have a more crystallized groundmass with plagioclase, clinopyroxene and opaque oxides. Vesicles occur in low abundances (usually <5%) and are often filled with secondary phases such as calcite and celadonite (see **Alteration petrology and structural geology**).

4.4. Geochemistry

Shipboard measurements on basalts from Hole U1562B include portable X-ray fluorescence (pXRF) and inductively coupled plasma–atomic emission spectroscopy (ICP-AES) analyses (see **Geochemistry and microbiology** in the Expedition 395 methods chapter [Parnell-Turner et al., 2025a]).

The pXRF analyses were primarily used for preliminary characterization of the hole during shipboard operations. Raw counts from pXRF analyses are shown in Figure F17. Despite significant scatter, major elements such as Mg, Al, and Si roughly group into several clusters with offsets that sometimes align with our lithostratigraphic unit boundaries. Although we caution against overin-
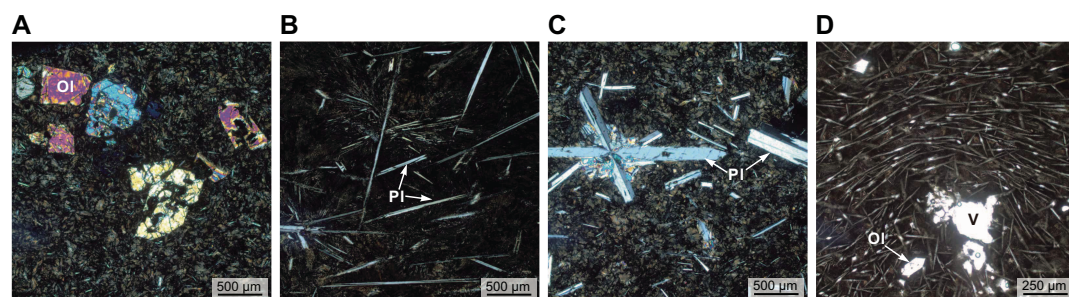

Figure F16. Basalt thin sections in (A–C) XPL and (D) PPL, Hole U1562B. A. Pillow lava showing skeletal olivine (Ol) phenocrysts in a cryptocrystalline groundmass (20R-2W, 96–99 cm). B. Glassy domain in a sheet flow (5R-1W, 23–26 cm). Pl = plagioclase. C. Elongate, twinned plagioclase laths in pillow lava (15R-3W, 25–28 cm). D. Pillow lava with dendritic olivines showing flow alignment (12R-1W, 96–99 cm). V = vesicle.

terpreting raw pXRF data, we note that the Unit 3 to 4 transition (~485 m CSF-A) is marked by slight increases in Mg, Al, and Si, as well as increases in incompatible trace elements such as Ti, Y, and Zr. On average, Unit 3 has slightly lower incompatible element concentrations than the other units, with another possible decrease in incompatible elements across the Unit 4–5 transition (~528 m CSF-A).

Similar geochemical offsets are also weakly reflected in ICP-AES analyses, which were performed on 18 samples that are co-located with the thin sections. Measurements of select major and trace elements are shown in Figure F18. MgO varies from 8.47 to 9.88 wt% with an average value of
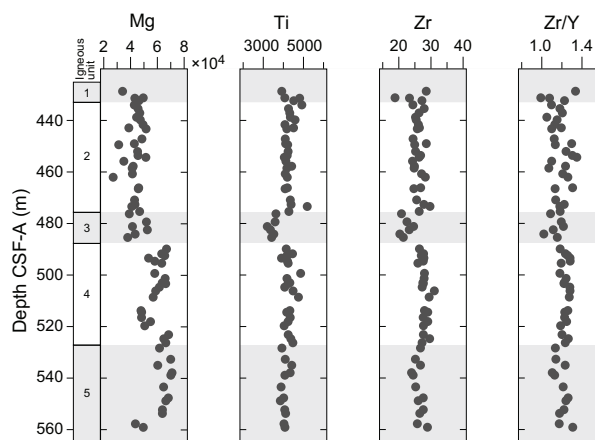
Figure F17. pXRF compositional data (raw counts) for selected major and trace elements, Hole U1562B.
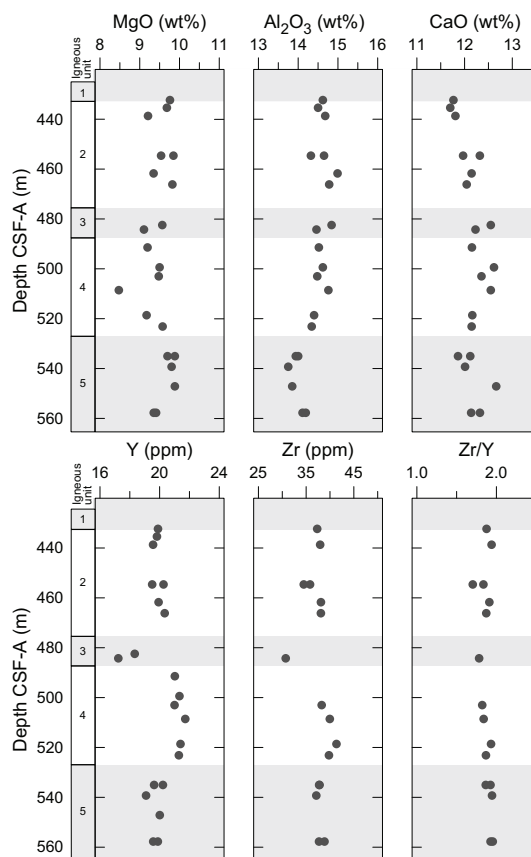
Figure F18. Bulk rock ICP-AES analyses for selected major and trace elements, Hole U1562B.

~9.49 wt%. Average Zr/Y is ~1.9, consistent with values from VSR basalts dredged from the ridge axis (Murton et al., 2002; Jones et al., 2014).

4.5. Correlations and interpretation

Core description results are combined with thin section observations, physical properties, downhole logging results, and shipboard geochemical analyses to develop a preliminary interpretation of Site U1562. As found at other sites, there is a weak correlation between MS and lithology (see **Physical properties**), with sheet flows exhibiting higher MS on average than pillow lavas and peperites (Figure **F13**). This correlation is probably caused by greater abundance of Fe-oxides (e.g., magnetite and titanomagnetite) within sheet flows. Similarly, sheet flows exhibit slightly higher L* color reflectance (Figure **F13**) and alteration extents (see **Alteration petrology and structural geology**) on average.

Hole U1562B had a markedly higher recovery rate than the other VSR hole, Hole U1563B (48% and 29%, respectively). However, we note that Hole U1563B also had a significantly higher proportion of sediment and peperite in the cores, which tend to be associated with lower recovery. Coring may preferentially sample peperitic zones where the carbonate matrix is baked and rich in basalt clasts and much of the surrounding sediment material is lost. Similarly, recovery of the one known sediment horizon of any significant thickness is incomplete: a mudstone layer ~65 cm thick was recovered from ~475 m CSF-A, but the downhole image log suggests that this sediment layer is probably ~3 m thick (see **Downhole measurements**). This sediment layer defines the boundary between Igneous Lithologic Units 2 and 3 and likely represents a significant hiatus between eruptions for such thick sediment accumulation. Assuming the average sedimentation rate estimated for the base of Hole U1562A, it would take on the order of ~10^5 y to accumulate several meters of sediment, suggesting that the upper basalt sequence is significantly younger than the lower basalt sequence. This observation is also consistent with biostratigraphic analyses of foraminifers, nannofossils, and bolboforms, which indicate this sediment layer is older than the sediment near the sediment/basement contact (see **Micropaleontology**).

Multiple horizons of peperite were recovered, indicating that lava has repeatedly flowed or erupted into carbonate ooze at this site. The prevalence of sediment at Sites U1562 and U1563 is significant, given that both are VSRs and thus thought to have higher average magma supply than the VST sites. One might therefore expect more frequent eruptions with less time for sediment accumulation than at Sites U1554 and U1555. Instead, there must be a significant amount of sediment accumulation at this site to produce peperite and mudstone intervals multiple meters thick. We speculate that the VSR sites may be sampling late stage off-axis eruptions or eruptions that flowed off-axis into already sedimented areas.

5. Alteration petrology and structural geology

At Site U1562, ~0.78 and ~65.39 m of basement core was recovered from Holes 395C-U1562A and 395C-U1562B, respectively. Here, we provide a visual description of the style and composition of basalt alteration and secondary mineral fill of their vesicles and document the occurrence and mineral fill of fractures from the basement cores.

5.1. Basalt alteration

Basalt from Site U1562 contains numerous intervals of intermixed peperite and completely altered carbonate sediments, which comprise ~2.4% of the recovered basement core at this site. Peperites at Site U1562 have a matrix of altered carbonate sediments that contain fragments of basalt and basaltic glass (see **Igneous petrology**). The alteration reported here is for basalt core and the basalt fragments in the peperite intervals.

We estimate that ~72% of the basalt core obtained from Holes U1562A and U1562B is slightly altered, 18% moderately altered, 8% highly altered, ~2% completely altered, and <1% unaltered basalt (Figure **F19**). The predominant alteration style of the basalt at Site U1562 is pervasive (background) (Figure **F20**). Alteration halos around fractures appear frequently at ~461–533 m

CSF-A in Hole U1562B, and localized patches of alteration are commonly observed at 434–461 and 533–553 m CSF-A. Alteration intensity at Site U1562 does not show any obvious correlation to basement core lithology (see **Igneous petrology**).

The most commonly occurring basalt alteration mineral assemblage at Site U1562 consists of Fe-oxide/oxyhydroxides + phyllosilicate and celadonite (Figure **F20**). Celadonite occurs as a minor component of the alteration assemblage at various depths in Hole U1562B. Rims of basalt clasts in peperite intervals display strong to complete alteration to palagonitic material (rich in Fe-oxide/oxyhydroxides), which in some clasts decreases in intensity toward their centers. In thin section, olivine phenocrysts are variably altered to a pale brown to green saponite phase or idding-sitized (Figure **F21A, F21B**). The basaltic groundmass appears variably altered mainly to smectite, likely saponite and Fe-saponite, celadonite, and Fe-celadonite (Figure **F21C, F21D**). Disseminated
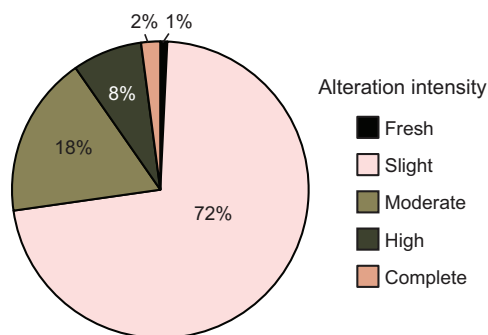
Figure F19. Proportional intensity of basalt alteration for all cores, Site U1562.

Figure F20. Lithologic interpretation and units, Hole U1562B, and alteration intensity variation, Holes U1562A and U1562B. (See Igneous petrology.)
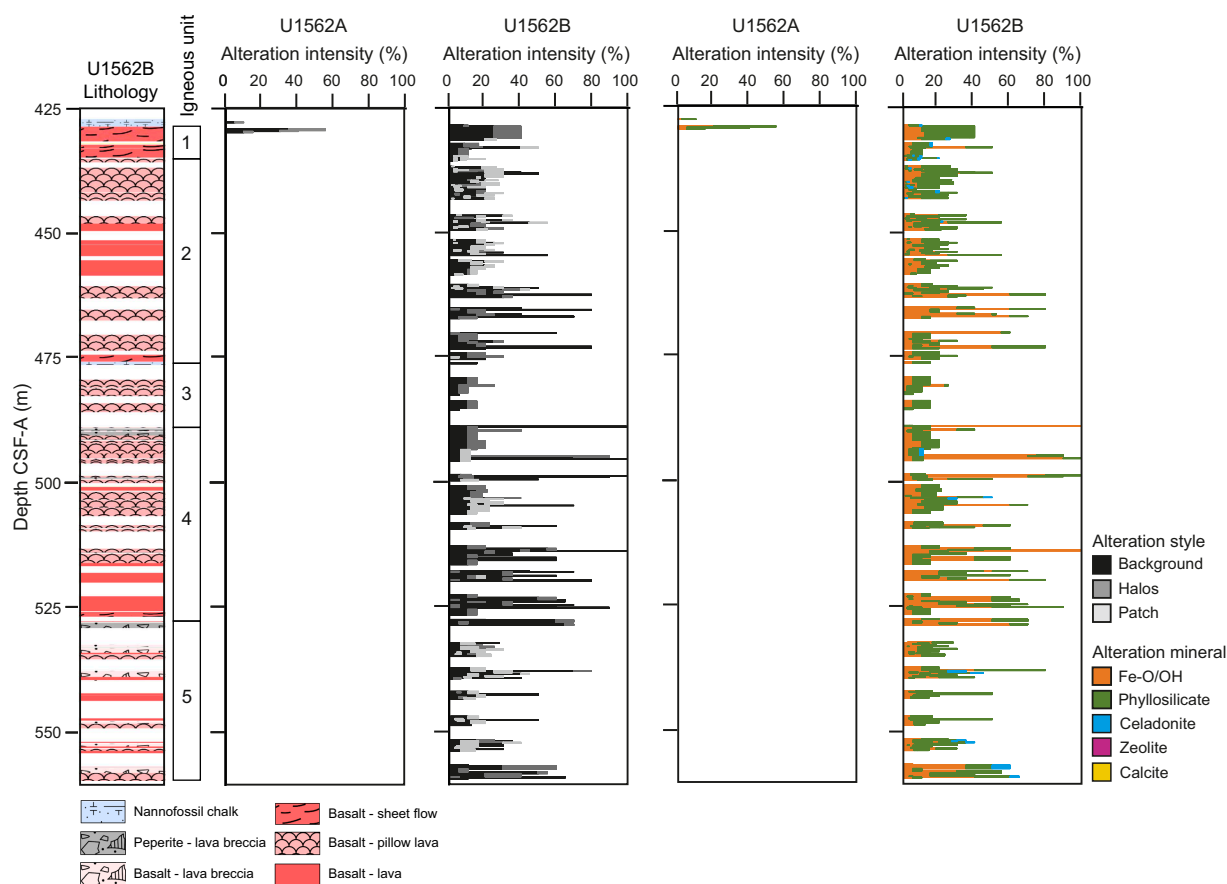
magnetite is observed, some of which has a dendritic morphology, along with common oxide phases.

An altered olivine from thin section Sample 395C-U1562B-17R-2, 109–112 cm, was analyzed with energy dispersive spectrometry (EDS). Elemental maps of the altered olivine were acquired (Si, O, Al, Ca, Mg, Fe, K, and Na), and two zones of interest on the altered olivine were analyzed for their EDS spectra to better characterize the alteration (Figure F22). Zone 1 shows strong spectral peaks
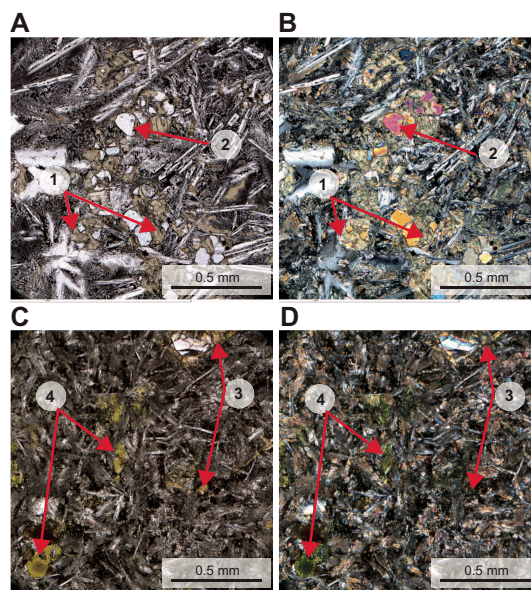

Figure F21. Alteration, Hole U1562B. A, B. Saponite/chlorite alteration (1) of olivine (2) (5R-1, 23–26 cm). C, D. Saponite alteration (3) and celadonite alteration (4) (17R-2, 109–112 cm). Left: PPL, right: XPL.
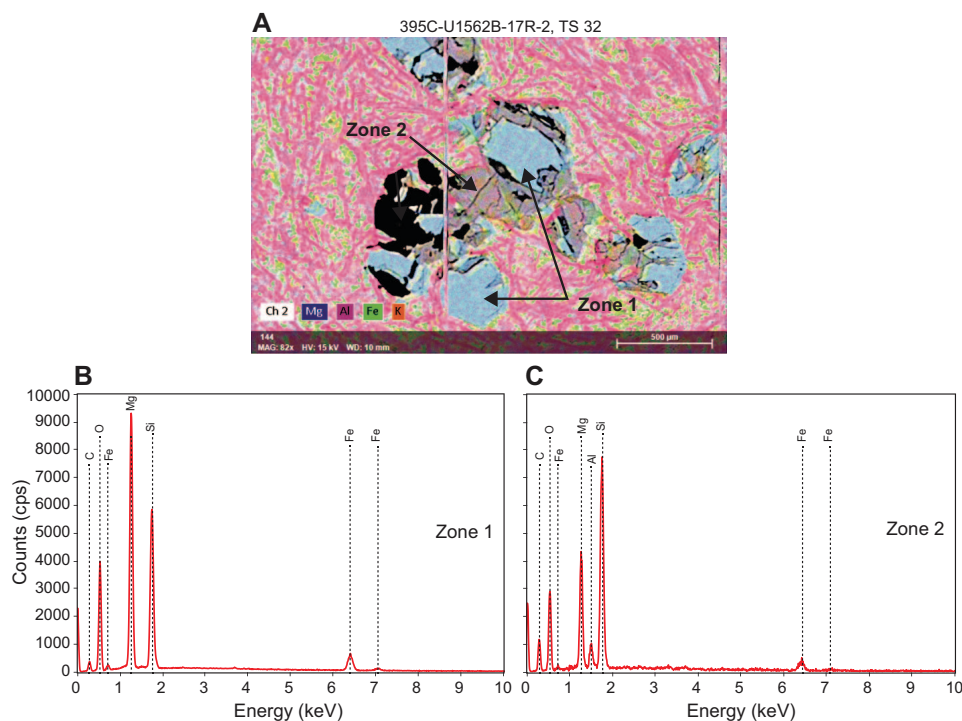
Figure F22. Altered olivine (395C-U1562B-17R-2, 109–112 cm). A. EDS element map showing secondary electron map overlaid with Mg, Al, Fe, and K chemistry maps. B, C. EDS spectra of (B) Zone 1 and (C) Zone 2. cps = counts per second.

for Mg, Si, and O with minor Fe. Zone 2 shows strong spectral peaks for Si, Mg, and O with minor Al and Fe and very minor Ca. Zone 1 represents unaltered olivine, close to the forsterite end-member, and Zone 2 is interpreted to be parts of the olivine phenocryst undergoing saponitization by replacement of Mg with Si, Al, and Ca.

The fraction of vesicles filled with alteration minerals varies between 10% and 100% at Site U1562. Vesicle-filling minerals are mostly Fe-oxide/oxyhydroxides, celadonite, and calcite, with moderate saponite and minor zeolite (phillipsite) (Figure **F23**). Thin section Sample 395C-U1562B-30R-1, 4–7 cm, displays calcite-filled vesicles with saponite spherules on their rims, with an outer celadonite rim (Figure **F23G, F23H**), as well as other vesicles containing calcite and a zeolite phase tentatively identified as phillipsite (Figure **F23C**). The mineral fill of most vesicles shows a color zonation, with Fe-oxide/oxyhydroxides or saponite rims to celadonite-filled vesicles presenting a range of colors from pale blue to pale green. Dark blue celadonite is uncommon in vesicles from Hole U1562B. There is no correlation between the percentage of vesicles filled and the alteration intensity of the basalt core at Site U1562. Some vesicles show <1 mm wide alteration halos in the basalt around them.

Vesicles with multiple infilling minerals from thin section Sample 395C-U1562B-30R-1, 4–7 cm (shown in Figure **F23G, F23H**), were analyzed using EDS (Figure **F24**). Elemental maps (Si, O, Al, Ca, Mg, Fe, K, and Na) and EDS spectra from two zones of interest were examined to better characterize the vesicle alteration mineralogy (Figure **F24C, F24D**). In Zone 1, a spherule-like material in the vesicles shows strong spectral peaks for Ca and O and minor peaks for Si, Al, Mg, and Fe. Zone 2 shows strong spectral peaks for Ca and O with minor Mg. Zone 2 can be inferred to represent Mg-calcite, and Zone 1 may represent a chlorite/smectite composition for the spherules on the edge of the vesicle, although the EDS spectra also contain signals of the Mg-calcite infill that may extend underneath the clay on the thin section. The K map highlights the presence of celadonite around the vesicle rims (between the chlorite/smectite spherules and Mg-calcite fill).

5.2. Structural geology

Fracture analysis at Site U1562 revealed 6 fractures in Hole U1562A (Section 64X-CC and Core 65X) and 1399 fractures in basement core from Hole U1562B. For Hole U1562B, an occurrence rate of ~21 fractures per meter of recovered core is reported (~17–18 fractures per meter of
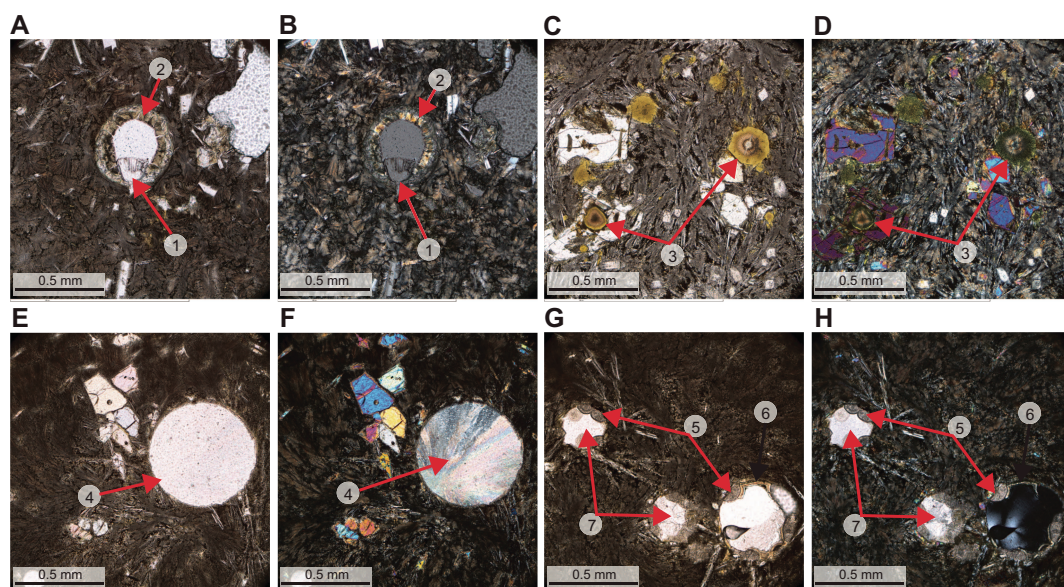

Figure F23. Vesicles, Hole U1562B. A, B. Vesicle filled with phillipsite (1) and a smectite rim (2) in (A) PPL and (B) XPL (15R-3, 25–28 cm). C, D. Layered vesicle (3) showing celadonite zonation in (C) PPL and (D) XPL (32R-1, 94–97 cm). E, F. Vesicle filled with calcite (4) in (E) PPL and (F) XPL (30R-1, 4–7 cm). G, H. Layered vesicles displaying smectite spherules (5), celadonite rims (6), and calcite infilling (7) in (G) PPL and (H) XPL (30R-1, 4–7 cm).

curated core). Fracture density seems invariant with depth, with only few local exceptions of low-fracture density at ~432, ~454, ~475, ~485, and 548 m CSF-A (Figure F25). Most fractures recorded at Site U1562 have widths ≤0.5 mm (64%) (Figure F26). The widest fractures recorded include two 8–10 mm wide carbonate-filled fractures in Hole U1562B (Figure F27). Most frac-
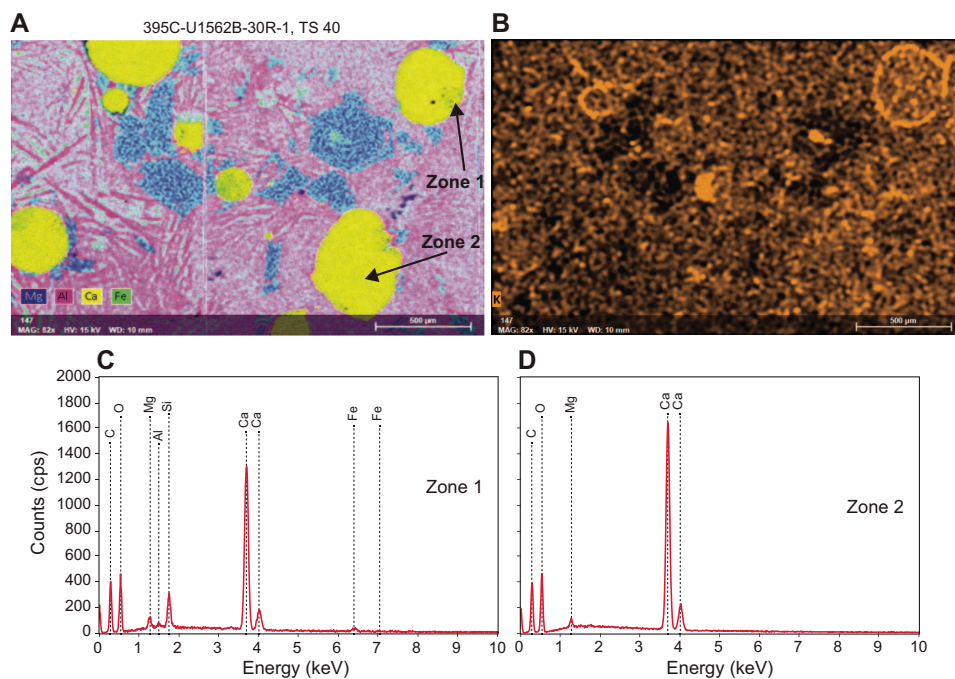

Figure F24. Calcite-filled vesicles with chlorite/smectite spherules and celadonite rims (395C-U1562B-30R-1, 4–7 cm). A. EDS element map displaying overlaid Mg, Al, Ca, and Fe chemistry. B. EDS K map displaying K-rich celadonite at vesicle rims. C. EDS spectrum of Zone 1. D. EDS spectrum of Zone 2. cps = counts per second.
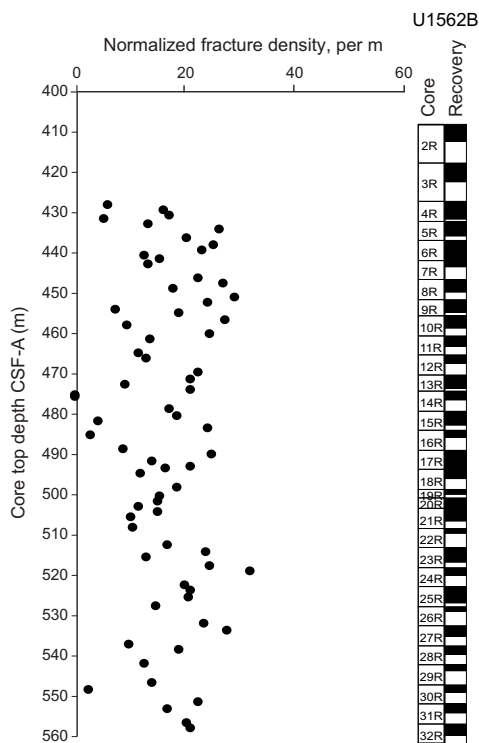
Figure F25. Fracture density normalized by curated section length, Hole U1562B.

tures are classified as partially open (42.2%) or veins (37.6%) with anastomosing (41.4%) or planar (45.5%) shapes, and most fractures are observed to exist in a crosscutting network (52%) (Figure **F28**). Fracture attitude was not recorded for this site because of time constraints during core description.

Fracture mineral fill classification was determined by color, visual inspection under a hand lens, and reaction to dilute HCl acid. In Hole U1562A, the mineral fill of the six fractures measured is primarily cryptocrystalline to microcrystalline carbonate ± Fe-oxide/oxyhydroxide ± celadonite. In Hole U1562B, the mineral fill of the 1399 documented fractures is mainly cryptocrystalline to microcrystalline carbonate ± Fe-oxide/oxyhydroxide with minor occurrences of phyllosilicate and celadonite (Figures **F29**, **F30A**). In thin section, some Fe-oxide/oxyhydroxide and celadonite fracture fills are observed (Figure **F30B**). Peperite and altered carbonate sediment intervals show a later stage of brittle deformation resulting in the formation of carbonate veins (Figure **F30C**). These carbonate veins commonly cut through the carbonate matrix around the basaltic fragments but occasionally also cut through the basaltic fragments. Fracture alteration halos range 1−20 mm wide with colors from brown, pale gray, green-gray, to green-brown. The mineral fill of vesicles in these alteration halos is mostly carbonate and phyllosilicate rich with some celadonite and Fe-oxide/oxyhydroxides.
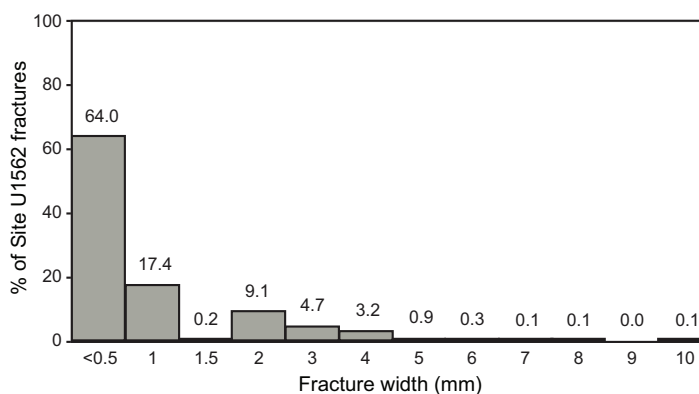

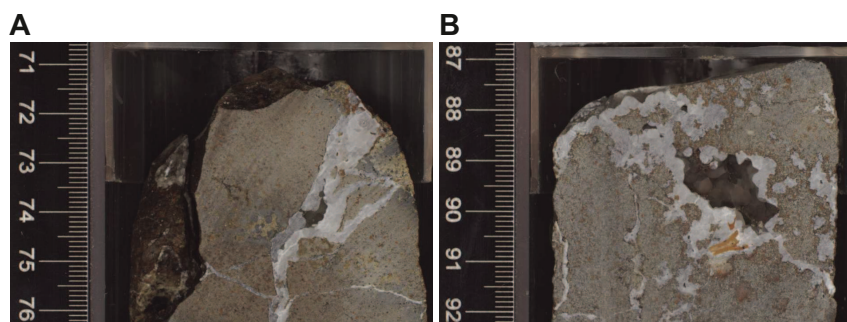**Figure F26.** Fracture width distribution, Site U1562.

Figure F27. Carbonate filled fractures, Hole U1562B. A. 30R-1, 71–76 cm. B. 31R-1, 87–92 cm.
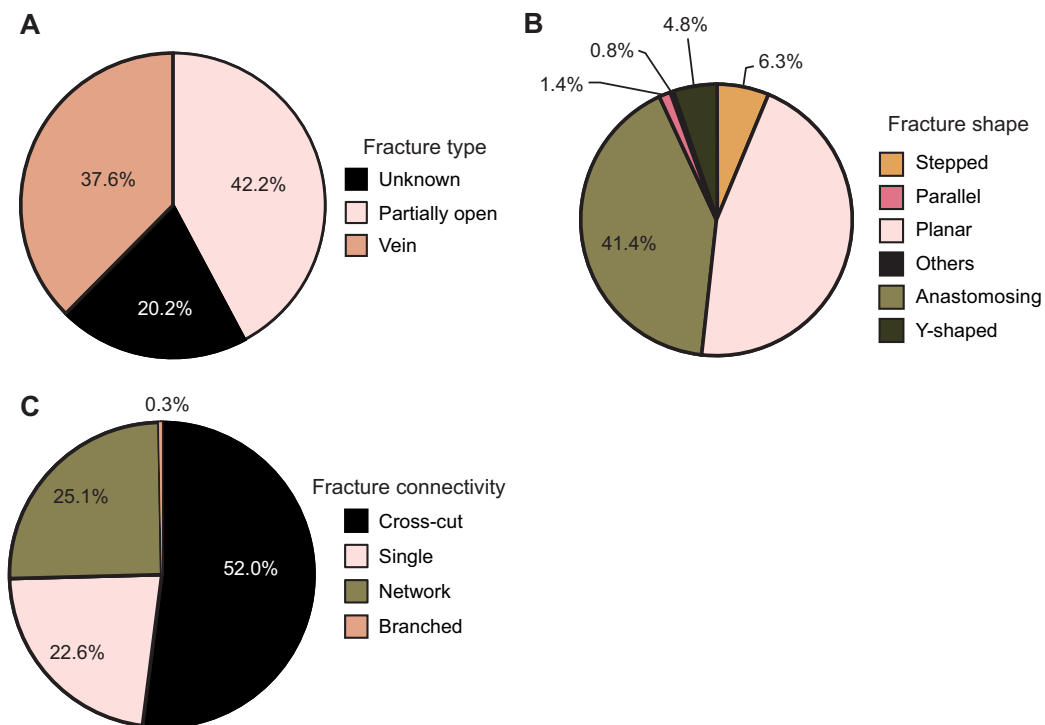
A

B

C

Figure F28. Basalt core fractures, Site U1562. A. Percentages of observed fracture types. B. Percentages of observed fracture shapes. C. Percentages of observed fracture connectivity.
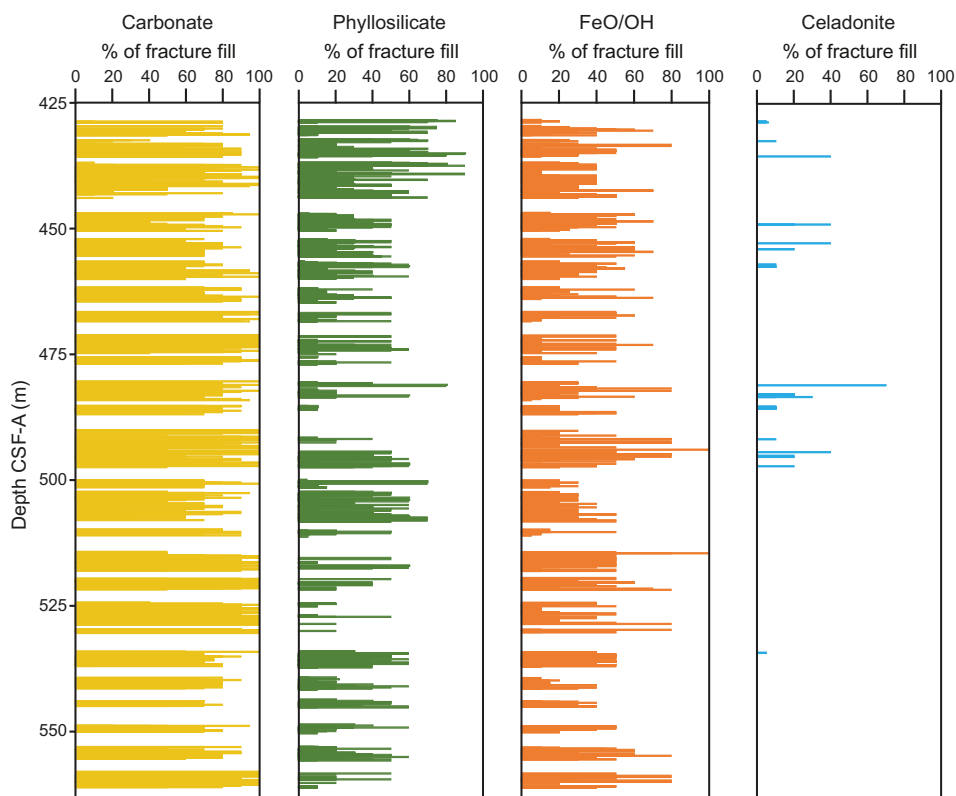
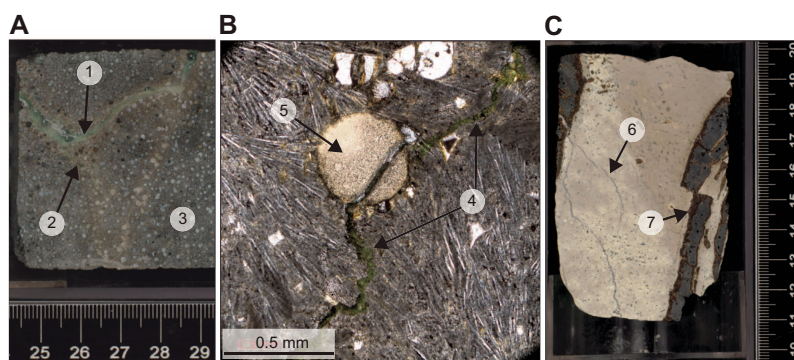**Figure F29.** Mineral fill percentages for individual fractures, Hole U1562B.

Figure F30. A. Altered highly vesicular basalt showing a chlorite/celadonite/calcite vein (1) displaying an oxide-rich halo (2) with abundant vesicles (3) (395C-U1562A-65X-1, 24–29 cm). B. Green celadonite vein (4) cutting through basalt and a saponite-filled vesicle (5) (395C-U1562B-5R-3, 68–71 cm). C. Carbonate-filled fractures cutting through altered carbonate sediments (6) and palagonitized basalt glass (7) (15R-2, 10–20 cm).

6. Micropaleontology

At Site U1562, a 429.8 m long interval of upper Miocene to upper Pleistocene silty clay and nannofossil chalk was recovered across multiple holes. Micropaleontological analyses were undertaken on samples from Hole 395C-U1562A, which recovered sediments in cores from 0 to 429.8 m CSF-A, and Hole 395-U1562C, which recovered core from 0 to 300.73 m CSF-A. The APC and XCB systems were used in both holes. In Hole U1562A, basement was encountered at ~430 m CSF-A in Section 64X-CC. Below this depth, Core 65X contains 0.68 m of basalt, confirming the transition from sediment to basement. Samples from the uppermost 300.73 m were analyzed for micropaleontology from Holes U1562A and U1562C, and below this depth only samples from Hole U1562A were available for study. Biohorizons used in the age model are based on calcareous nannoplankton, planktonic foraminifers, and bolboforms. Calcareous nannofossils and planktonic foraminifers are present with varying abundances, from barren or nearly barren samples to those with very high abundances. This change in abundance most likely reflects glacial–interglacial variability in temperatures, salinity, and/or ice cover in the Quaternary part of the succession. Bolboforms, when present, are generally rare or few.

6.1. Calcareous nannofossils

A total of 47 core catcher samples from Hole U1562A and 96 core catcher and working-half section samples from Hole U1562C were studied for calcareous nannofossils. One additional sample from Hole 395C-U1562B was taken from the mudstone found ~45 m below the top of the igneous succession. Observations were undertaken using plane-polarized light, cross-polarized light, and circular-polarized light. A list of calcareous nannofossil bioevents is provided in Table **T6**; these bioevents are mostly based on Hole U1562C where it overlaps in depth with Hole U1562A because the former was studied in more detail shipboard during Expedition 395. One biohorizon is included from Hole U1562A, top *Coccolithus miopelagicus*, because Hole U1562C was not drilled to this depth. Calcareous nannofossils are present in most samples although with distinctly differing abundances alternating in intervals downcore, from few (1–5 per field of view [FOV]) to dominant (hundreds per FOV). In a distinct interval between Samples 395-U1562C-7H-CC (54.2 m CSF-A) and 15H-CC (129.79 m CSF-A), more than half of the samples have very few to rare nannofossils or are barren of nannofossils. Preservation is mostly good in the uppermost ~130 m with occasional intervals of moderate preservation. An interval of very good preservation occurs between ~130 and ~250 m CSF-A, below which preservation is mostly good.

Samples from the Pleistocene succession recovered in Hole U1562C show distinct changes in the abundance of nannofossils and their species composition downcore. The base common *Emiliania huxleyi* biohorizon (0.09 Ma) is present in the first core between Samples 1H-1, 40 cm (0.4 m CSF-A), and 1H-2, 82 cm (2.31 m CSF-A). The biohorizon base *E. huxleyi* (0.29 Ma) is then placed

between Samples 1H-3, 140 cm (4.39 m CSF-A), and 1H-CC (5.32 m CSF-A), followed by top acme *Gephyrocapsa caribbeanica* (0.28 Ma) between Samples 1H-CC (5.32 m CSF-A) and 2H-2, 100 cm (7.82 m CSF-A), and top *Pseudoemiliania lacunosa* (0.43 Ma) between Samples 2H-2, 100 cm (7.82 m CSF-A), and 2H-3, 142 cm (9.74 m CSF-A). Two biohorizons, base acme *G. caribbeanica* (0.56) and top *Reticulofenestra asanoi* (0.91 Ma) are both placed between Samples 3H-1, 59 cm (15.39 m CSF-A), and 3H-3, 130 cm (19.12 m CSF-A), and will need further sampling in the cores to be resolved. An interval with very few nannofossils that also contains two biohorizons, top *Helicosphaera sellii* (1.24 Ma) and top *Calcidiscus macintyrei* (1.60 Ma), occurs between Samples 3H-3, 130 cm (19.12 m CSF-A), and 4H-4, 86 cm (29.69 m CSF-A). No other Pleistocene or late Pliocene biohorizons were identified because of the very rare and sporadic occurrence of *Discoaster* species. The next, middle Pliocene biohorizon is top *Reticulofenestra pseudoumbilicus* (3.82 Ma) between Samples 17F-CC (144.17 m CSF-A) and 18F-CC (148.45 m CSF-A). Two calcareous nannofossil biohorizons, the top paracme of *R. pseudoumbilicus* (7.1 Ma) between Samples 39F-CC (237.52 m CSF-A) and 40F-CC (242.22 m CSF-A) and top *C. miopelagicus* (11.04 Ma) between Samples 395C-U1562A-59X-CC (378.93 m CSF-A) and 60X-CC (383.06 m CSF-A), were identified in the upper Miocene. The presence of *C. miopelagicus* constrains the bottom of the hole to be older than 11.04 Ma (see also **Age model**). Sample 395C-U1562B-14R-2, 12–17 cm, taken from the 65 cm thick mudstone below the top of the igneous succession, is dominated by a moderately preserved calcareous nannofossil assemblage consisting of *R. pseudoumbilicus*, medium sized *Reticulofenestra* species and *Reticulofenestra perplexa*, *Sphenolithus* sp., and *Calcidiscus* sp. The assemblage looks significantly different from the one found at the base of Hole U1562A (Sample 46X-CC; 427.4 m CSF-A). *C. miopelagicus* is present and gives an age estimate that is older than 11.04 Ma (top *C. miopelagicus* in Raffi et al., 2020).

6.2. Planktonic foraminifers

Samples at Site U1562 were studied in Holes U1562A–U1562C. Samples from Holes U1562A and U1562B were processed and studied in the micropaleontology laboratory at University College London, and those from Hole U1562C were processed and studied on board *JOIDES Resolution*. A total of 31 core catcher samples were studied from Hole U1562A in the depth interval 0–476 m CSF-A, spanning almost the entire sedimentary succession, including one sample from the mudline. A single sample was studied from Hole U1562B from a 65 cm thick layer of sediment located ~45 m below the top of the igneous basement succession at ~476 m CSF-A. A total of 47 core catcher samples were studied for planktonic foraminifers from Hole U1562C, spanning 0–301 m CSF-A. A list of planktonic foraminifer bioevents is provided in Table **T7**. Preservation is excellent or very good in most samples except for some samples from the deeper part of the succession, which are indurated and the tests are infilled but in which preservation is still rated as good. Plank-

Table T6. Calcareous nannofossil bioevents, Site U1562. B = base, Bc = base common, Ba = base acme, T = top, Ta = top acme, Tpa = top paracme. **Download table in CSV format.**

Biohorizon	Marker species	Age (Ma)	(Sub)zone base	Top core, section, interval (cm)	Bottom core, section, interval (cm)	Top depth CSF-A (m)	Bottom depth CSF-A (m)	Midpoint depth CSF-A (m)	±
				395-U1562C-	395-U1562C-				
1	Bc *Emiliania huxleyi*	0.09		1H-1, 40	1H-2, 82	0.40	2.31	1.36	0.96
2	Ta *Gephyrocapsa caribbeanica*	0.28		1H-CC	2H-2, 100	5.32	7.82	6.57	1.25
3	B *Emiliania huxleyi*	0.29	NN21	1H-3, 140	1H-CC	4.39	5.32	4.86	0.46
4	T *Pseudoemiliania lacunosa*	0.43	NN20	2H-2, 100	2H-3, 142	7.82	9.74	8.78	0.96
5	Ba *Gephyrocapsa caribbeanica*	0.56		3H-1, 59	3H-3, 130	15.39	19.12	17.26	1.86
6	T *Reticulofenestra asanoi*	0.91		3H-1, 59	3H-3, 130	15.39	19.12	17.26	1.86
9	T *Helicosphaera sellii* (Atlantic)	1.24		3H-3, 130	4H-4, 86	19.12	29.69	24.41	5.29
12	T *Calcidiscus macintyrei*	1.60		3H-3, 130	4H-4, 86	19.12	29.69	24.41	5.29
	Base Pleistocene	2.59							
	Base upper Pliocene	3.60							
19	T *Reticulofenestra pseudoumbilicus*	3.82	NN16	17F-CC	18F-CC	144.17	148.45	146.31	2.14
	Base Pliocene	5.33							
22	Tpa *Reticulofenestra pseudoumbilicus*	7.10		39F-CC	40F-CC	237.52	242.22	239.87	2.35
				395C-U1562A-	395C-U1562A-				
28	T *Coccolithus miopelagicus*	11.04		59X-CC	60X-CC	378.93	383.06	380.995	2.06

tonic foraminifers are common to dominant in all samples except for the interval between Samples 395-U1562C-10H-CC (82.70 m CSF-A) and 14H-CC (120.71 m CSF-A) and correlative levels in Hole U1562A, which are discussed further below.

Sample 395C-U1562A-1H-1, 0 cm, from the mudline, contains many iron-stained shells, which may indicate a component of reworked or disturbed material, as well as a similar proportion of fresh-looking specimens. The assemblage is diverse and indicative of interglacial conditions. Large *Globigerina bulloides* is abundant and shows apparent intergradation with *Globigerina cariacoensis* and *Globigerina umbilicata*. Both *Neogloboquadrina incompta* (dextral) and *Neogloboquadrina pachyderma* (sinistral) are present. The most interesting aspect of this sample is the presence of rare specimens of *Globorotalia tumida*, a species that was not found deeper in the sediment or in the mudline samples collected at other Expedition 395 sites. This species peaks in abundance at the equator and also occurs commonly in warm boundary currents, but it is generally absent or extremely scarce in higher latitudes (Siccha and Kucera, 2017). Its presence may be a function of warm Holocene conditions. It is unlikely to be an Anthropocene invader because most individuals are iron stained, probably indicating prolonged exposure on the seafloor.

Sample 395C-U1562A-1H-CC (1.99 m CSF-A) contains frequent to abundant encrusted sinistral *N. pachyderma* and is therefore attributed to the *N. pachyderma* Zone. Also present are *G. bulloides*, *Turborotalita quinqueloba*, *G. cariacoensis*, *G. umbilicata*, *Globoconella inflata*, *Globorotalia scitula*, and *Globigerinita glutinata*. The base common encrusted sinistral *N. pachyderma*, marking the base of the *N. pachyderma* Zone at 1.82 Ma, is most closely constrained in Hole U1562C between Samples 395-U1562C-3H-CC (24.62 m CSF-A) and 4H-CC (34.32 m CSF-A). Samples 395C-U1562A-4H-CC (31.06 m CSF-A) and 5H-CC (40.41 m CSF-A) contain *G. inflata* in the absence of encrusted *N. pachyderma* (although rare sinistral unencrusted specimens are present in the latter sample) and are therefore assigned to the *G. inflata* Zone. The base of *G. inflata*, marking the base of the *G. inflata* Zone at 2.06 Ma, is between Samples 5H-CC (40.41 m CSF-A) and 6H-CC (49.71 m CSF-A). Sample 6H-CC (49.71 m CSF-A) lacks *G. inflata* and *G. umbilicata* and is therefore assigned to the *G. bulloides* Zone. The bottom of *G. inflata* was found at a dis-

Table T7. Planktonic foraminifer bioevents, Site U1562. B = base, Bc = Base common, T = top, X = coiling reversal, d-s = dextral to sinistral, sin = sinistral. IRD = ice-rafted debris. PRZ = partial range zone, LOZ = lowest occurrence zone, CRZ = concurrent range zone. **Download table in CSV format.**

Biohorizon	Marker species	Age (Ma)	(Sub)zone base	Top core, section, interval (cm)	Bottom core, section, interval (cm)	Top depth CSF-A (m)	Bottom depth CSF-A (m)	Midpoint depth CSF-A (m)	±
				395C-U1562A-	395C-U1562A-				
F1	Bc *Neogloboquadrina pachyderma* (sin)	1.82	*N. pachyderma* PRZ	1H-CC	4H-CC	1.99	31.11	16.55	14.56
F2	B *Globoconella inflata*	2.06	*G. inflata* LOZ	5H-CC	6H-CC	40.41	49.71	45.06	4.65
F3	B *Globigerina umbilicata*	2.07		5H-CC	6H-CC	40.41	49.71	45.06	4.65
F4	T *Neogloboquadrina atlantica*	2.26	*G. bulloides* PRZ	9H-CC	10H-CC	78.44	88.05	83.25	4.81
F5	B *Globigerina cariacoensis*	2.26		9H-CC	10H-CC	78.44	88.05	83.25	4.81
	Base common IRD			14H-CC	18H-CC	125.61	163.41	144.51	18.90
	Base Pleistocene	2.59							
	Base upper Pliocene	3.60							
F6	B *Globoconella puncticulata*	4.54	*G. puncticulata/N. atlantica* CRZ	18H-CC	19H-CC	163.41	173.47	168.44	5.03
F7	B *Globorotalia crassaformis*	4.60		18H-CC	19H-CC	163.41	173.47	168.44	5.03
	Base Pliocene	5.33							
F8	X d-s *Neogloboquadrina atlantica*	9.23		52F-CC	54F-CC	337.84	347.37	342.61	4.77
F9	B *Globorotalia cibaoensis*	9.44	*G. cibaoensis* LOZ	54F-CC	56F-CC	347.37	356.70	352.04	4.66
F10	T *Paragloborotalia mayeri*	10.54	*P. continuosa* PRZ	58X-CC	59X-CC	366.22	378.93	372.58	6.36
F11	B *Neogloboquadrina acostaensis*	10.57		62X-CC	63X-CC	404.47	413.27	408.87	4.40
	Base upper Miocene	11.65							
F12	B *Neogloboquadrina atlantica*	11.76			>64X-CC		>427.40		
				395C-U1562B-	395C-U1562B-				
F15	B *Orbulina suturalis*	15.12			>14R-2, 12-17		>475.66		
				395-U1562C-	395-U1562C-				
F1	Bc *Neogloboquadrina pachyderma* (sin)	1.82	*N. pachyderma* PRZ	3H-CC	4H-CC	24.62	34.32	29.47	4.85
F2	B *Globoconella inflata*	2.06	*G. inflata* LOZ	7H-CC	8H-CC	54.20	63.78	58.99	4.79
F3	B *Globigerina umbilicata*	2.07		6H-CC	7H-CC	44.81	54.25	49.53	4.72
F4	T *Neogloboquadrina atlantica*	2.26	*G. bulloides* PRZ	10H-CC	12H-CC	82.65	101.75	92.20	9.55
F5	B *Globigerina cariacoensis*	2.26		14H-CC	15H-CC	120.71	129.79	125.25	4.54
F6	B *Globoconella puncticulata*	4.54	*G. puncticulata/N. atlantica* CRZ	21F-CC	22F-CC	159.88	164.51	162.20	2.31

tinctly lower depth in Hole U1562C, between Samples 7H-CC (54.20 m CSF-A) and 8H-CC (63.78 m CSF-A), but this is considered less reliable because it is based on the presence of a single specimen.

Sample 395C-U1562A-9H-CC (78.44 m CSF-A) yielded a very small residue in the >63 µm fraction, possibly because this part of the sediment drift was subject to winnowing, and contains just two specimens of *Neogloboquadrina atlantica*. Because this species is usually common up to its top occurrence (Poore and Berggren, 1975), these specimens are interpreted as probably reworked and the top occurrence datum (2.26 Ma) is placed between Samples 9H-CC (78.44 m CSF-A) and 10H-CC (88.05 m CSF-A). An even more complex picture occurs around the same depth in Hole U1562C, in which a series of samples spanning from Sample 10H-CC (82.65 m CSF-A) through 14H-CC inclusive (120.71 m CSF-A) have only few or rare planktonic foraminifers or are barren. In the same interval, quartz and rock fragments interpreted as ice-rafted debris (IRD) vary from dominant (Sample 11H-CC; 92.35 m CSF-A) to absent (Sample 12H-CC; 101.75 m CSF-A). Observations of the sediment in this interval (see **Lithostratigraphy**) reveal that IRD presence varies greatly on a decimeter scale, such that the paleontological core catcher samples must inevitably alias a complex stratigraphic pattern. In Hole U1562C, the top of *N. atlantica* is placed between Samples 10H-CC (82.65 m CSF-A) and 12H-CC (101.75 m CSF-A), and the intervening sample (11H-CC; 92.35 m CSF-A) is barren and dominated by IRD.

The bottom extent of frequent to dominant quartz and rock fragments is constrained in Hole U1562C to between Samples 14H-CC (120.71 m CSF-A) and 15H-CC (129.79 m CSF-A). In Hole U1562A, the lowest abundant quartz is in Sample 14H-CC (125.61 m CSF-A). These observations constrain the lowest recorded evidence for significant ice rafting in our samples.

The washed residue >63 µm of Sample 395-U1562C-15H-CC (129.79 m CSF-A) contains large numbers of foraminifer tests, many of which are infilled with a speckled light greenish gray to glossy black material and coated with a thin reddish orange rind with a waxy appearance (Figure **F31**). The greenish gray to glossy black material also occurs as free rounded pellets and subangular clasts. Preliminary shipboard investigation with scanning electron microscope–energy dispersive spectrometry (SEM-EDS) and XRD indicates that it is likely glauconite, and the reddish orange coatings appear to be an iron- and titanium-rich amorphous silica. This mineralization is interpreted as authigenic, suggesting that the foraminifers may have been exposed on the seafloor for extended periods before being mixed with fresh unaltered specimens and concentrated by seafloor currents. Glauconite and glauconite-infilled foraminifers occur sporadically through the rest of the succession below this level.

The base of the *Globoconella puncticulata*/*N. atlantica* Zone is marked by the base of *G. puncticulata* (4.54 Ma) between Samples 395C-U1562A-18H-CC (163.41 m CSF-A) and 19H-CC (173.47 m CSF-A) and at a similar depth in Hole U1562C between Samples 21F-CC (159.88 m CSF-A) and 22F-CC (164.51 m CSF-A). This event corresponds to the immigration and rapid dispersal of *G. puncticulata* across much of the Atlantic Ocean and Mediterranean Sea that is well constrained at 4.54 Ma in other sections (for discussion, see **Micropaleontology** in the Expedition 395 methods chapter [Parnell-Turner et al., 2025a]).
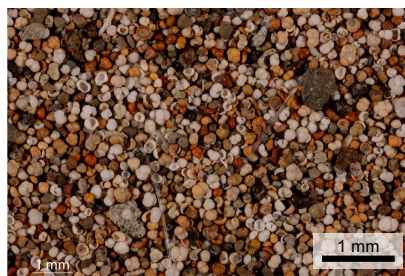

Figure F31. Foraminifer residue >63 µm (395-U1562C-15H-CC; 129.79 m CSF-A). Shown is a mixture of relatively fresh looking foraminifers (white) and glauconite-infilled shells (greenish gray to black) with iron-/titanium-rich silica coatings (orange). Free glauconite pellets and sponge spicules also occur.

The interval from base *G. puncticulata* to Sample 395C-U1562A-52F-CC (337.84 m CSF-A) is relatively homogeneous in terms of planktonic foraminifer assemblages, with *N. atlantica* (sinistral), *G. bulloides*, and *Globigerina falconensis* generally common or abundant and *G. scitula* occurring sporadically. Scattered occurrences of specimens attributed to *Globorotalia cibaoensis* indicate an assignment to the *G. cibaoensis* Zone. *Orbulina universa* is consistently present, albeit in low numbers, which contrasts with its patchier occurrences at higher stratigraphic levels at the site.

A pronounced shift in the coiling direction of *N. atlantica* from dextral to sinistral dominance (going upcore) occurs between Samples 395C-U1562A-52F-CC (337.84 m CSF-A) and 54F-CC (347.37 m CSF-A) (Figure **F32**; Table **T8**). Although the species is very rare in the latter sample with just two specimens observed, both are dextral. The same sample is noteworthy in containing many large *O. universa*, which is much more common than it is anywhere else in the succession. The coiling shift is calibrated at 9.23 Ma based on the record of Aksu and Kaminski (1989) at Ocean Drilling Program (ODP) Site 646 in the Labrador Sea (see **Micropaleontology** in the Expedition 395 methods chapter [Parnell-Turner et al., 2025a]). *N. atlantica* is common or abundant in Samples 56F-CC (356.70 m CSF-A) through 64X-CC (427.40 m CSF-A), although it is dominated by the "primitive" morphotype that some authors prefer to recognize as *N. atlantica praeatlantica* (Foresi et al., 2002). Base *G. cibaoensis*, which marks the base of the *G. cibaoensis* Zone (9.44 Ma), is just below the coiling shift in *N. atlantica* and is located between Samples 54F-CC (347.37 m CSF-A) and 56F-CC (356.70 m CSF-A), but its relative rarity and the patchiness of its distribution gives the biohorizon low confidence.

The top of *Paragloborotalia mayeri* (10.54 Ma), marking the base of the *Paragloborotalia continuosa* Zone, occurs between Samples 395C-U1562A-58X-CC (366.22 m CSF-A) and 59X-CC (378.93 m CSF-A). The species is rare below its disappearance level despite being common to abundant lower in the succession in Samples 63X-CC (413.27 m CSF-A) and 64X (427.40 m CSF-A). This pattern contrasts with ODP Site 926 in the tropical Atlantic, where the biohorizon is calibrated astronomically at 10.54 Ma and the species is abundant up to its extinction level (Chaisson and Pearson, 1997). There are complex taxonomic and biochronologic questions surrounding this
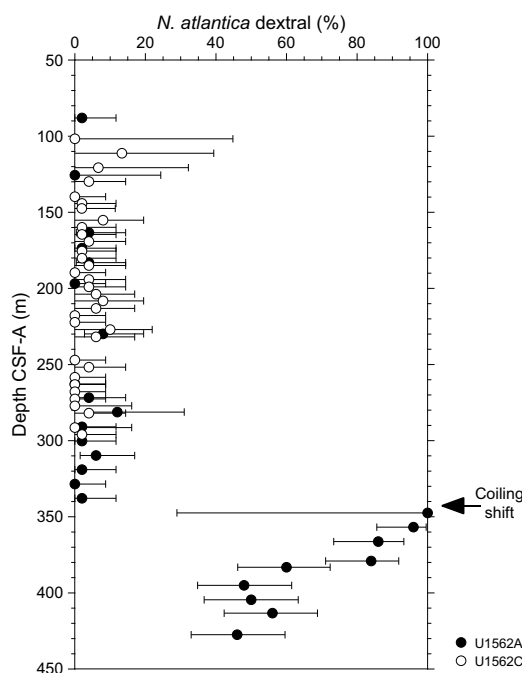

Figure F32. *N. atlantica* coiling ratios, Site U1562. Error bars = 95% confidence intervals. The dextral to sinistral shift (calibrated at 9.23 Ma) is marked.

Table T8. *N. atlantica* coiling direction count data, Site U1562. **Download table in CSV format.**

potentially useful datum (see discussion in Raffi et al., 2020). Specimens at Site U1562 closely resemble those illustrated as *P. mayeri* at Deep Sea Drilling Project (DSDP) Site 407 on the Reykjanes Ridge by Poore (1979), with distinctly curved sutures on the spiral side and highly arched apertures. Samples from Site U1562 were directly compared under the microscope with an assemblage from near the top occurrence at Site 926. Those from Site U1562 are on average smaller with fewer chambers and more strongly curved spiral sutures, but very similar specimens occur among the range of variation at Site 926. It is likely that the top occurrence on the Reykjanes Ridge records the same biological extinction as occurs in the tropics.

An upsection change from random to dextrally dominant coiling in *N. atlantica* occurs between Samples 395C-U1562A-59X-CC (378.93 m CSF-A) and 60X-CC (383.06 m CSF-A) (Figure **F32**). This change may be useful for regional correlation. The lowermost sample examined in the regular sedimentary succession, Sample 64X-CC (427.4 m CSF-A), contains *P. mayeri* and is assigned to the *P. mayeri* highest occurrence zone. It also contains *N. atlantica*.

Hole U1562B was cored with the RCB system from the lowermost part of the sedimentary succession into basement. After penetrating over 45 m into basalt, a substantial interval of sediment was encountered, comprising the whole of Section 14R-2. Sample 14R-2, 12–17 cm (475.66 m CSF-A), contains a well-preserved foraminifer assemblage that is significantly older than the lowermost sample examined from the sedimentary succession described above. Of particular note is the frequent presence of a globorotaliid species of uncertain affinity. The species bears a general resemblance to *Fohsella fohsi*, a tropical form from the same time interval, except that it is heavily encrusted and invariably has five chambers per whorl rather than the six typical of *F. fohsi*. Also present in the sample is rare *Trilobatus trilobus* (the only observed occurrence in Expedition 395 samples of this common low- to mid-latitude species) and questionable *Praeorbulina circularis*. Another peculiarity of the assemblage compared with all overlying samples is the absence of *Paragloborotalia* species. These indications suggest that the sediment pocket is distinctly older than the lowermost part of the regular sedimentary succession at the site, but it is difficult to specify how much older (see **Age model**).

6.3. Bolboforms

Bolboforms were studied in the same set of sample residues used for foraminifers. In Hole U1562C, bolboforms occur from Sample 27F-CC (184.88 m CSF-A) downward. In Hole U1562A, they occur in every sample studied from Sample 22F-CC (196.87 m CSF-A) downward. They are generally very rare in comparison to foraminifers and other particles but become markedly more abundant downcore. Being small, they are difficult to identify with the light microscope, so all specimens were transferred to SEM stubs and imaged using the shipboard Hitachi TM3000 desktop SEM before taxonomic assignment. A list of biohorizons is presented in Table **T9**.

Top *Bolboforma intermedia*, marking the base of the *Bolboforma costairregularis* Zone, could not be identified because of very scarce occurrences. The base of *B. intermedia*, marking the base of the *B. intermedia* Zone (8.18 Ma), is located tentatively between Samples 395C-U1562A-48F-CC and 50F-CC (318.91–328.49 m CSF-A). *Bolboforma metzmacheri* is also rare in the succession, with its base marking the base of the *B. metzmacheri* Zone (9.89 Ma), tentatively placed between Samples 56F-CC (356.70 m CSF-A) and 58X-CC (366.22 m CSF-A). The top of *Bolboforma sub-*

Table T9. Bolboform bioevents, Site U1562. B = bottom, T = top. LOZ = lowest occurrence zone, PRZ = partial range zone, TRZ = total range zone. **Download table in CSV format.**

Biohorizon	Marker species	Age (Ma)	(Sub)zone base	Top core, section, interval (cm)	Bottom core, section, interval (cm)	Top depth CSF-A (m)	Bottom depth CSF-A (m)	Midpoint depth CSF-A (m)	±
				395C-U1562A-	395C-U1562A-				
	Base Pliocene	5.33							
B3	B *Bolboforma intermedia*	8.18	*B. intermedia* TRZ	48F-CC	50F-CC	318.91	328.49	323.70	4.79
B4	B *Bolboforma metzmacheri*	9.89	*B. metzmacheri* LOZ	56F-CC	58X-CC	356.70	366.22	361.46	4.76
B5	T *Bolboforma subfragoris*	10.82	*B. capsula* PRZ	59X-CC	60X-CC	378.93	383.06	381.00	2.06
	Base upper Miocene	11.65							

fragoris, which marks the base of the *Bolboforma capsula* Zone (10.82 Ma), is more confidently placed between Samples 59X-CC (378.93 m CSF-A) and 60X-CC (383.06 m CSF-A). Several bicamerate specimens of *B. subfragoris* were observed in Sample 61X-CC (395.04 m CSF-A).

The lowermost sample examined is Sample 395C-U1562B-14R-2, 12–17 cm, which was taken from the short section of sediment that occurs more than 45 m below the top of igneous basement (see **Planktonic foraminifers**). The bolboform assemblage in this sample is distinctly different from those taken from the regular succession above and contains *Bolboforma laevis* together with several specimens of *Bolboforma clodiusi* and the *Bolboforma reticulata* s.l. group. The latter species, which is the most abundant species in the sample, resembles the form illustrated as "*Bolboforma oblongireticulata*" by Spiegler (1999), which appears to be a nomen nudum because it was never formally described. If that identification is correct, the assemblage is most likely from the middle Miocene *Bolboforma compressispinosa* Zone of Spiegler (1999), although the nominate species of the zone was not found in the sample. If so, this observation would agree with the planktonic foraminifer and nannofossil evidence from the sediment pocket and could indicate a tentative age of ~12.33–12.43 Ma according to our recalibration of the short biostratigraphic range of "*Bolboforma oblongireticulata*" at ODP Site 982 reported in Spiegler (1999).

7. Physical properties

A range of whole-round, section-half, and discrete sample physical properties were measured on ~730 m of sediment core recovered from Holes 395C-U1562A, 395C-U1562B, and 395-U1562C and ~77 m of basement core recovered from Holes U1562A and U1562B (Table **T10**). Physical properties data were cleaned for half the response function corresponding to the instruments at the top and bottom of each section, and values deemed artifacts were removed from the respective figures (Table **T11**). All raw data are retained in the Laboratory Information Management System (LIMS) database.

Table T10. Physical properties measurement resolution, Site U1562. MSP = point MS, RSC = reflectance spectroscopy and colorimetry, PWL = *P*-wave logger, PWB = *P*-wave bayonet, TCON = thermal conductivity. * = some variability in the measurement resolution that is dependent on the core recovery and changes in lithology, NA = not applicable. **Download table in CSV format.**

Hole	Lithology	GRA (cm)	MAD (m)	MS (cm)	MSP (cm)	NGR (cm)	RGB (cm)	RSC (cm)	PWL (cm)	PWC (m)	PWB (m)	TCON (m)
395C-												
U1562A	Sediment	2.5	~10	2.5	2.5	10	1	2.5	2.5	NA	NA	~10
U1562A	Basalt	2.5	NA	2.5	2.5	10	1	2.5	NA	1 sample	NA	1 sample
U1562B	Sediment	2.5	NA	2.5	2.0	10	1	2.0	2.5	~1 per core	NA	NA
U1562B	Basalt	2.5	NA	2.5	2.0	10	1	2.0	2.5	~1 per core	NA	~10*
395-												
U1562C	Sediment	2.5	NA	2.5	2.5	10	1	2.5	2.5	~1 per core	NA	~5–10

Table T11. Physical properties data cleaning, Site U1562. Indicated values are considered unrealistic and were removed from the presented figures. MSP = point MS, NA = not applicable. **Download table in CSV format.**

Parameter (unit)	Edge effect removal (cm)	Expedition 395C		Expedition 395
		Hole U1562A	Hole U1562B	Hole U1562C
MS (WRMSL, IU)	10	>750	>1200	>750
MSP (SHMSL, IU)	10	>750	>1200	>750
GRA (WRMSL, g/cm³)	10	<1.25, >2	<1 (0–430 m CSF-A), <2 (430 m CSF-A to bottom of hole)	<1.25, >1.8
P-wave logger (m/s)	10	<1450, >1700	>2000	<1450, >1900
RGB	5	>160 (0–351 m CSF-A), >180 (351–425 m CSF-A), >200 (425 m CSF-A to bottom of hole)	NA	>150
Color spectrometry (L*)	5	>50 (0–240 and 270–340 m CSF-A)	NA	NA
Color spectrometry (a*)	5	<8	NA	>7
Color spectrometry (b*)	5	less than –5	NA	>60

7.1. Whole-round measurements

Variations in sedimentary physical properties in Hole U1562C are very similar to those measured in the overlapping stratigraphic interval of Hole U1562A (Figures **F33**, **F34**). The sediments in the uppermost 130 m gradually increase downhole in gamma ray attenuation (GRA) bulk density, MS, and NGR with superimposed meter-scale oscillations. These parameters drop sharply at 130 m CSF-A. Below 130 m CSF-A, bulk densities stay relatively constant with small variations around 1.6 g/cm³, and MS and NGR show a more variable pattern. Relatively large amplitude variations (hundreds of instrument units for MS and tens of counts per second for NGR) to ~350 m CSF-A, below which both parameters show lower values. Between 180 and 300 m CSF-A, the oscillations in MS and NGR are most prominent and occur on a scale of ~20 m. Whole-Round Multisensor Logger (WRMSL) *P*-wave velocity (V_p) values increase slightly downhole and average around 1500 m/s.

In Hole U1562B, voids and gaps between the core and liners in the basalt sections make the interpretation of physical properties profiles less straightforward (Figure **F35**). Nevertheless, intervals of higher MS seem to correspond to slightly lower values in bulk density and NGR. Measured values in the sedimentary interval (Cores 2R–4R) are comparable with the physical properties values for the deepest sediments in Hole U1562A.

7.2. Split core measurements

The point MS (MSP) data show relative variations similar to those in the WRMSL MS data, and the absolute values for the sediments are alike, with the MSP values for the basalts slightly higher and lower in their relative extrema, probably because the WRMSL data integrate the volume of the whole core section (Figures **F33**, **F34**, **F35**). The changes in color reflectance properties in the
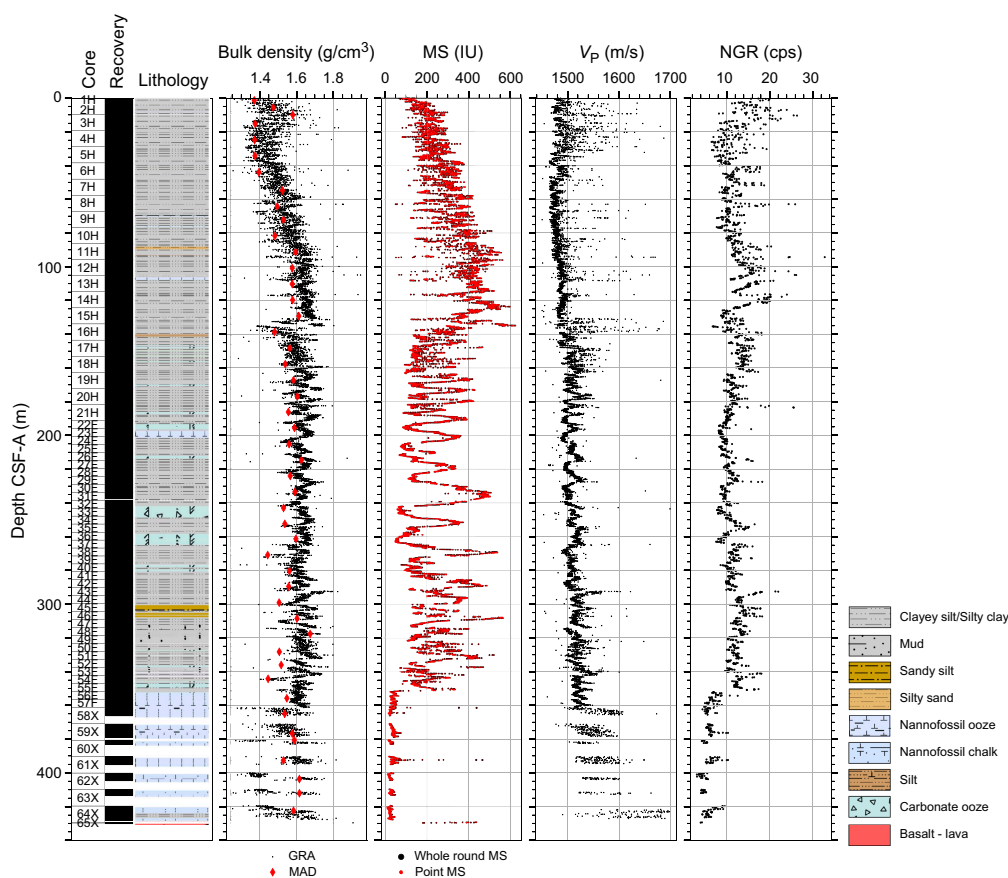
Figure F33. Physical properties measurements. Hole U1562A. cps = counts per second.
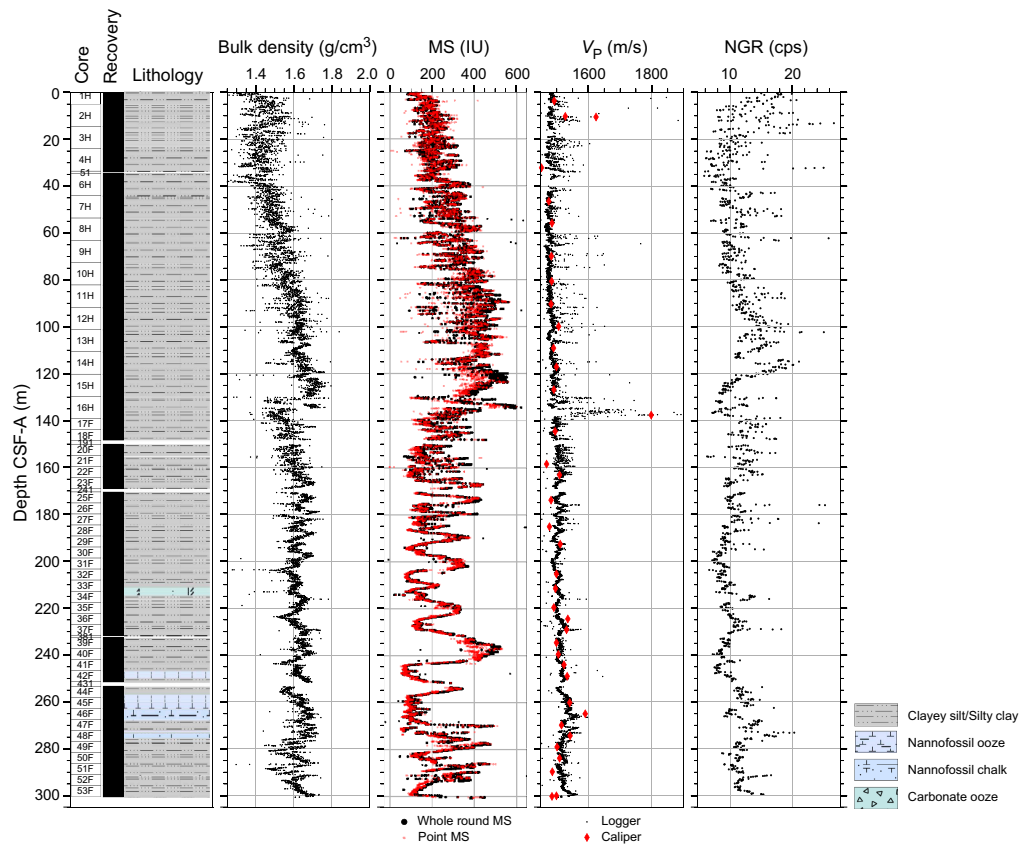
Figure F34. Physical properties measurements, Hole U1562C. cps = counts per second.
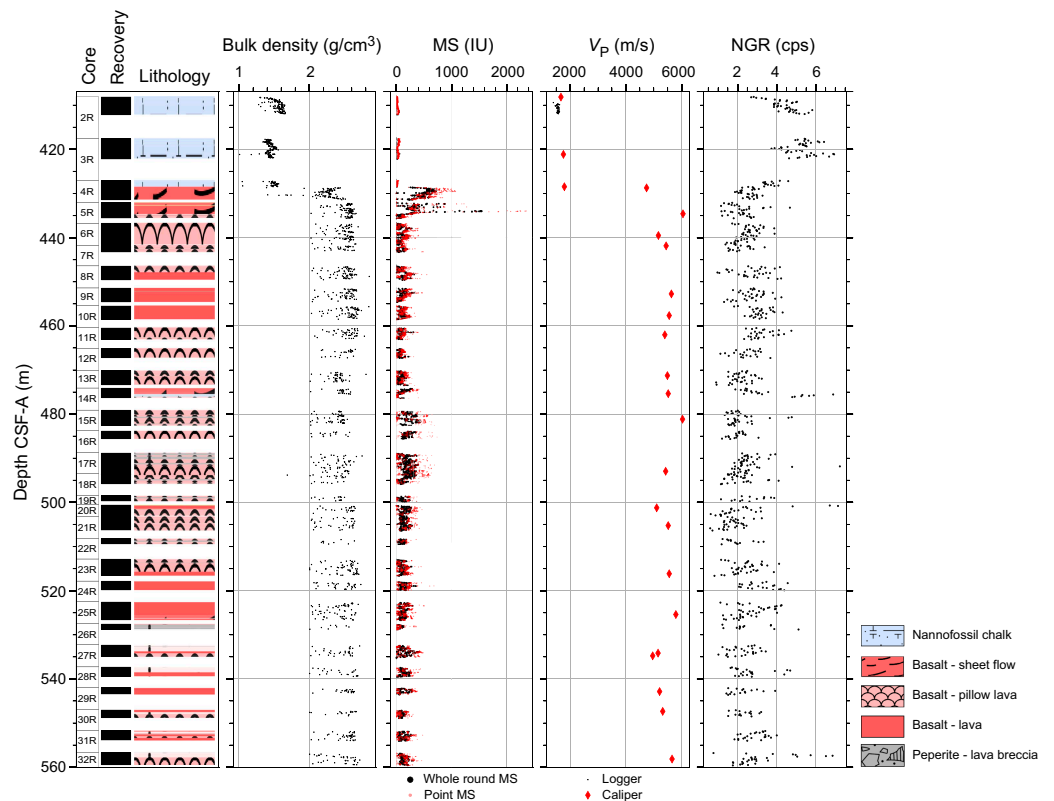

Figure F35. Physical properties measurements, Hole U1562B. cps = counts per second.

sediments of Holes U1562A and U1562C are divided into stratigraphic intervals similar to those in the WRMSL profiles (Figures **F36**, **F37**). Two brownish layers (9 and 7 m thick) with higher R, a*, and b* values occur toward the top of the holes (0–30 m CSF-A), below which depth color changes are dampened and the general color trends to darker to 130 m CSF-A. The interval between 130 and 350 m CSF-A has pronounced color cycles of varying thicknesses between lighter and darker intervals (submeter to multimeter scales). Just above the contact with basalt (350–430 m CSF-A), the sediments are noticeably lighter in color than the sediments above.

The presence of significant voids and uneven surfaces in the basalt sections of Hole U1562B leads to noisy color reflectance data (Figure **F38**). In the basement, the sedimentary and peperite units show up clearly in color records, with higher R, G, B, a*, and b* values (Figure **F15**). The L* reflectance record shows intervals of lower values, but a systematic relationship with basalt morphology is not observed.

7.3. Discrete measurements

7.3.1. *P*-wave velocity

V_P caliper (PWC) values (from measurements made in the *x*-direction, perpendicular to the core long axis) for sediments from Hole U1562B are about 1700 m/s, and for basalts they vary between
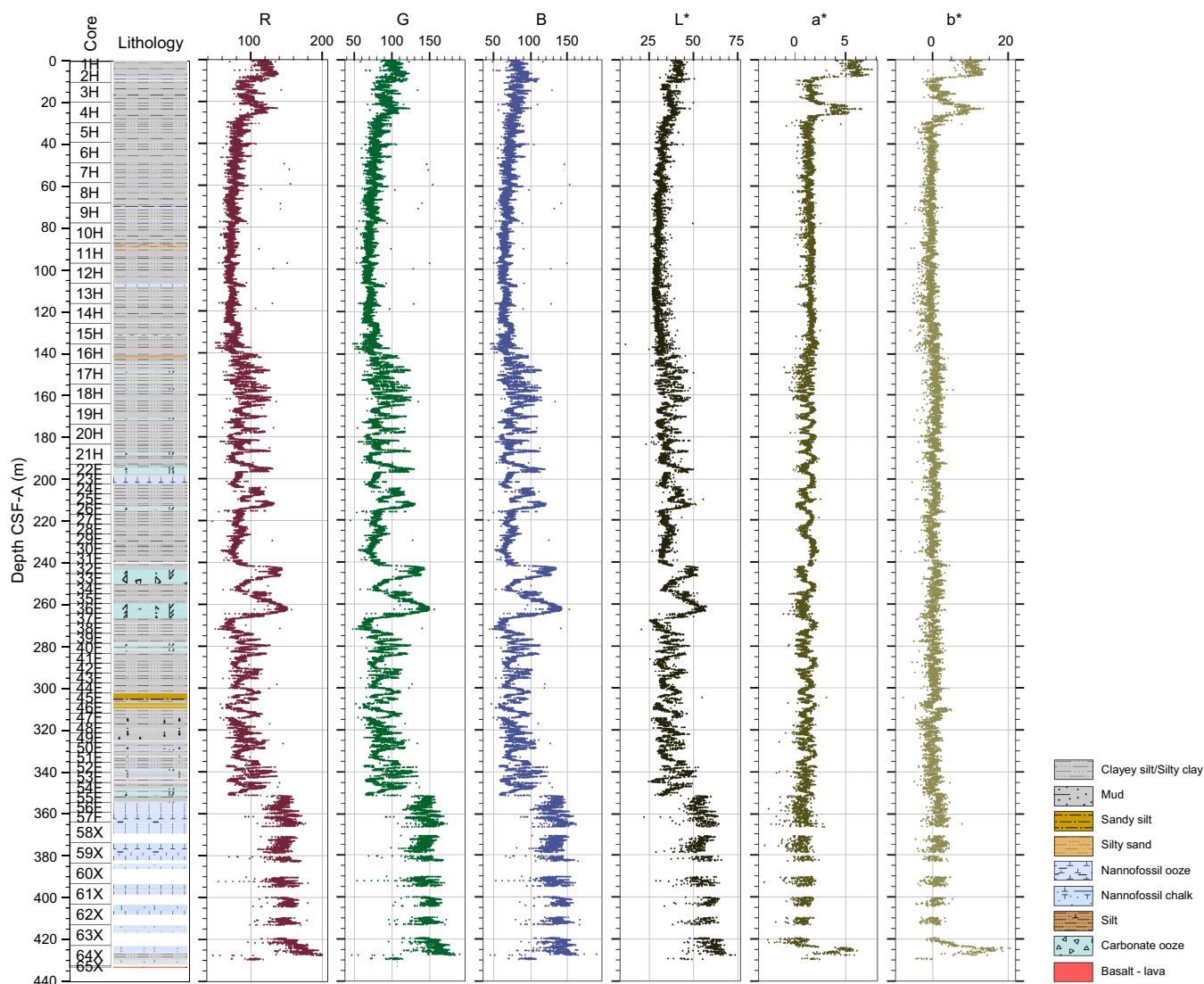
Figure F36. Archive-half colorimetry and reflectance measurements, Hole U1562A.

4725 and 6053 m/s (Figure **F35**). Sedimentary V_P values in Hole U1562C average around 1500 m/s (Figure **F34**). One point measured in Section 395-U1562C-16H-6, 53 cm (137.65 m CSF-A), shows a higher value of 1798 m/s, which is consistent with the higher velocity measurements measured using the WRMSL in this interval. This observation might indicate condensation at a lithologic transition that might also be a disconformity (see **Lithostratigraphy** and **Age model**).

7.3.2. Moisture and density

Moisture and density (MAD) samples were measured on sediment cores from Hole U1562A at approximately one per 10 m. Bulk density values are shown in Figure **F33** alongside the WRMSL bulk density estimates. MAD estimates of bulk density values in Hole U1562A range 1.4–1.7 g/cm³ and are in good agreement with GRA bulk density estimates from the WRMSL. Porosity ranges 63–81 vol% with an average of 70 vol% and a slightly decreasing trend downhole from around 80 to 65 vol%. Grain density varies from 2.6 to 2.9 g/cm³ with an average of 2.7 g/cm³ and shows a decreasing trend from around 2.9 to 2.6 g/cm³.

7.3.3. Thermal conductivity

Thermal conductivity measurements were made on working-half sections at a variable resolution for the different holes (Table **T10**). Thermal conductivity is typically 0.75–1.20 W/(m·K) for the sediments from Holes U1562A and U1562C and 1.40–1.80 W/(m·K) for Hole U1562B. Values slightly increase with depth for the sedimentary units and are relatively constant for the basement
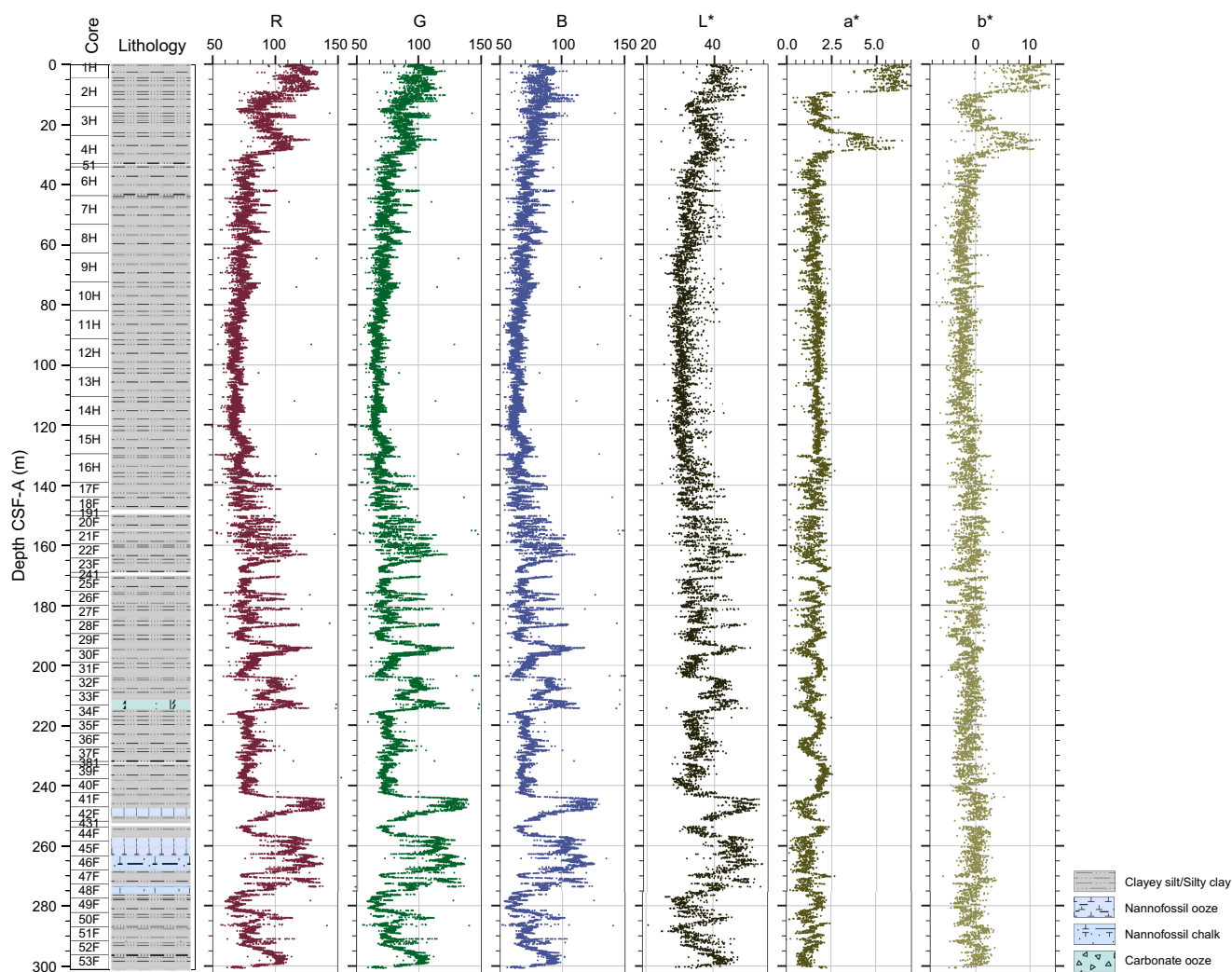

Figure F37. Archive-half colorimetry and reflectance measurements, Hole U1562C.
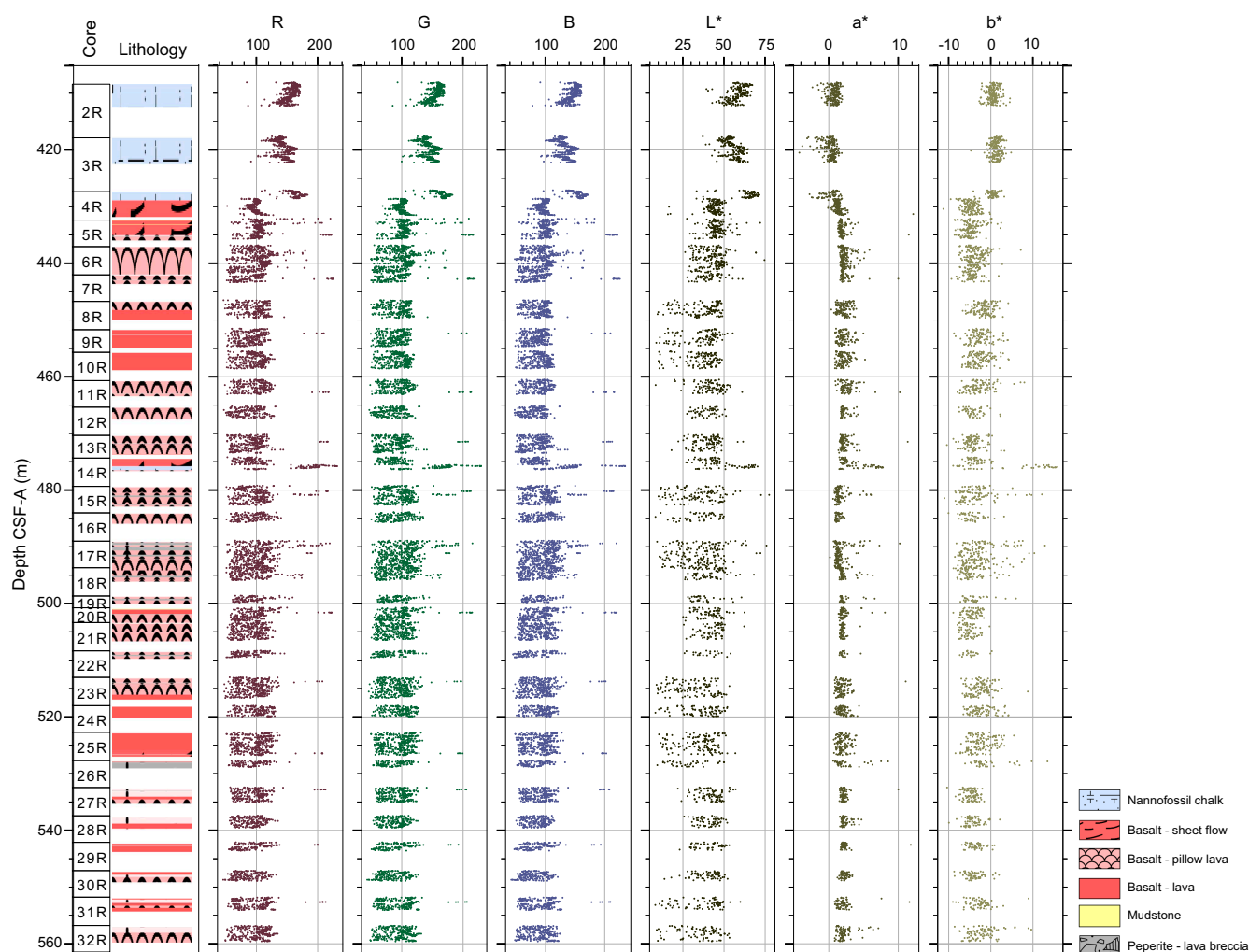
Figure F38. Archive-half colorimetry and reflectance measurements, Hole U1562B.

rocks. Thermal conductivity measurements of the sediments are combined with downhole formation temperature measurements to estimate heat flow (see **Downhole measurements**; Figure **F57**).

8. Stratigraphic correlation

The stratigraphic correlation reported here includes the main sedimentary targets of coring from Holes 395C-U1562A and 395-U1562C. Information from Hole U1562A was used to inform the position of the first core for Hole U1562C. MS data from whole-round measurements were used for near real-time correlation because they often reveal strong contrasts between lithologic sequences. These data were obtained shortly after the core is recovered on deck at 5.0 cm resolution using the Special Task Multisensor Logger (STMSL) to guide operational decisions. The whole-round MS data collected at 2.5 cm resolution using the WRMSL were used to construct the final splices. An overview of the MS data from Holes U1562A and U1562C and the wireline log data from Hole 395C-U1562B are presented in Figure **F39**.

8.1. Correlation between holes

Core 395-U1562C-1H recovered the mudline plus a length of 5.37 m, and this initial offset allowed filling gaps in recovery in Hole U1562A. Correlation was achieved without gaps through Cores 395C-U1562A-16H (144.63 m CSF-A; 155.125 m core composite depth below seafloor, Method A

[CCSF-A]) and 395-U1562C-17F (144.22 m CSF-A) (Figure **F40**). The lower extent of these cores was too close to alignment to be able to tie on to any of the next cores, leading to a correlation gap. Based on the pattern of MS variability and correlation with the downhole wireline logging MS data collected in Hole U1562B, the gap is estimated to be approximately 1 m. Similar small gaps can be
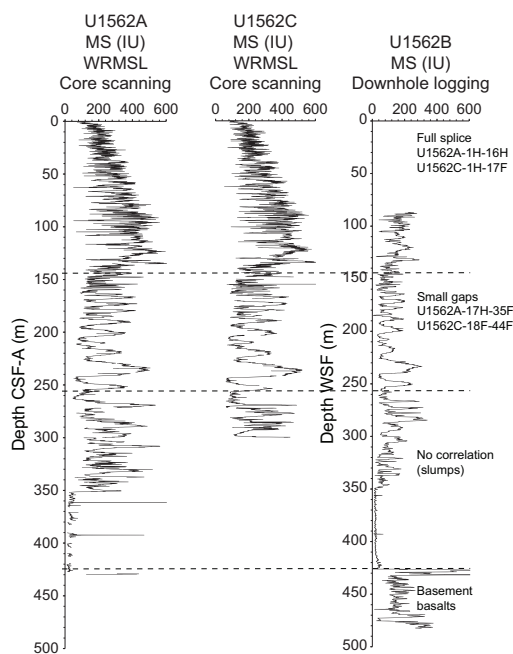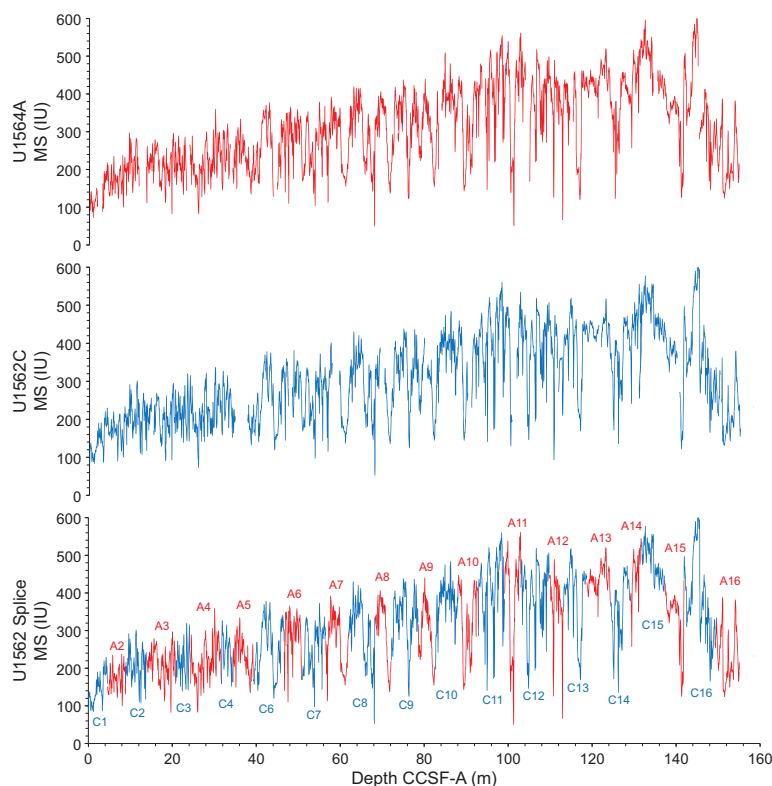

Figure F39. WRMSL and wireline logging MS, Site U1562.

Figure F40. Splice for 0–160 m CCSF-A, Site U1562. Cores included in the splice are noted, where C1 = Core 395-U1562C-1H.

found between Cores 395-U1562C-20F and 395C-U1562A-18H and between Cores 395-U1562C-22F and 395C-U1562A-19H (Figure **F41**). Despite the small gaps, this interval can still be tied with some confidence based on the broad cyclical patterns and the comparison with wireline logging MS data from Hole U1562B. In Cores 395-U1562C-19H through 35F and 395C-U1562A-25F through 35F, ties can be made to ~280 m CCSF-A (Figure **F42**). Below Core 395C-U1562A-35F, correlation between holes becomes difficult, probably because of the presence of disrupted sedimentary sequences (see **Lithostratigraphy**).

8.2. Construction of the splice

The continuous splice for the uppermost 155 m CCSF-A includes Holes U1562A and U1562C (Figure **F40**; Table **T12**). An appended splice is further extended to Core 395C-U1562A-35F by estimating the presence and magnitude of several small gaps (<1 m) (Figure **F42**). Core catcher sections were not included in the splice, and splice figures presented here do not include data collected in the core catcher sections.
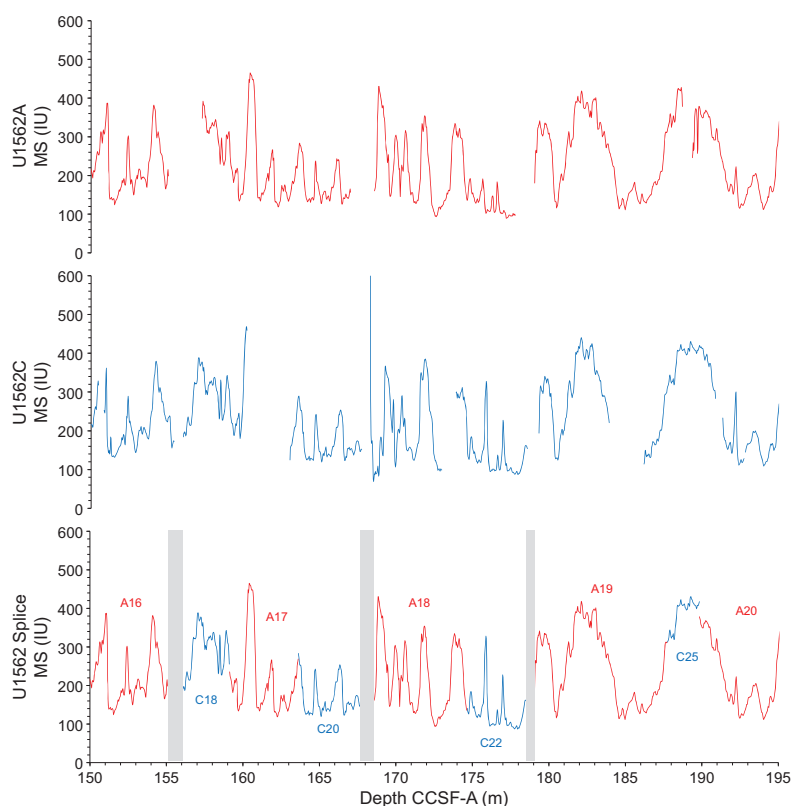

Figure F41. Splice for 155–195 m CCSF-A, Site U1562. Cores included in the splice are noted, where A16 = Core 395C-U1562A-16H. Several gaps (gray bars) prevent a full splice in this interval.
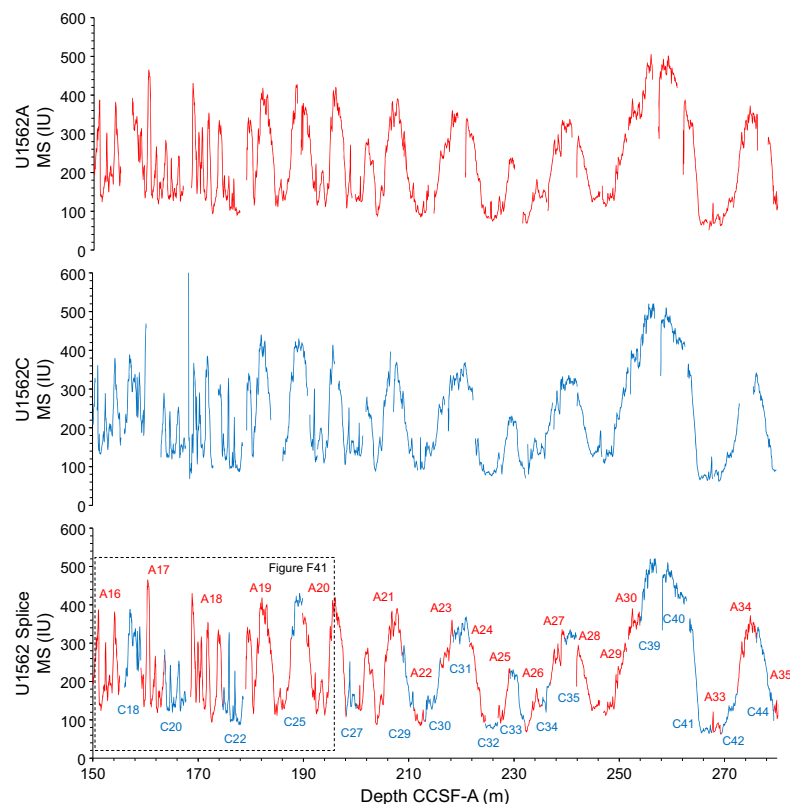
Figure F42. Splice for 150–280 m CCSF-A, Site U1562. Cores included in the splice are noted, where A16 = Core 395C-U1562A-16H.

Table T12. Splice table, Site U1562. **Download table in CSV format.**

9. Paleomagnetism

9.1. Shipboard measurements

Shipboard paleomagnetic investigations were conducted on archive-half sections from Holes 395C-U1562A, 395C-U1562B, and 395-U1562C (Figure **F43**; see **Paleomagnetism** in the Expedition 395 methods chapter [Parnell-Turner et al., 2025a]). For sediments from Hole U1562A, five demagnetization steps (0, 10, 15, 20, and 25 mT) at 2.5 cm spacing were performed, and for Hole U1562C four steps (0, 10, 15, and 20 mT) were adopted, using a resolution of 2.5 or 5 cm. For basalts from Hole U1562B, five steps of demagnetization (0, 10, 15, 20, and 25 mT) at 2 cm spacing were adopted.

We used the directional data from archive halves measured after in-line alternating field (AF) demagnetization step (maximum demagnetization step of 20 or 25 mT) to determine magnetic polarities in each hole. Directional data were analyzed using Zijderveld diagrams (Zijderveld, 1967), and the characteristic remanent magnetization (ChRM) direction(s) were calculated using principal component analysis (PCA) (Kirschvink, 1980) using PuffinPlot software (Version 1.4.1; Lurcock and Florindo, 2019).

9.2. Demagnetization behavior of sedimentary rocks

After the removal of an overprint up to 10 mT, stepwise AF demagnetization performed up to 20 or 25 mT successfully isolated a stable ChRM directed to the origin of the Zijderveld plot, even if not completely demagnetized (Figure **F44**). Normal (Figure **F44A, F44D**) and reversed (Figure

F44B, F44E) polarities were identified both in Holes U1562A and U1562C. In some cases, the natural remanent magnetization (NRM) was fully demagnetized within the 10 mT step (Figure F44C, F44F).

In Hole U1562A, NRM intensity varies from 4.8×10^{-5} to 4.3 A/m (average = 0.2 A/m). In Hole U1562C, NRM intensity ranges 4.9×10^{-3} to 2.21 A/m (average = 0.23 A/m) (Figure F45).

In Hole U1562A, point MS obtained from section halves (see **Physical properties**) ranges 2.7–664.2 IU (average = 228.3 IU) (Figure F45). Three measurement points in interval 58X-1, 22.5–27.5 cm, are greater than 1000 IU and correspond to three large (>2 cm) basaltic clasts (not shown). In Hole U1562C, MS varies from 0.4 to 755.7 IU (average = 248.1 IU) (Figure F46).

Both NRM and MS show considerable variability with depth (Figures F45, F46, F47), most likely due to changes in carbonate and silica content in sedimentary units. At 120–350 m CSF-A in Hole U1562A and 120–300 m CSF-A in Hole U1562C, both MS and NRM show a cyclicity that may reflect changes in carbonate content (see **Lithostratigraphy**). Below 350 m CSF-A in Hole U1562A, both NRM intensity and MS decrease considerably. Variations in inclination reflect changes in the magnetic polarities. Intervals of soft-sediment deformation (see **Lithostratigraphy**), which hamper magnetostratigraphic interpretation, are highlighted as yellow bands in Figures F45 and F46. Normal polarities (in black) are characterized by positive inclinations with short secular variations around values similar to the present-day field at Site U1562.
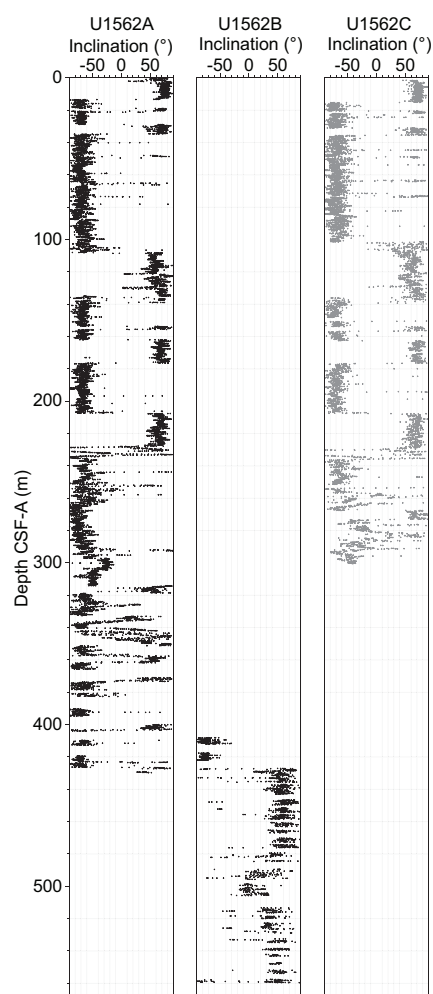

Figure F43. Inclination, Holes U1562A–U1562C. In-line measurements collected with SRM on archive halves at 25 mT (black) and 20 mT (gray) demagnetization steps.

9.3. Demagnetization behavior of basalts

The igneous rocks in Hole U1562B consist of pillow basalts and basalt flows (see **Igneous petrology**). Typical examples of demagnetization behavior are shown in Figure **F48**. After the removal of an initial overprint at 10–15 mT, usually a single component of magnetization can be isolated. AF demagnetization mainly shows two types of behavior with total magnetization loss before 20 mT (i.e., soft magnetization behavior; Figure **F48B**) or no significant loss of magnetization at 25 mT (i.e., hard magnetization behavior; Figure **F48A, F48C, F48D**). Most of the basalts show normal polarity (Figure **F48D**).
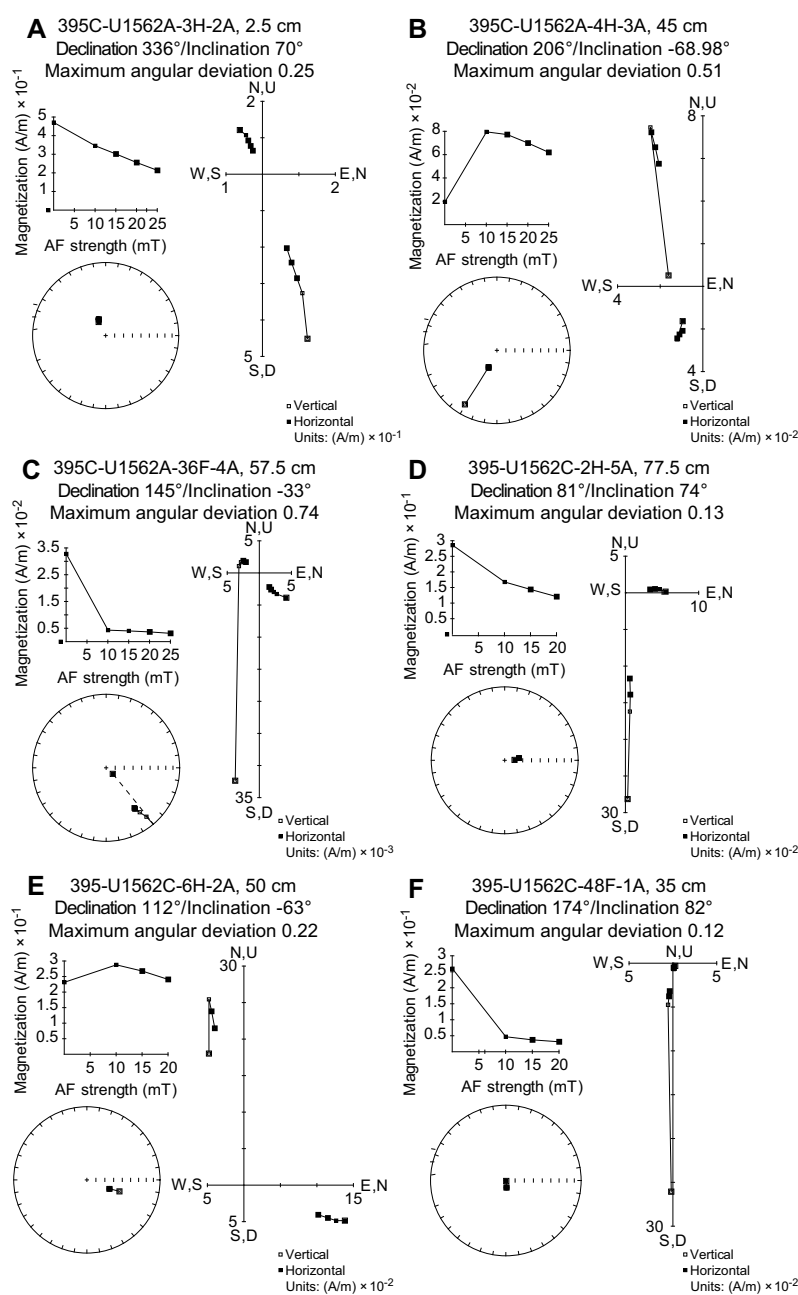

Figure F44. Demagnetization behaviors of sediments, Holes U1562A and U1562C. A, D. Normal polarity samples. B, E. Reversed polarity samples. C, F. Samples showing early decay at 10 mT. Declination and inclination of remanent magnetization at progressive demagnetization steps are displayed on both stereographic projection and Zijderveld diagrams (Zijderveld, 1967). Intensity of remanent magnetization is plotted against treatment value. Zijderveld diagrams: solid symbols = declination, open symbols = inclination. Stereographic plots: solid symbols = positive (down-pointing) inclination, open symbols = negative (up-pointing) inclination.

The transition from sedimentary to igneous rocks occurs at ~430 m CSF-A with considerable change in NRM intensity and two orders of magnitude increase in MS (Figure **F49**).

9.4. Magnetostratigraphy

The magnetostratigraphy of Site U1562 is based on the correlation of the polarity assigned to the archive-half cores from Hole U1562A using inclinations after 25 mT demagnetization and the polarities reported in the reference geomagnetic polarity timescale (GPTS) (Table **T13**). Importantly, the magnetic events recognized in Hole U1562A (Figure **F45**) are also identified in Hole U1562C (Figure **F46**). In sections where soft-sediment deformation is present, the inclination record is most likely disturbed and not interpretable in terms of magnetic polarities.

The magnetostratigraphic data from Hole U1562A were correlated to the GPTS (Ogg, 2020) and plotted along with the tie points from the microfossil ages (see **Age model**). A succession of 14 normal and 14 reversed intervals was recognized (Figure **F47**).

The boundary between the Brunhes and Matuyama Chrons was interpreted at ~13 m CSF-A (0.773 Ma), and the transition from the Matuyama to Gauss Chrons was interpreted at ~108 m CSF-A (2.595 Ma) (Table **T13**).
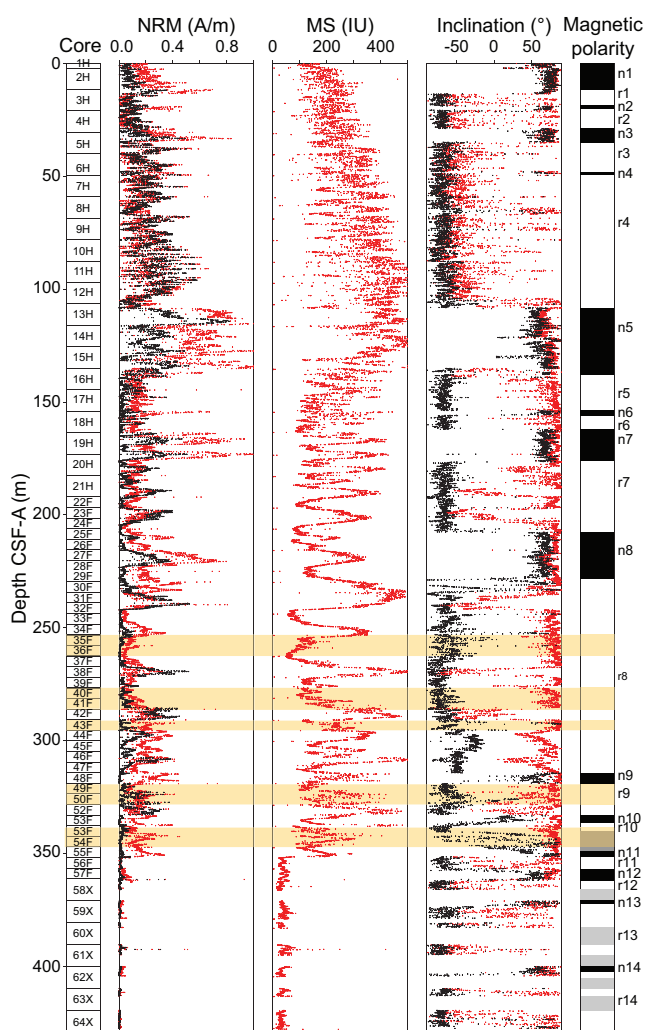

Figure F45. Paleomagnetic measurements, Hole U1562A. Yellow bands = intervals showing soft-sediment deformation. NRM and inclination: red = NRM, black = NRM after 25 mT AF demagnetization. Magnetic polarity interpretation of inclination: n = normal, r = reversed, gray = depth for which a polarity interpretation was not unequivocal, or there was no recovery.
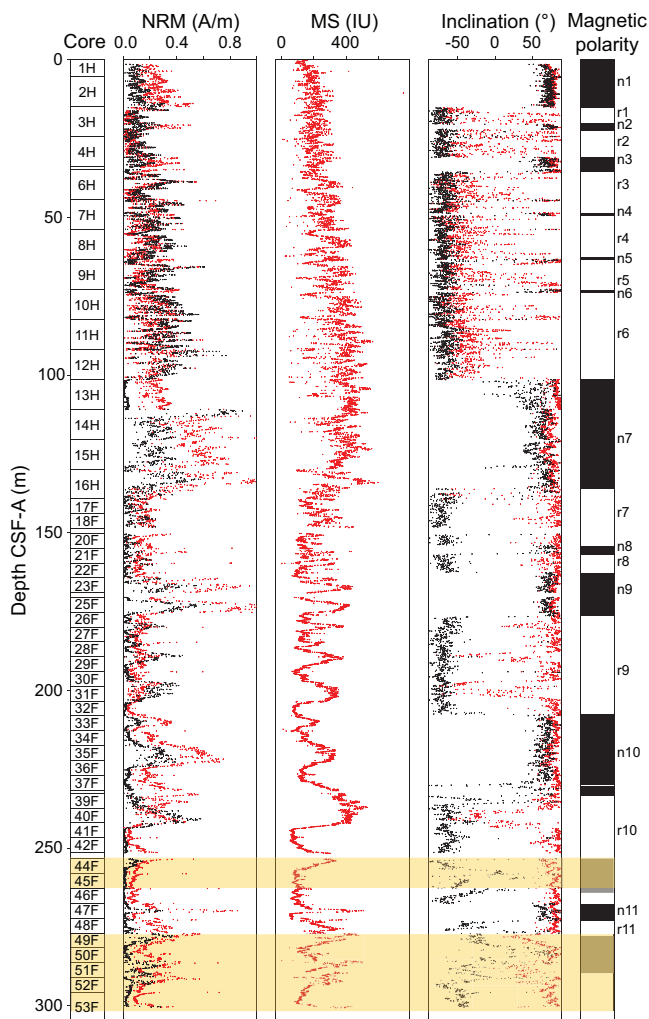
Figure F46. Paleomagnetic measurements, Hole U1562C. Yellow bands = soft-sediment deformation. NRM and inclination: red = NRM, black = NRM after 20 mT AF demagnetization. Magnetic polarity interpretation of inclination: n = normal, r = reversed, gray = depth for which a polarity interpretation was not unequivocal.
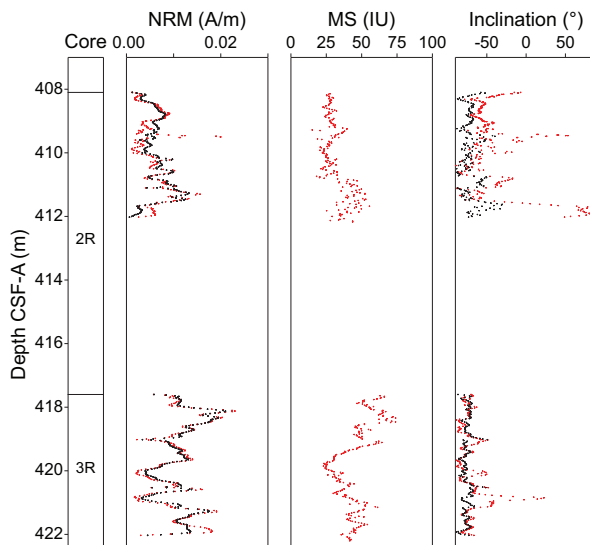

Figure F47. Paleomagnetic measurements from sediments, Hole U1562B. NRM and inclination: red = NRM, black = after 25 mT AF demagnetization.
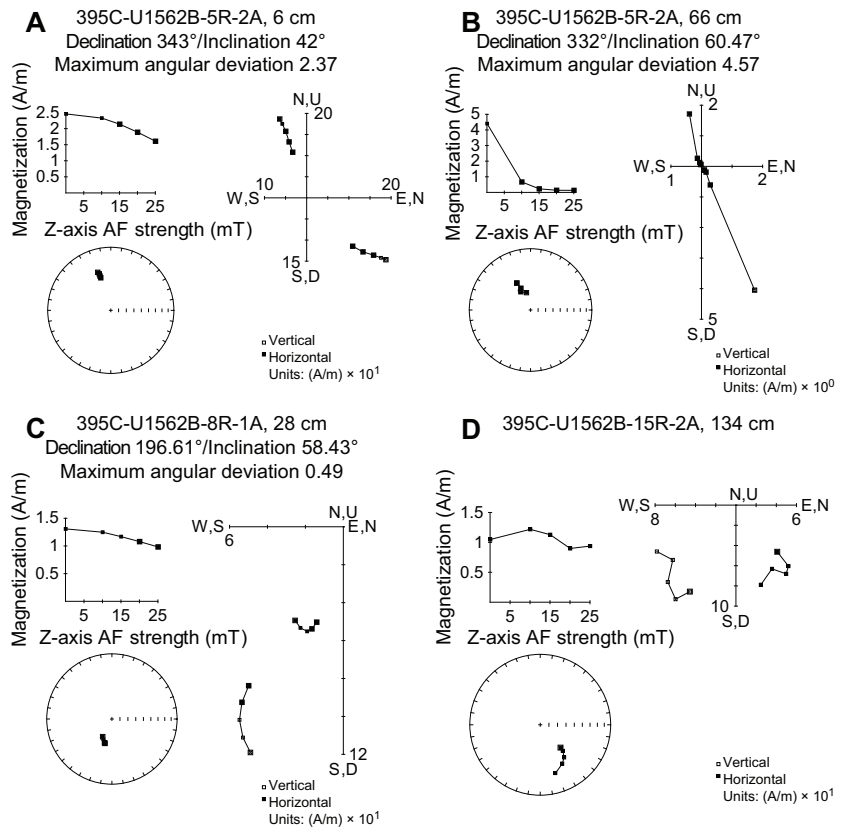
Figure F48. Demagnetization behaviors of basalts, Hole U1562B. A. Normal polarity sample. B. Normal polarity but a magnetization decaying at 15 mT. C. Normal polarity and a magnetization not decaying before 25 mT. D. Example of where it is difficult to isolate the ChRM and a polarity is not recognized. Declination and inclination of remanent magnetization at progressive demagnetization steps are displayed on both stereographic projection and Zijderveld diagrams (Zijderveld, 1967). Intensity of remanent magnetization is plotted against the treatment value. Zijderveld diagrams: solid symbols = declination, open symbols = inclination. Stereographic plots: solid symbols = positive (down-pointing) inclination, open symbols = negative (up-pointing) inclination.
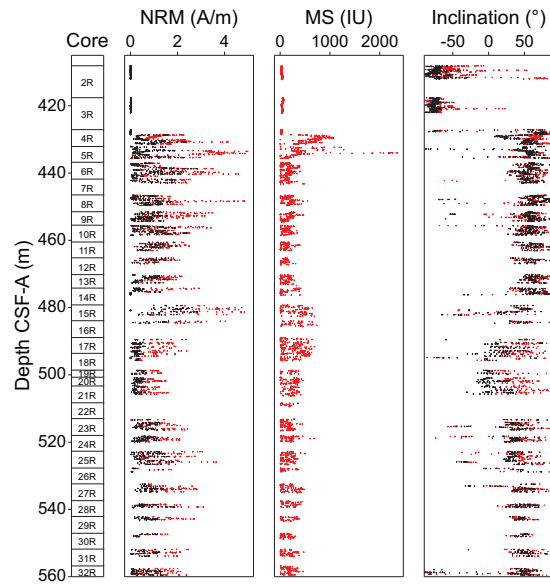

Figure F49. Paleomagnetic measurements, Hole U1562B. NRM and inclination: red = NRM, black = after 25 mT AF demagnetization.

Table T13. Paleomagnetic age datums, Hole U1562A and U1562C. n = normal, r = reverse. Base of magnetic polarities and sections are shown in Figures F45 and F46. Polarity subchron and base ages follow Ogg (2020). **Download table in CSV format.**

Magnetic polarity	Magnetic polarity base CSF-A (m)	Core, section	Magnetic polarity	Magnetic polarity base CSF-A (m)	Core, section	Polarity subchron	Base of chron/ subchron (Ma)
		395C-U1562A-			395C-U1562C-		
n1	13.43	3H-2	n1	15.20	3H-1	C1n (Brunhes)	0.773
r1	18.85	3H-5	r1	20.50	3H-4	C1r.1r (Matuyama)	0.990
n2	20.58	3H-7	n2	22.40	3H-5	C1r.1n (Jaramillo)	1.070
r2	28.83	4H-6	r2	31.00	4H-5	C1r.3r	1.775
n3	34.73	5H-3	n3	35.60	6H-1	C2n (Olduvai)	1.934
r3	48.00	6H-6	r5	48.70	7H-3	C2r.1r	2.116
n4	48.73	6H-6	n5	49.20	7H-4	C2r.1n (Feni)	2.140
r4	108.15	13H-2	r6	101.40	13H-1	C2r.2r (Matuyama)	2.595
n5	137.71	16H-2	n7	137.40	16H-6	C2An.3n	3.596
r6	153.73	17H-7	r7	153.70	20F-3	C2Ar	4.187
n7	176.44	20H-3	n9	175.70	26F-1	C3r.4n (Thvera)	5.235
r7	207.58	25H-2	r9	207.60	32F-4	C3r (Gilbert)	6.023
n8	228.40	29H-3	n10	229.00	37F-2	C3An.2n	6.727

10. Geochemistry and microbiology

Cores taken during Expedition 395C (Holes U1562A and U1562B) were analyzed for headspace gas, IW chemistry, and bulk sediment/basalt geochemistry. Cores taken during Expedition 395 (Hole U1562C) were analyzed for bulk sediment geochemistry. The geochemistry of basalts at Site U1562 is described in **Igneous petrology**. Headspace gas analyses were conducted on cores from Holes U1562A and U1562B; methane concentrations are low and range ~0 to 3 ppmv. Ethane was absent in all holes. IW calcium ion (Ca^{2+}) concentrations are highest near the sediment/water and sediment/basement interfaces. Magnesium ion (Mg^{2+}) concentrations display a generally decreasing trend with depth, with a small increase at the sediment/basement interface. Sulfate ion (SO_4^{2-}) concentrations have seawater-like values at the top and bottom of the sedimentary sequence and a minimum around 250 m CSF-A. $CaCO_3$ shows large variability but generally increases downcore, trending from ~0 to 33 wt% in the uppermost 100 m to ~83 wt% near the sediment/basement interface. Bulk sediment generally exhibits low total organic carbon (TOC), total nitrogen (TN), and total sulfur (TS) content.

10.1. Volatile hydrocarbons

Methane concentrations in the sedimentary section of Site U1562 (Holes U1562A and U1562B) increase from 0.4 ppmv at the sediment/water interface to a peak of 2.7 ppmv at 317.2 m CSF-A and then drop back to 0 ppmv at the sediment/basement interface (Figure **F50**). The slightly increased methane concentrations and the absence of ethane in the middle part of the sedimentary sequence suggest increased biogenic methane gas production and that thermogenic gas sources are unlikely.

10.2. Interstitial water chemistry

A total of 66 IW samples were squeezed from 5 or 10 cm long whole-round samples from 0.95 to 427.3 m CSF-A in Hole U1562A (Cores 1H–64X). One additional IW sample was collected from Section 395C-U1562B-14R-2, 17–27 cm, from an intercalated sediment layer in the basalt basement at 475.71 m CSF-A. Selected data acquired from analysis of IW in Holes U1562A and U1562B are shown in Figure **F51**. pH displays little variation throughout the sedimentary section (7.69 ± 0.07). Alkalinity varies from near seawater values at the top (Sample 395C-U1562A-1H-1, 95–100 cm; 3.0 mM) and bottom (Sample 64X-4, 142–152 cm; 3.6 mM) of the sediment to high values at 223.15 m CSF-A (e.g., Sample 28F-2, 145–150 cm; 7.9 mM). IW Mg^{2+} concentrations range 45.9–54.0 mM. Mg^{2+} concentrations are highest (~50 mM) at the top and bottom of the sedimentary sequence, with the lowest Mg^{2+} concentration (45.8 mM) occurring at 288.97 m CSF-A (Sample 44F-2, 146–151 cm). SO_4^{2-} concentrations range 18.5–28.9 mM with the highest values

observed at the top and bottom of the sediments. SO_4^{2-} concentrations are also high in the intercalated basalt-sediment Sample 395C-U1562B-14R-2, 17–27 cm (28.9 mM). Ca^{2+} concentrations range 6.3–10.6 mM, with the lowest concentrations in the middle part of the sedimentary sequence. Sr^{2+} concentrations range from 84.9 µM at 0.95 m CSF-A to 154.3 µM at 425.34 m CSF-A; they generally increase toward the bottom of the sediments but decrease to 87.7 µM at 475.71 m CSF-A in Section 14R-2.

10.2.1. Bulk sediment geochemistry

10.2.1.1. Carbonate, nitrogen, carbon, and sulfur

Discrete sediment samples (n = 76) were collected from squeeze cake residues and working-half sections during sediment description for Cores 395C-U1562A-1H through 64X (0.95–427.3 m CSF-A), 395C-U1562B-14R (475.71 m CSF-A), and 395-U1562C-3H through 50F (15.39–284.12 m CSF-A) and analyzed for total carbon (TC), TN, and total inorganic carbon (TIC). For Hole U1562C, sedimentary TS was also analyzed. TOC content and $CaCO_3$ weight percent were subsequently calculated from TIC and TC measurements. $CaCO_3$ varies from 0.04 to 82.9 wt%, with the highest content at 475.71 m CSF-A in the intercalated sediments from Section 395C-U1562B-14R-2, 17–27 cm (bottom sample in Figure **F52**). The sampling strategy for $CaCO_3$ analyses (and as a result carbon, nitrogen, and sulfur analyses) differed between the holes. For Holes U1562A and U1562B, sediment was collected from the squeeze cake residues and was therefore sampled independent of lithology. No IW samples were collected for Hole U1562C; therefore, additional sediment samples were chosen so that the resulting geochemical information (e.g., $CaCO_3$ content) could be used to aid in lithologic description. The apparent offset in the $CaCO_3$ content
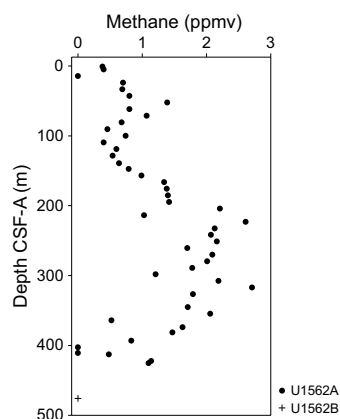

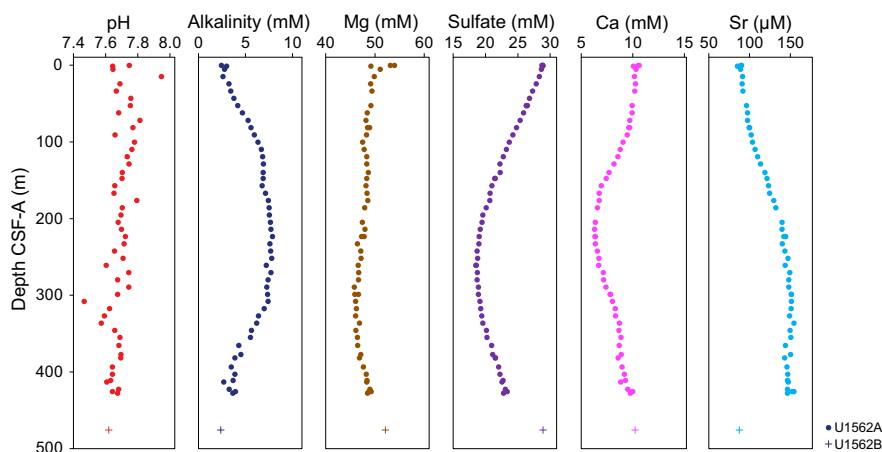**Figure F50.** Composite gas analyses of methane concentrations, Holes U1562A and U1562B.

Figure F51. IW pH, alkalinity, and concentrations of selected ions, Holes U1562A and U1562B.
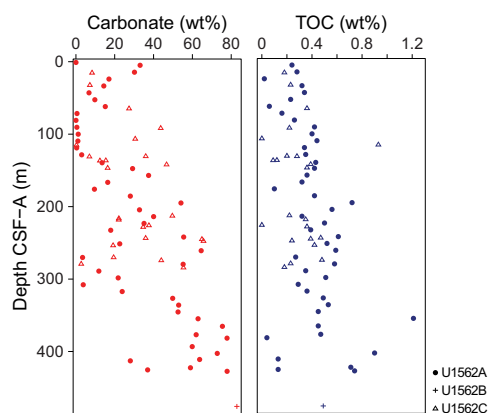
Figure F52. CaCO$_3$ and TOC from IW residues, Holes U1562A–U1562C. Sediment samples from Hole U1562C were selected from working halves to aid in sediment description.

between the two holes thus reflects the sampling bias and variable sedimentary CaCO$_3$ content in different lithologic layers, not a general difference in CaCO$_3$ content between the two holes. TOC is low (<1.21 wt%) and averages 0.38 ± 0.23 wt%. Four analyses for C and N fall outside of the upper quartile of data (above 2 wt%) and were excluded from the interpretation. TN is also very low (range = 0–0.08 wt%). TS was only measured for Hole U1562C (range = 0–1.09 wt%).

10.2.2. Microbiology

Microbiological sampling of sediments from Holes U1562A and U1562C was focused on collecting material for culture-independent approaches. A total of 49 sediment samples from Hole U1562A and 31 sediment samples from Hole U1562C, each 5 cm³, were collected with a sterile cut-end syringe. A total of 13 whole-round samples of hard rock were collected from Hole U1562B for shore-based microbiological analyses.

11. Downhole measurements

Details on tools and logging procedures can be found in **Downhole measurements** in the Expedition 395 methods chapter (Parnell-Turner et al., 2025a); only hole-specific procedures are detailed here. Downhole logging operations at Site U1562 were conducted in Hole 395C-U1562B, which was logged with the triple combo tool string (Magnetic Susceptibility Sonde [MSS], High-Resolution Laterolog Array [HRLA], Accelerator Porosity Sonde [APS], Hostile Environment Litho-Density Sonde [HLDS], and Hostile Environment Natural Gamma Ray Sonde [HNGS]), FMS-sonic tool string (FMS, Dipole Sonic Imager [DSI], General Purpose Inclinometry Tool [GPIT], and HNGS), UBI tool string (UBI, GPIT, and HNGS), and VSI tool string (VSI and HNGS) (Tables **T14**, **T15**). During coring in Hole 395C-U1562A, formation temperature measurements were acquired at four locations (Cores 4H, 7H, 10H, and 13H) using the APCT-3 tool (Table **T16**).

11.1. Logging procedure and log data processing and quality control

After coring operations were completed in Hole U1562B, the hole was cleaned and the pipe was raised to 89 m DSF (86 m WSF). The heavy mud used for drilling was then replaced with seawater. The triple combo tool string was deployed first and acquired a downhole log (Data Set 010LUP), a repeat uphole log (Data Set 011LUP) from 136 to 559 m WSF, and an uphole log to the seafloor (Data Set 017PUP). During the downhole logging pass, the calipers were closed and the APS was turned off; therefore, no APS or HLDS data were acquired in this logging pass. The FMS-sonic tool string was deployed and acquired a downhole log (Data Set 032PUP) with the calipers closed (no FMS image log acquired), a repeat uphole log from 419 to 558 m WSF (Data Set 033PUP), and a main uphole log (Data Set 034PUP) along the entire open hole (0–558 m WSF). The quality of the V_P from the monopole transmitter was deemed acceptable for the basement interval (426–545 m WSF) by the Lamont-Doherty Earth Observatory Borehole Research Group (LDEO-BRG), but

it was deemed poor in the sediment section, so V_P data for depths above 426 m WSF are not discussed here. The dipole shear velocities were deemed to be of good quality in the sediment section (~85–426 m WSF) and are discussed here. The third tool string deployed was the VSI tool string. A brief uphole VSI logging pass was performed from 81 to 113 m WSF to depth match the station depths to the other logging tools. Seismic data from four VSI stations were acquired at 556.6, 459.4, 428.5, and 420 m WSF. The final logging pass in Hole U1562B was the UBI tool string. An initial uplog (Data Set 050LUP) was acquired without the UBI switched on to collect a gamma log for depth matching (408–553 m WSF). Two more uphole logs were conducted, one from 410 to 553 m WSF (Data Set 051LUP) and another from 0 to 407 m WSF (Data Set 052LUP), to acquire acoustic borehole image logs with the UBI. Because of enlargement of Hole U1562B in the sedimentary section (0–426 m WSF), the UBI did not acquire a good quality acoustic image log above the basement.

The gamma log of the triple combo tool string uphole log (Data Set 017PUP) is used as the reference log for depth matching all logging data from Hole U1562B. Once depth matched, all logging data were depth shifted to a seafloor depth of 2015 m WMSF (0.5 m difference from the driller's depth of 2014.5 m drilling depth below rig floor [DRF]), which was determined by a step in the gamma log from the uphole log of the triple combo tool string (Data Set 017PUP). During logging operations, the wireline heave compensator (WHC) was used to counter the 0.25–0.5 m of ship heave.

Table T14. Logging passes in Hole 395C-U1562B and APCT-3 in situ formation temperature measurements in Hole 395C-U1562A. NA = not applicable. **Download table in CSV format.**

Hole	Tool string	Tool list	Logging pass	Logging data reference	From depth WSF (m)	To depth WSF (m)	Pipe depth WSF (m)	Notes
395C-								
U1562A	APCT-3	Formation temperature	NA	NA	21	116	NA	4 measurements acquired
U1562B	Triple combo	MSS-B/HRLA/APS/HLDS/HNGS	Downlog	010LUP	0	559	86	Caliper closed
			Repeat (uplog)	011LUP	136	559	86	Recorded open hole
			Main (uplog)	017PUP	0	559	86	Reference pass
	VSI	VSIT/HNGS	NA	NA	81	113	86	4 stations acquired
	FMS-sonic	FMS/DSI-2/GPIT/HNGS	Downlog	032PUP	0	485	86	Caliper closed
			Repeat (uplog)	033LUP	419	558	86	Recorded open hole
			Main (uplog)	034PUP	0	558	86	
	UBI	UBI/GPIT/HNGS	Uplog	052LUP	408	553	86	No image
			Uplog	051LUP	410	553	86	
			Downlog	050LUP	0	407	86	

Table T15. Downhole logging units, Hole U1562B. **Download table in CSV format.**

Logging unit	Hole 395C-U1562B depth WMSF (m)	Lithology
L1a	0–86	Sediment
L1b	86–136	Sediment
L2a	136–305	Sediment
L2b	305–350	Sediment
L3	350–426	Sediment
L4	426–560	Basalt

Table T16. APCT-3 measurements, Hole U1562A. **Download table in CSV format.**

Section	Depth DSF (m)	Formation temperature (°C)
395C-U1562A-		
4H	30.5	4.27
7H	59	5.37
10H	79	6.46
13H	116	7.34

The borehole diameter was enlarged in the sediment section of Hole U1562B, generally between 13 and 17 inches, which is larger than bit size (~9.875 inches). Hole enlargement affects most measurements, especially those acquired with tools that require eccentralization and a good contact to the borehole wall. In the basement, the hole size is mostly close to the bit size with only short, localized enlargements.

Image log quality is mostly poor for both the acoustic and resistivity image logs in the sedimentary portion of Hole U1562B but is of higher quality in the basement section (>426 m WMSF). FMS caliper data show the hole is ovalized at 135–240 m WMSF, with shorter intervals of complete borehole widening to diameters of ~14.5 inches. From ~240 to 426 m WMSF, the hole is enlarged to diameters of ~15 inches. In the basement section, Hole U1562B has a diameter in good agreement with bit size (~9.875 inches) with only slight widening of the hole diameter between 464 and 476 m WMSF.

11.2. Logging units

Four logging units (Unit L1 = 0–136 m WMSF; Unit L2 = 136–350 m WMSF; Unit L3 = 350–426 m WMSF; Unit L4 = 426–560 m WMSF) are defined for Hole U1562B based on downhole logging responses (Figure **F53**). Logging subunits are defined in Unit L1 to account for logging in drill pipe and open hole and in Unit L2 based on further variations in the MS and shear wave velocity (V_S).

11.2.1. Logging Unit L1

Depth: 0–136 m WMSF

Logging Unit L1 starts at the seafloor, and its boundary with Unit L2 is defined by an increase in gamma radiation at ~136 m WMSF. Despite the drill pipe repressing the gamma measurements in the upper portion of Unit L1 (Subunit L1a), the overall character of the gamma log is similar throughout Unit L1. Furthermore, this logging unit correlates with Lithostratigraphic Unit I (0–135 m CSF-A) (see **Lithostratigraphy**), including Logging Subunits L1a and L1b.

11.2.1.1. Logging Subunit L1a

Depth: 0–86 m WMSF

Downhole logging in the uppermost 86 m of Hole U1562B was acquired through drill pipe. Therefore, only suppressed gamma log measurements can be used to assess the formation. Logging Subunit L1a gamma logs show an average reading of 1.56 ± 0.7 American Petroleum Institute gamma radiation units (gAPI) (Figure **F53**).

11.2.1.2. Logging Subunit L1b

Depth: 86–136 m WMSF

Below the drill pipe, Logging Subunit L1b was measured with a full suite of wireline logs except V_P, which returned unreliable data for this interval (Figure **F53**). The gamma log increases to a mean value of 15.6 ± 2.5 gAPI and shows multiple peaks of up to ~25 gAPI. Spectral gamma log peaks are influenced by a Th signal of up to 2.8 ppm. Density increases with depth in Subunit L1b from ~1.2 to ~1.6 g/cm³. Electrical resistivity is variable in Subunit L1a, although values fluctuate little from ~0.7 Ωm. V_S increases from ~235 m/s to 390 m/s with depth in Subunit L1b. MS is variable throughout Subunit L1b, ranging 15–275 SI.

11.2.2. Logging Unit L2

Depth: 136–350 m WMSF

Logging Unit L2 is characterized by an overall high gamma signal (average = 20.5 ± 2.8 gAPI) that displays a cyclic pattern on a meter to decimeter scale (Figure **F53**). Peaks in the gamma signal are largely from a Th component. This cyclic logging response is also observed in the MS, V_S, and porosity measurements of this logging unit. Electrical resistivity (~0.8 Ωm), density (1.6 g/cm³), and porosity (0.75) are largely invariable with depth in Unit L2. Subunits L2a and L2b are differen-

tiated from each other based on the wavelength of these logging response cycles. Unit L2 correlates to Lithostratigraphic Units II and III (see **Lithostratigraphy**).

11.2.2.1. Logging Subunit L2a

Depth: 136–305 m WMSF

Logging Subunit L2a shows cyclic behavior in both V_S and MS, the length scale of which increases with depth from meter scale to decameter scale. MS and V_S appear to show a negative correlation
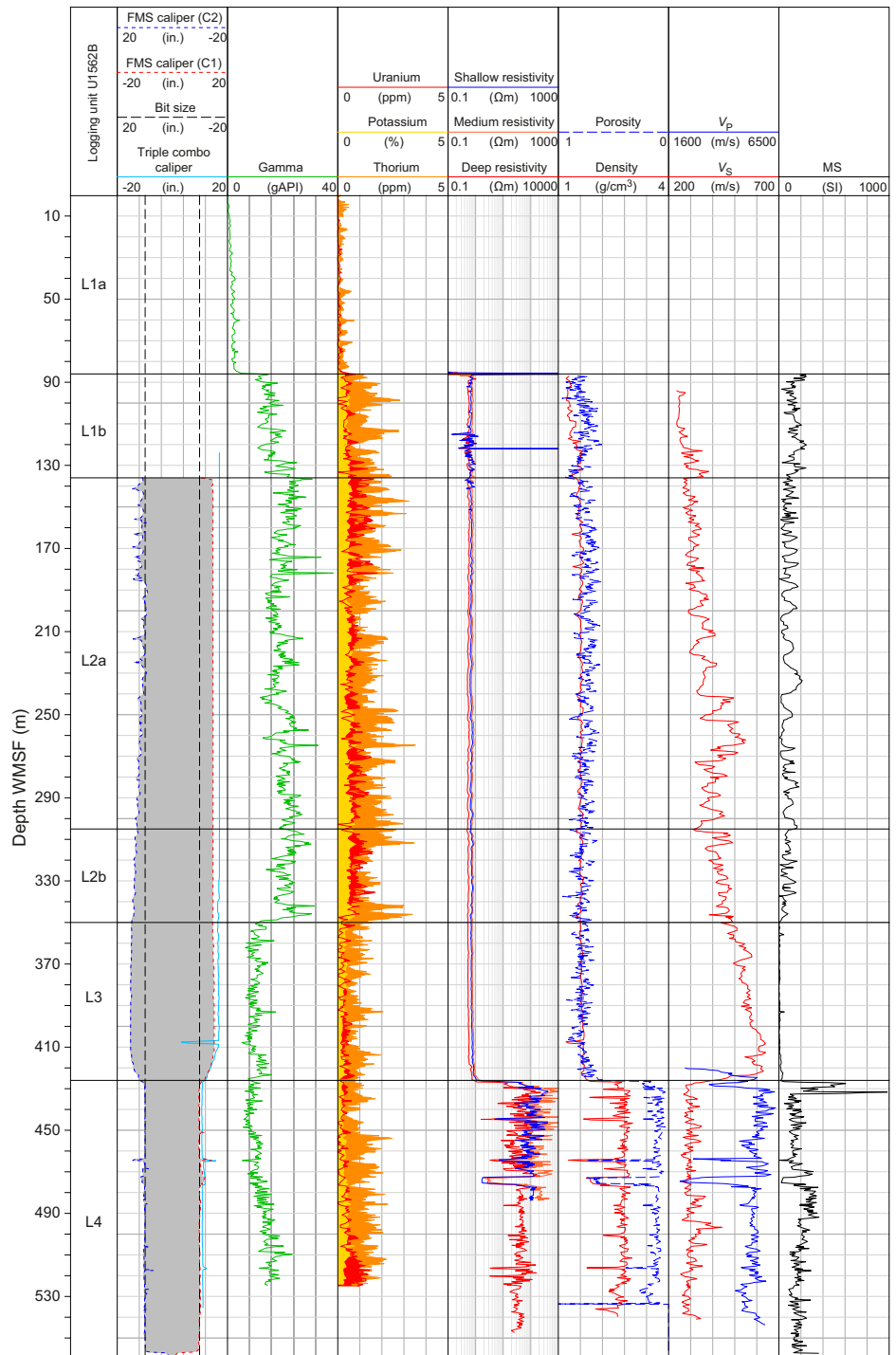

Figure F53. Downhole logging data, Hole U1562B. in = inches.

such that when the MS of the sediment increases, V_S decreases and vice versa. V_S also shows an overall increase with depth in Subunit L2a from ~280 m/s up to between 345 and 550 m/s.

11.2.2.2. Logging Subunit L2b

Depth: 305–350 m WMSF

Logging Subunit L2b shows the same V_S and MS cyclic behavior observed in Subunit L2a, although they occur at a shorter, meter scale, and the cycles appear to diminish with depth. MS and V_S continue to show a negative correlation, and V_S shows an initial drop from the bottom of Subunit L2a and then an increase with depth in Subunit L2b from ~300 to ~500 m/s.

11.2.3. Logging Unit L3

Depth: 350–426 m WMSF

The boundary between Logging Units L2 and L3 is marked by a sharp drop in gamma radiation, and Unit L3 displays an average of 10.2 ± 1.7 gAPI (Figure **F53**). The gamma log shows increased peaks in this logging unit, which, like the units above it, is dominated by a Th signal, as shown by the spectral gamma log. Electrical resistivity reports the same values as Unit L2 (~0.85 Ωm) with a slight increase at the bottom of the unit as it approaches Unit L4. Density increases with depth in Unit L3 from 1.6 to 1.8 g/cm³. At ~407 m WMSF, the caliper shows a narrowing of the hole, which is also reflected in an artificial drop in density. V_S increases with depth in Unit L3 from ~440 to ~650 m/s. The lowermost part of Unit L3 (420–426 m WMSF) produced reliable V_P measurements that show a rapid increase downward toward the top of Unit L4, from ~2300 to 5500 m/s. MS is invariably low in Unit L3 (average = 7.9 SI) and only shows a slight increase of up to ~40 SI at the bottom of the unit. Unit L3 correlates to Lithostratigraphic Unit IV (see **Lithostratigraphy**).

11.2.4. Logging Unit L4

Depth: 426–560 m WMSF

Logging Unit L4 represents the basement sequence drilled in Hole U1562B (Figure **F53**). The boundary between Units L3 and L4 is defined by marked changes in resistivity, density, porosity, V_P, V_S, and MS. The gamma log shows an initial decrease to ~7 gAPI at the top of Unit L4 that gradually increases with depth to as high as ~23 gAPI. The spectral gamma log has a strong Th signal to ~515 m WMSF, below which it becomes mostly a U signal. The transition from the sediment strata to the basement basalt is obviously marked by the previously mentioned increase in electrical resistivity (from deep-resistivity values of ~0.85 to ~51 Ωm), an increase in density (from 1.7 to 2.7 g/cm³), a decrease in porosity (from ~0.6 to 0.16), a decrease in V_S (from 630 to 230 m/s), an increase in V_P (from 3350 to 6090 m/s), and an initial large increase in MS (from ~13 to 605 SI). All logging responses show variability throughout the basement sequence, with increases in MS correlating to increases in V_P, density, and resistivity and decreases in porosity and vice versa. A notable interval at 472–476 m WMSF with low resistivity (deep resistivity of ~6.5 Ωm), high porosity (~0.62), low density (~1.8 g/cm³), low V_P (2400 m/s), and low MS (~30 SI) may correlate to an intermixed sediment layer recovered in the basement basalts (see **Lithostratigraphy**). Similar meter-scale logging signatures can be observed throughout Unit L4 (e.g., ~464 m WMSF) that may represent further sediment layers in the basement, most of which have not been recovered in the cored material.

11.3. Borehole imaging

The resistivity image log acquired in the sedimentary sequence in Hole U1562B shows alternating conductive and resistive layering (Figure **F54**), and a mottling pattern is particularly apparent from 300 to 430 m WMSF (Subunit L2b and Unit L3). Unit L2 displays some apparently cyclic behavior in the resistivity logs; however, the frequent ledges and borehole breakouts of the hole make it difficult to interpret the signal clearly. Both the acoustic and resistivity image logs are of excellent quality in the basement sequence in Hole U1562B (>430 m WMSF) (Figure **F54**). Both image logs show a mostly featureless basement with some fractured to very fractured intervals that are provisionally interpreted to be small pillow lava structures. An interval of sediment is observable on

image logs at ~472–475 m WMSF (Figure **F55**). At some depths, wide fractures can be observed, marked by low acoustic and low resistivity values in the images (e.g., ~516 m WMSF; Figure **F54**).

11.4. Downhole temperature and thermal conductivity

During coring in Hole U1562A, downhole temperature measurements were taken with the APCT-3 tool in Unit L1. The APCT-3 tool provided equilibration temperatures ranging from 4.27°C at 30.5 m CSF-A to 7.34°C at 116 m CSF-A (Figure **F56**; Table **T16**). These observations indicate a
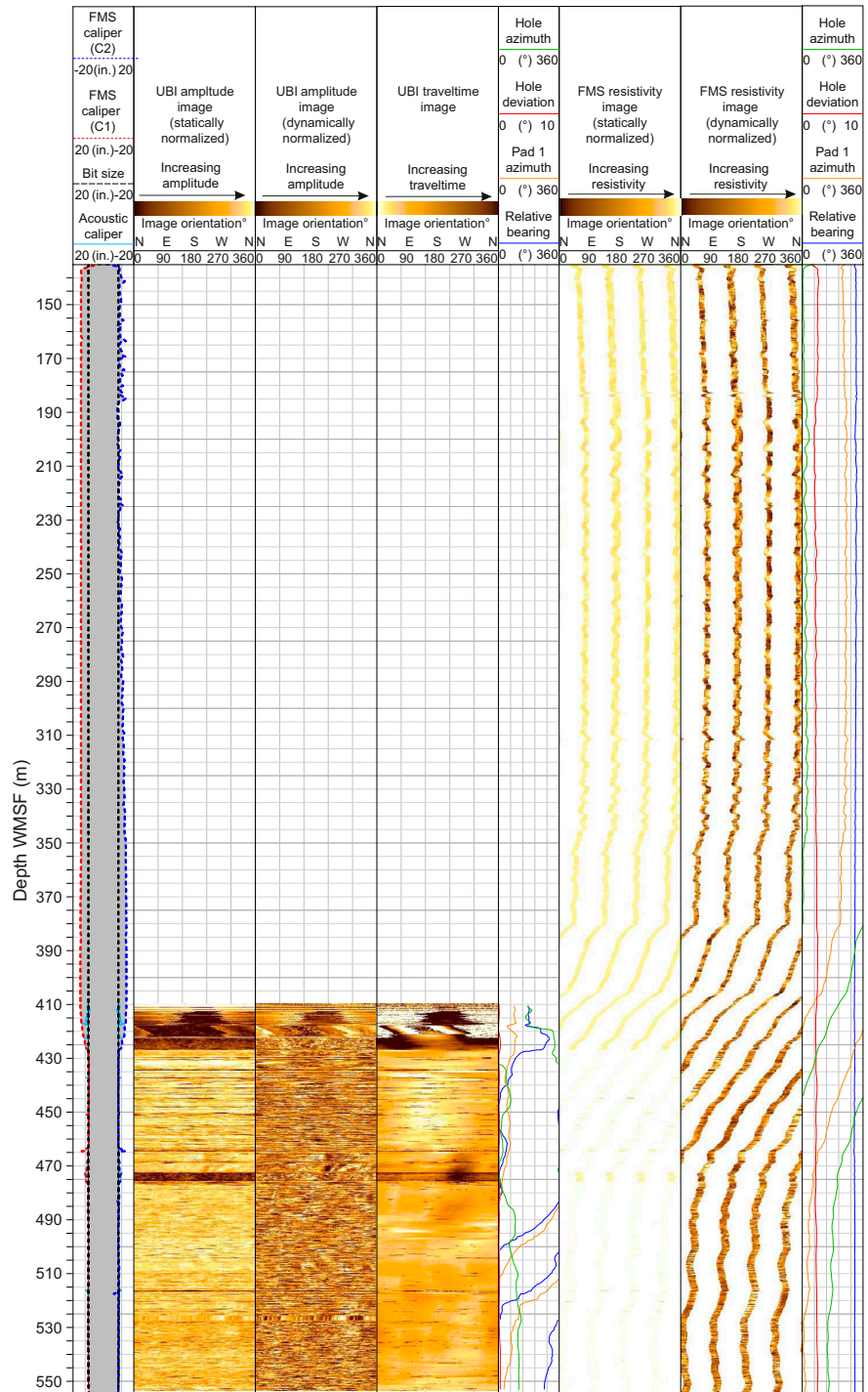

Figure F54. Wireline image data, Hole U1562B. in = inches.

thermal gradient in the upper sediment section of 36°C/km (Figure **F57A**). Thermal conductivity under in situ conditions (K) was estimated from laboratory-determined thermal conductivity from Hole U1562A using the method of Hyndman et al. (1974); it varies slightly, but mostly has values around 0.8 to 0.9 W/m·K (Figure **F57B**). A linear function for depth-dependent thermal resistance (*R*) was obtained by integrating the inverse of the thermal conductivity over depth and applying a linear least-squares fit (Figure **F57C**). This function was used to estimate thermal resistance at each corresponding APCT-3 downhole temperature measurement depth. A heat flow of 33.5 mW/m² was obtained from a linear least-squares fit of the relationship between temperature and thermal resistance (Bullard, 1939), whose slope is the vertical heat flow (Figure **F57D**).
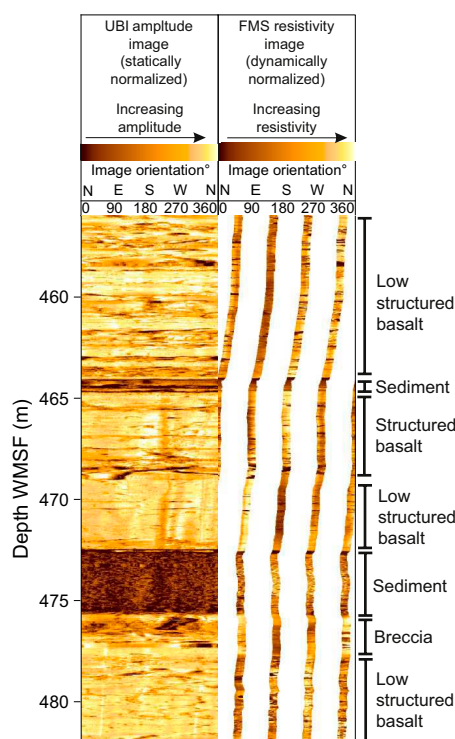

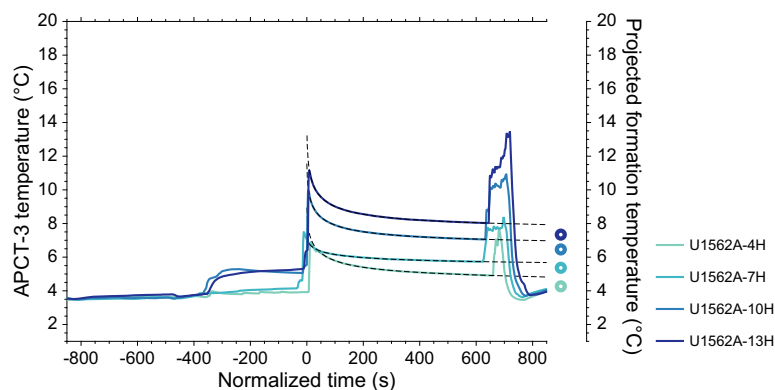**Figure F55.** Basalt basement image features, Hole U1562B.

Figure F56. APCT-3 temperature-time series and projected formation temperatures, Hole U1562A. Colored lines = observed temperature-time series, dashed lines = modeled heat pulse decay function (Hartmann and Villinger, 2002), colored dots = formation temperatures projected using best-fitting heat pulse decay function. Time is normalized with respect to onset of heat pulse decay model.
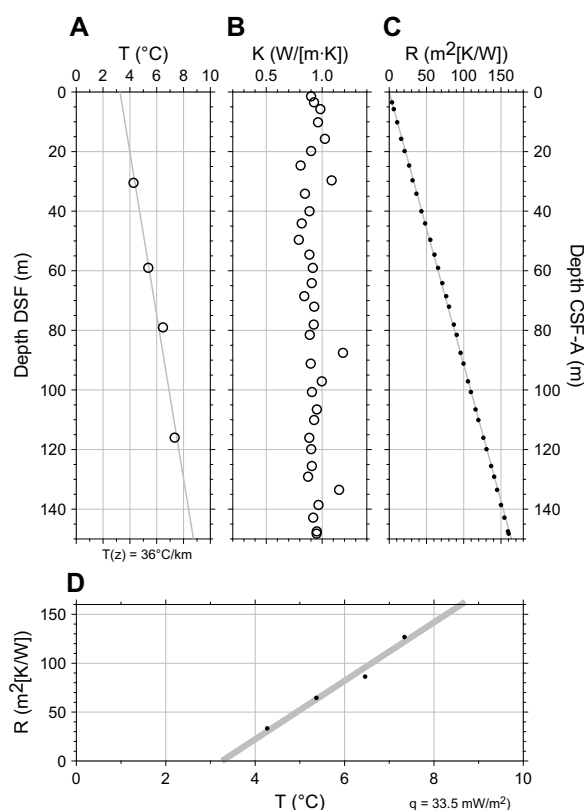
Figure F57. Thermal gradient and heat flow estimates, Hole U1562A. A. Projected APCT-3 formation temperature (open circles). Gray line = linear least-squares fit, *T(z)* = thermal gradient. B. Observed thermal conductivity. C. Calculated thermal resistance (*R*) (black dots). Gray line = linear least-squares fit for resistance as a function of depth, *R(z)*. D. Temperature as a function of thermal resistance (black dots) (i.e., Bullard plot). Gray line = linear least-squares fit, the gradient of which is vertical heat flow (*q*).

12. Age model

Site U1562, located near the eastern edge of Björn drift, has a thinner sedimentary succession than Site U1554, which is located near the center of the drift as imaged on Seismic Profile JC50-1 (see **Background and objectives**). Seismic Profile JC50-1 indicates that the upper part of the succession at Site U1562, from the seafloor reflection at ~2.7 s TWT to an angular discordance at ~2.9 s TWT, corresponds to a package of sediment that can be traced along the profile to Site U1554. Cores recovered from Site U1554 showed that this part of the succession had rapid sedimentary accumulation rates (up to ~17 cm/ky) and sedimentary facies consistent with a contourite deposit (see **Age model** in the Site U1554 chapter [Parnell-Turner et al., 2025b]). This package of sediment, which we attribute to the Björn drift depositional system, thins out eastward along the seismic reflection profile in the direction of Site U1562, but the thinning is not uniform, and a substantial stratigraphic interval within it appears to be pinched out at Site U1562 around ~2.75 s TWT. In contrast to the upper part of the succession at Site U1562, below ~2.9 s TWT the succession appears substantially thicker than the stratigraphically equivalent strata at Site U1554. From ~2.9 to ~3.05 s TWT, the seismic profile shows a series of relatively continuous parallel reflections, but below that level the reflections are less coherent to ~3.15 s TWT and then more coherent again down to the prominent basement reflection at ~3.25 s TWT.

Magnetostratigraphic (see **Paleomagnetism**) and biostratigraphic (see **Micropaleontology**) age constraints for the sedimentary succession in Holes 395C-U1562A and 395-U1562C are combined as an age-depth plot in Figure **F58**. The selected age model tie points are listed in Table **T17**. The succession appears relatively continuous to ~22 m CSF-A with a sedimentation rate of ~1.8 cm/ky. From ~22 m CSF-A to the base of Subchron C1r.3r at 28.83 m CSF-A, the succession is evidently
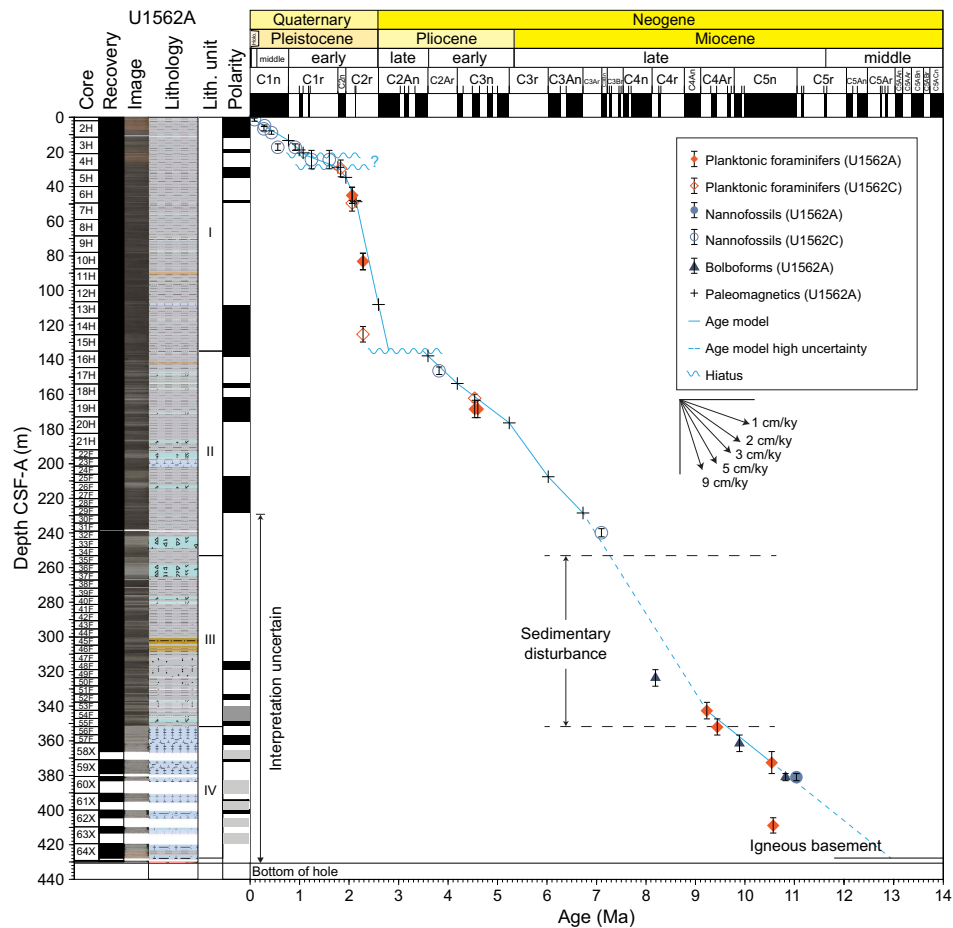
Figure F58. Age model, Hole U1562A. Additional biostratigraphic constraints from Hole U1562C are shown.

Table T17. Age model tie points, Hole U1562A. X = coiling reversal, d-s = dextral to sinistral. **Download table in CSV format.**

Tie point	Event (base)	Age (Ma)	Depth CSF-A (m)
1	Top of hole	0.000	0.00
2	C1n (Brunhes)	0.773	13.43
3	C1r.1n (Jaramillo)	1.070	20.58
4	Top condensed interval (extrapolated down)	1.13	22.00
5	Bottom condensed interval (extrapolated up)	1.78	28.83
6	C1r.3r	1.775	28.83
7	C2n (Olduvai)	1.934	34.73
8	C2r.1n (Feni)	2.140	48.73
	Base Pleistocene	2.59	107.50
9	C2r.2r (Matuyama)	2.595	108.15
10	Lithostratigraphic Unit I (hiatus?) (extrapolated down)	2.80	135.00
11	Lithostratigraphic Unit I (hiatus?) (extrapolated up)	3.50	135.00
12	C2An.3n (Base upper Pliocene)	3.596	137.71
13	C2Ar	4.187	153.73
14	C3r.4n (Thvera)	5.235	176.44
	Base Pliocene	5.33	180.19
15	C3r (Gilbert)	6.023	207.58
16	C3An.2n	6.727	228.40
	Lithostratigraphic Unit II	7.27	253.10
	X d-s *Neogloboquadrina atlantica*	9.23	342.61
	Lithostratigraphic Unit III	9.61	351.36
17	Top *P. mayeri*	10.54	372.58
	Base upper Miocene	11.65	397.97
18	Lithostratigraphic Unit IV	12.95	427.73

condensed and/or subject to hiatuses. Subchron C1r.2n (Cobb Mountain; 1.180–1.215 Ma) appears to be missing despite good recovery (see **Paleomagnetism**). The interval may correspond to the pinching out of seismic reflections at ~2.75 s TWT discussed above. Below 28.83 m CSF-A, there is a marked change in the character of the MS record from higher to lower frequency cyclicity downcore (see **Stratigraphic correlation**). The succession from this depth to the base of Lithostratigraphic Unit I at 135 m CSF-A contains a sequence of magnetic reversals in Chron 2 (Matuyama), providing constraints for a relatively rapid sedimentation rate of ~10 cm/ky.

The succession around the top of Lithostratigraphic Unit II at 135 m CSF-A is interpreted as a likely hiatus or series of closely spaced hiatuses that cut out or truncate a series of paleomagnetic reversals in the late Pliocene. It probably corresponds to the angular discordance in the seismic reflection profile at ~2.9 s TWT noted above. Below that level in Unit II, the biostratigraphic datums suggest a simple age-depth relationship that can be refined by the magnetostratigraphy to the base of Subchron C3An.2n (6.727 Ma) at 228.40 m CSF-A. The upper part of Unit II to the base of the Thvera Subchron C3r.4n (5.235 Ma) has an average sedimentation rate of ~2.4 cm/ky. The lower part of Unit II, from the base of Subchron C3r.4n to the base of Subchron C3An.2n, has a higher average sedimentation rate of ~3.5 cm/ky.

Lithostratigraphic Unit III (253.10 to 351.36 m CSF-A) is characterized by multiple intervals of severe soft-sediment deformation that likely indicate successive episodes of mass sediment transport (see **Lithostratigraphy**). This unit likely corresponds to the relatively incoherent part of the seismic reflection profile between ~3.05 and ~3.15 s TWT discussed above. Although the sedimentary succession registers a series of magnetic polarity reversals throughout the lower part of Unit III and Unit IV, the paleomagnetic interpretation relative to the GPTS is uncertain because of sedimentary complications and poor core recovery in Cores 395C-U1562A-58X through 64X (see **Paleomagnetism**).

The age model for the lower part of the succession in Hole U1562A is based on a series of foraminifer, bolboform, and nannofossil biohorizons. These constraints are considered to have low reliability for various reasons related to taxonomic uncertainty, low or variable abundances, and/or age calibration issues (see **Micropaleontology**). Taken together, however, they suggest a downward age progression with an average sedimentation rate of ~2.3 cm/ky. Lithostratigraphic Unit IV, from 351.36 m CSF-A to the basement at 427.73 m CSF-A, is characterized by sedimentary cyclicity of a fairly consistent character and wavelength as manifested in color reflectance and MS records (see **Physical properties** and **Downhole measurements**). Linear extrapolation of the age model trend to the base of Unit IV suggests an approximate age of 13.0 Ma for the oldest part of the regular sedimentary succession at the site. The age of the basement is estimated at 13.86 Ma from regional magnetic surveys (see **Background and objectives**).

A ~65 cm interval of laminated and bioturbated mudstone was found ~45 m below the top of the igneous succession in Section 395C-U1562B-14R-2 (see **Lithostratigraphy**). This interval corresponds to a highly distinctive ~3 m thick interval observed in the downhole resistivity and density image logs at 472.5–475.5 m WMSF (see **Downhole measurements**). The lithology is similar to Lithostratigraphic Unit IV at the base of the regular sedimentary succession but contains different assemblages of nannofossils, foraminifers, and bolboforms. The age difference from the sediment at the bottom of the regular sedimentary succession is currently difficult to constrain (see **Micropaleontology**), but the distinctive microfossil assemblage and apparently baked nature of the sediment suggest it is unlikely to have infiltrated from above, and therefore probably accumulated on the seafloor before being buried by lava flows. If the ~3 m of sediment accumulated at the same rate as Unit IV, it would imply ~130 ky of deposition.

References

Aksu, A.E., and Kaminski, M.A., 1989. Neogene and Quaternary planktonic foraminifer biostratigraphy and biochronology in Baffin Bay and the Labrador Sea. In Srivastava, S.P., Arthur, M., Clement, B., et al., Proceedings of the Ocean Drilling Program, Scientific Results. 105: College Station, TX (Ocean Drilling Program), 287–304. **https://doi.org/10.2973/odp.proc.sr.105.122.1989**

Bullard, E.C., 1939. Heat flow in South Africa. Proceedings of the Royal Society of London, A: Mathematical and Physical Sciences, 173(955):474–502. **https://doi.org/10.1098/rspa.1939.0159**

Butterworth, S., 1930. On the theory of filter amplifiers. Experimental Wireless and the Wireless Engineer, 7:536–541. **https://www.gonascent.com/papers/butter.pdf**

Chaisson, W.P., and Pearson, P.N., 1997. Planktonic foraminifer biostratigraphy at Site 925: middle Miocene-Pleistocene. In Shackleton, N.J., Curry, W.B., Richter, C., and Bralower, T.J. (Eds.), Proceedings of the Ocean Drilling Program, Scientific Results. 154: College Station, TX (Ocean Drilling Program), 3–31. **https://doi.org/10.2973/odp.proc.sr.154.104.1997**

Foresi, L.M., Iaccarino, S.M., and Salvatorini, G., 2002. Neogloboquadrina alantica preatlantica, new subspecies from late Middle Miocene. Rivista Italiana Di Paleontologia E Stratigrafia, 108(2). **https://doi.org/10.13130/2039-4942/5479**

Hartmann, A., and Villinger, H., 2002. Inversion of marine heat flow measurements by expansion of the temperature decay function. Geophysical Journal International, 148(3):628–636. **https://doi.org/10.1046/j.1365-246X.2002.01600.x**

Hyndman, R.D., Erickson, A.J., and Von Herzen, R.P., 1974. Geothermal measurements on DSDP Leg 26. In Davies, T.A., Luyendyk, B.P., et al., Initial Reports of the Deep Sea Drilling Project. 26: Washington, DC (US Government Printing Office), 451–463. **https://doi.org/10.2973/dsdp.proc.26.113.1974**

Jones, S.M., Murton, B.J., Fitton, J.G., White, N.J., Maclennan, J., and Walters, R.L., 2014. A joint geochemical–geophysical record of time-dependent mantle convection south of Iceland. Earth and Planetary Science Letters, 386:86–97. **https://doi.org/10.1016/j.epsl.2013.09.029**

Kirschvink, J.L., 1980. The least-squares line and plane and the analysis of palaeomagnetic data. Geophysical Journal International, 62(3):699–718. **https://doi.org/10.1111/j.1365-246X.1980.tb02601.x**

Lurcock, P.C., and Florindo, F., 2019. New developments in the PuffinPlot paleomagnetic data analysis program. Geochemistry, Geophysics, Geosystems, 20(11):5578–5587. **https://doi.org/10.1029/2019GC008537**

Lyons, R.G., 2011. Understanding Digital Signal Processing (Third edition): Upper Saddle River, NJ (Prentice Hall). **https://www.iro.umontreal.ca/~mignotte/IFT3205/Documents/UnderstandingDigitalSignalProcessing.pdf**

Murton, B.J., Taylor, R.N., and Thirlwall, M.F., 2002. Plume–ridge Interaction: a geochemical perspective from the Reykjanes Ridge. Journal of Petrology, 43(11):1987–2012. **https://doi.org/10.1093/petrology/43.11.1987**

Ogg, J.G., 2020. Geomagnetic Polarity Time Scale. In Gradstein, F.M., Ogg, J.G., Schmitz, M., and Ogg, G. (Eds.), Geologic Time Scale 2020. Amsterdam (Elsevier), 159–192. **https://doi.org/10.1016/B978-0-12-824360-2.00005-X**

Parnell-Turner, R., White, N., Henstock, T.J., Jones, S.M., Maclennan, J., and Murton, B.J., 2017. Causes and consequences of diachronous v-shaped ridges in the North Atlantic Ocean. Journal of Geophysical Research: Solid Earth, 122(11):8675–8708. **https://doi.org/10.1002/2017JB014225**

Parnell-Turner, R.E., Briais, A., LeVay, L.J., Cui, Y., Di Chiara, A., Dodd, J.P., Dunkley Jones, T., Dwyer, D., Eason, D.E., Friedman, S.A., Hemming, S.R., Hochmuth, K., Ibrahim, H., Jasper, C., Karatsolis, B.T., Lee, S., LeBlanc, D.E., Lindsay, M.R., McNamara, D.D., Modestou, S.E., Murton, B., OConnell, S., Pasquet, G.T., Pearson, P.N., Qian, S.P., Rosenthal, Y., Satolli, S., Sinnesael, M., Suzuki, T., Thulasi Doss, T., White, N.J., Wu, T., and Yang Yang, A., 2025a. Expedition 395 methods. In Parnell-Turner, R.E., Briais, A., LeVay, L.J., and the Expedition 395 Scientists, Reykjanes Mantle Convection and Climate. Proceedings of the International Ocean Discovery Program, 395: College Station, TX (International Ocean Discovery Program). **https://doi.org/10.14379/iodp.proc.395.102.2025**

Parnell-Turner, R.E., Briais, A., LeVay, L.J., Cui, Y., Di Chiara, A., Dodd, J.P., Dunkley Jones, T., Dwyer, D., Eason, D.E., Friedman, S.A., Hemming, S.R., Hochmuth, K., Ibrahim, H., Jasper, C., Karatsolis, B.T., Lee, S., LeBlanc, D.E., Lindsay, M.R., McNamara, D.D., Modestou, S.E., Murton, B., OConnell, S., Pasquet, G.T., Pearson, P.N., Qian, S.P., Rosenthal, Y., Satolli, S., Sinnesael, M., Suzuki, T., Thulasi Doss, T., White, N.J., Wu, T., Yang Yang, A., dos Santos Rocha, V., Pearman, C., and Tian, C.Y., 2025b. Site U1554. In Parnell-Turner, R.E., Briais, A., LeVay, L.J., and the Expedition 395 Scientists, Reykjanes Mantle Convection and Climate. Proceedings of the International Ocean Discovery Program, 395: College Station, TX (International Ocean Discovery Program). **https://doi.org/10.14379/iodp.proc.395.103.2025**

Parnell-Turner, R.E., Briais, A., LeVay, L.J., and the Expedition 395 Scientists, 2025c. Supplementary material, **https://doi.org/10.14379/iodp.proc.395supp.2025**. In Parnell-Turner, R.E., Briais, A., LeVay, L.J., and the Expedition 395 Scientists, Reykjanes Mantle Convection and Climate. Proceedings of the International Ocean Discovery Program, 395: College Station, TX (International Ocean Discovery Program).

Poore, R.Z., 1979. Oligocene through Quaternary planktonic foraminiferal biostratigraphy of the North Atlantic: DSDP Leg 49. In Luyendyk, B.P., Cann, J.R., et al., Initial Reports of the Deep Sea Drilling Project. 49: Washington, DC (US Government Printing Office), 447–517. **https://doi.org/10.2973/dsdp.proc.49.115.1979**

Poore, R.Z., and Berggren, W.A., 1975. Late Cenozoic planktonic foraminiferal biostratigraphy and paleoclimatology of Hatton-Rockall Basin; DSDP Site 116. Journal of Foraminiferal Research, 5(4):270–293. **https://doi.org/10.2113/gsjfr.5.4.270**

Raffi, I., Wade, B.S., Pälike, H., Beu, A.G., Cooper, R., Crundwell, M.P., Krijgsman, W., Moore, T., Raine, I., Sardella, R., and Vernyhorova, Y.V., 2020. The Neogene Period. In Gradstein, F.M., Ogg, J.G., Schmitz, M.D., and Ogg, G. (Eds.), Geologic Time Scale 2020. (Elsevier), 1141–1215. **https://doi.org/10.1016/B978-0-12-824360-2.00029-2**

Siccha, M., and Kucera, M., 2017. ForCenS, a curated database of planktonic foraminifera census counts in marine surface sediment samples. Scientific Data, 4(1):170109. **https://doi.org/10.1038/sdata.2017.109**

Skilling, I.P., White, J.D.L., and McPhie, J., 2002. Peperite: a review of magma–sediment mingling. Journal of Volcanology and Geothermal Research, 114(1–2):1–17. **https://doi.org/10.1016/S0377-0273(01)00278-5**

Spiegler, D., 1999. Bolboforma biostratigraphy from the Hatton-Rockall Basin (North Atlantic). In Raymo, M.E., Jansen, E., Blum, P., and Herbert, T.D., Proceedings of the Ocean Drilling Program, Scientific Results, 162. College Station, TX (Ocean Drilling Program), 35–49. **https://doi.org/10.2973/odp.proc.sr.162.013.1999**

Zijderveld, J.D.A., 1967. AC demagnetization of rocks: analysis of results. In Runcorn, S.K.C., Creer, K.M., and Collinson, D.W. (Eds.), Methods in Palaeomagnetism. Developments in Solid Earth Geophysics, 3: 254–286. **https://doi.org/10.1016/B978-1-4832-2894-5.50049-5**